Title
Experimental and Analytical Studies on Pyroelectric Waste Heat Energy Conversion

Permalink
https://escholarship.org/uc/item/6rw643p5

Author
Lee, Felix

Publication Date
2012

Peer reviewed|Thesis/dissertation

UNIVERSITY OF CALIFORNIA

Los Angeles

Experimental and Analytical Studies on Pyroelectric Waste Heat Energy Conversion

A thesis submitted in partial satisfaction

of the requirements for the degree

Master of Science in Mechanical Engineering

by

Felix Lee

2012

<div align="center">

Abstract of the Thesis

Experimental and Analytical Studies on Pyroelectric Waste Heat Energy Conversion

by

Felix Lee

Master of Science in Mechanical Engineering

University of California, Los Angeles, 2012

Professor Laurent G. Pilon, Chair

</div>

This study is concerned with direct conversion of thermal energy into electrical energy by subjecting pyroelectric materials to the Olsen cycle. The Olsen cycle consists of two isoelectric field and two isothermal processes on the electric displacement versus electric field diagram. The energy and power generation capabilities of copolymer poly(vinylidene fluoride-trifluorethylene) [P(VDF-TrFE)] films and lead lanthanum zirconate titanate (PLZT) ceramics were evaluated by executing the Olsen cycle via so-called "stamping experiments" and "dipping experiments".

The stamping experiments consisted of alternatively pressing a pyroelectric material in thermal contact with hot and cold aluminum blocks under specified electric fields. It was performed to assess the pyroelectric energy conversion performance using heat conduction. The largest energy density generated in the stamping experiments was 155 J/L/cycle with 60/40 P(VDF-TrFE) thin film at 0.066 Hz between 25 and 110ºC and electric fields cycled between 20 and 35 MV/m. This energy density exceeded the 130 J/L/cycle achieved by our previous prototypical device using oscillatory laminar convective heat transfer. However, the performance was limited by poor thermal contact between the aluminum blocks and pyroelectric material and also by excessive leakage current inherent to P(VDF-TrFE) at high temperatures and/or large electric fields.

On the other hand, dipping experiments consisted of successively immersing a pyroelectric

<div align="center">ii</div>

material into isothermal hot and cold thermal reservoirs at different temperatures while simultaneously cycling the electric fields. It was performed on relaxor ferroelectric $x/65/35$ PLZT ceramics with x between 5 and 10 mol.%. The operating temperature, applied electric field, sample thickness, cycle frequency, and electrode material were systematically varied to explore their respective effects on the energy and power densities produced. A maximum energy density of 1014 J/L/cycle was obtained with a 190 μm thick 7/65/35 PLZT sample at 0.0256 Hz at temperatures between 30 and 200°C and electric field from 0.2 to 7.0 MV/m. To the best of our knowledge, this energy density is the largest achieved among pyroelectric single crystals, ceramics, and polymers using the Olsen cycle. Meanwhile, a maximum power density of 55.3 $\pm$ 8.0 W/L was obtained with a 190 μm thick 9.5/65/35 PLZT sample at 0.125 Hz. Additionally, the temperature-dependent dielectric behavior of PLZT ceramics was characterized.

The polarization transition temperature of lanthanum-doped $x/65/35$ PLZT ceramics decreased from 240 to 10°C for increasing lanthanum dopant concentration x from 5 to 10 mol.%. This establishes that the different compositions should be operated at different temperatures for maximum pyroelectric energy conversion. Finally, a physical thermo-electrical model for estimating the energy harvested by ferroelectric relaxors was further validated against experimental data for a wide range of electric fields and temperatures.

The thesis of Felix Lee is approved.

_____
Adrienne Lavine

_____
Christopher S. Lynch

_____
Laurent G. Pilon, Committee Chair

University of California, Los Angeles

2012

iv

Table of Contents

LIST OF FIGURES

x

xvi

List of Tables

Nomenclature

A	sample cross-sectional area, m^2
b	sample thickness, m
Bi	Biot number $(=hb/k)$
c_p	specific heat, J/kg·K
C	capacitance, F
D	electric displacement, C/m^2
ΔD	electric displacement span, C/m^2
d_{33}	piezoelectric coefficient, C/N
E	electric field, V/m
ΔT	change in electric field, ^{o}C
E_b	electrical breakdown field, V/m
E_c	coercive field, V/m
E_{cr}	critical electric field, V/m
f	frequency, Hz
h	heat transfer coefficient, W/m^2·K
k	thermal conductivity, W/m·K
I_p	electric current, A
I_L	leakage current, A
N_D	energy density, J/L
p_c	pyroelectric coefficient, C/m^2·K
P	polarization density, C/m^2
P_D	power density, W/L
P_r	remnant polarization, C/m^2
P_s	saturation polarization, C/m^2
Q	heat flow, J
PE	pyroelectric element
R	resistance, Ω

s_{33}	elastic compliance, m^2/N
S	entropy, J/kg·K
ΔS	entropy change, J/kg·K
t	time, s
T	temperature, ^{o}C or K
ΔT	temperature swing, ^{o}C
T_B	Burns temperature, ^{o}C
T_{Curie}	Curie temperature, ^{o}C
T_H	temperature of hot source, ^{o}C
T_p	polarization transition temperature, ^{o}C
x	lanthanum doping level
x_3	strain in longitudinal direction $[=\alpha_3(T_{hot}\text{-}T_{cold})]$
V	voltage, V
VDC	DC voltage, V
V_1	voltage across capacitor, V
V_2	voltage across resistor, V
V_{PE}	voltage across pyroelectric element, V

Greek symbols

α	linear thermal expansion coefficient, K^{-1}
β	beta crystal phase
δ	relative error between experimental data and model predictions, %
ε_o	vacuum permittivity (= 8.854x10^{12} F/m)
ε_r	relative permittivity
γ	gamma crystal phase
λ	radiative wavelength, m
ρ	density, kg/m^3
ρ_R	electrical resistivity, Ω·m
σ	elastic stress, Pa

τ_t	thermal characteristic time constant $(=1/f)$, s
τ_{i-j}	period of process i-j, s

Subscripts

avg	refers to average
$cold$	refers to cold
cr	refers to critical
eff	refers to effective
H	refers to high
hot	refers to hot
L	refers to low
max	refers to maximum
PE	refers to pyroelectric element
$*$	refers to electric field corresponding to maximum power density
$+$	refers to electric field corresponding to maximum energy density

ACKNOWLEDGMENTS

CHAPTER 1

Introduction

The objective of this chapter is to present the motivations and background of this study. First, energy usage in our society and the waste heat sources are discussed. This is followed by a brief discussion of common methods for converting waste heat into useful electrical energy. Then, the pyroelectric effect and previous studies on pyroelectric energy conversion are reviewed and the scope of this MS thesis is introduced. This chapter concludes with the research objectives of this study.

1.1 Motivations

The world is facing an unprecedented combination of economic, environmental, demographic, and energy challenges that exert stress on the Earth's resources and our inhabitants' quality of life. Over the past century, the world's human population has been increasing significantly. For instance, from 1973 to 2010, the world population grew from 3.9 to 7.0 billion human beings corresponding to a 79% increase [8]. According to the United Nations, the world population is projected to increase by 25% to 9.3 billion people by 2050 [9]. A majority of these increases are predicted to occur throughout regions which will also experience increases in urbanization [10]. This will result in a significant increase in energy demand. Therefore, these trends call for more efficient and less polluting energy technologies.

1.2 Waste heat

Waste heat refers to the thermal energy released as a by-product of power, refrigeration, or heat pump cycles as required by the second law of thermodynamics. It is often released into the atmosphere, rivers, or oceans in the form of hot gases or hot water. Figure 1.1 shows estimates of the energy produced, used, and wasted in the United States during 2009 in quadrillion British thermal units (10^{15} BTU) [1]. It shows that only 42.3% of the energy contained in raw energy sources (e.g., petroleum, natural gas, and coal) was useful in residential, commercial, industrial, electricity generation, or transportation applications. The remaining 57.8% was wasted mainly in the form of waste heat. A wide variety of processes produce large amounts of waste heat. For example, only 20-30% of the energy consumed in the transportation sector was useful while the remaining 70-80% was lost through the tailpipe or the radiator in vehicles [11]. In addition, over 65% of the energy consumed in the electric generation sector was wasted. This sector contributes to the largest form of energy consumption. As energy demands continue to increase, it would be advantageous for society to harvest wasted heat and convert it into usable forms.

Waste heat can be divided into three categories: low, medium, and high grade waste heat with temperatures ranging from 27 to 205°C, 205 to 593°C, and 593 to 1649°C, respectively [12]. High-grade waste heat can be easily reused to generate more electricity using conventional power cycles. For example, the flue gas emitted from gas turbines operating using the Brayton cycle may be reused to produce steam in power plants based on the Rankine cycle. It can also be used to heat water for domestic and industrial uses as in co-generation schemes [13]. On the other hand, thermal heat dissipated from servers, data centers, solar panels, and internal combustion engines are sources of low and medium grade waste heat. Unfortunately, there are fewer solutions for converting medium and low grade waste heat into usable forms of energy.

The necessity to develop more energy efficient engineering systems has brought significant attention to waste heat energy harvesting devices [14–16]. If waste heat can be efficiently recycled into useful forms of energy, it may compete as a potential source to meet the rising
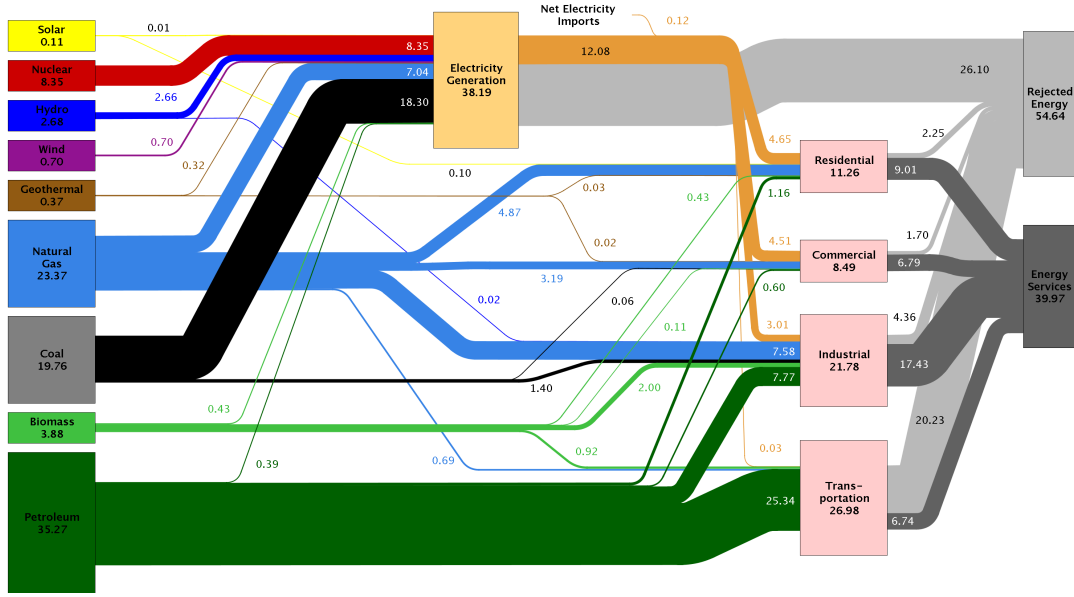
Figure 1.1: Flow chart of the energy produced, used, and wasted in the United States in 2009 (unit in quads, 10^{15} Btu) [1].

energy demand. Unfortunately, small Carnot efficiencies have hindered the development of such devices. Organic Rankine cycles and Stirling engines have been utilized to convert waste heat into mechanical work [14, 15]. Particularly, Stirling engines have been used in a variety of applications including heat pumps, cryogenic refrigeration, and air liquefaction [15]. More recently, they have been utilized in solar power plants [17] and automobiles [18]. Theoretically, Stirling engines can achieve Carnot effciency, but losses due to gas leakage, friction, and heat losses to the surroundings reduce their efficiency [15]. Moreover, an additional step is required to convert mechanical energy into electricity by means of an electrical generator. Additionally, thermoelectric devices utilize the Seebeck effect to directly convert a steady-state temperature difference at the junction of two dissimilar metals or semiconductors into electrical energy [16]. Commercial thermoelectric generators have efficiencies reported to be *"typically around 5%"* [16]. The low efficiencies can be owed to the intrinsic limitations of the thermoelectric materials available in nature with a combination of low thermal conductivity, high electrical conductivity, and large Seebeck factor. Alternatively, pyroelectric energy conversion devices require thermal cycling of a pyroelectric element (PE) between a

hot and a cold temperature source combined with a cycle in the displacement-electric field diagram to produce electricity [4–7, 19–35]. The energy generated by a pyroelectric device can be harvested in practice by delivering it to an external load or storage unit.

1.3 Pyroelectric energy conversion

Pyroelectric energy conversion offers a novel and direct way to convert heat into electricity by transforming time-dependent temperatures directly into electricity [19–23, 36]. It makes use of the pyroelectric effect to create a flow of charge to or from the surface of a pyroelectric material as a result of heating or cooling [3]. The fact that very small changes in temperature ($\sim$mK) can produce a pyroelectric current on the order of nA or pA [3] has been used extensively in infrared detection for imaging and motion sensing as well as thermometer applications [37]. Recently, pyroelectric materials have been used to directly convert thermal energy to electrical energy via a thermal-electrical cycle. The use of pyroelectric materials to harvest waste heat has been explored both experimentally and theoretically. Although early theoretical studies predicted low efficiencies [38, 39], experimental studies [4, 19, 20, 22, 29, 36, 40] have shown significantly better results. Overall, however, little effort has been made to develop pyroelectric energy conversion.

1.4 Objectives and scope

This study is concerned with materials and practical implementation of pyroelectric waste heat energy harvesting. Its objectives are as follows:

1. to experimentally demonstrate the concept of stamping and the use of heat conduction for implementing a pyroelectric energy cycle using copolymer poly(vinylidene fluoride-trifluoroethylene) [P(VDF-TrFE)],

2. to experimentally measure the energy and power densities of relaxor ferroelectric lead lanthanum zirconate titanate (PLZT) undergoing the Olsen cycle under various oper-

ating conditions,

3. to characterize the dielectric behavior of PLZT with different lanthanum doping and for different temperatures,

4. to assess the validity of a previously developed physical model used for estimating the energy generation capabilities of pyroelectric materials over a wide range of operating conditions.

Chapter 2 begins with a review of the current state of knowledge in materials and pyroelectric energy conversion. Chapter 3 presents practical implementation of the Olsen cycle using conductive heat transfer. Chapters 4, 5, and 6 describe the experiments performed to measure the energy and power densities generated using various pyroelectric materials. The effects of different operating parameters on the energy and power generation performance are discussed in detail. Finally, Chapter 7 summarizes the conclusions drawn from this study and provides recommendations for future research.

CHAPTER 2

Current State of Knowledge

This chapter begins with an introduction on the physical concepts governing pyroelectric energy harvesting. An overview of dielectric materials is provided and followed by a review of pyroelectricity and ferroelectricity. Next, the Olsen cycle for pyroelectric energy conversion is introduced. Various modes of heat transfer and practical implementation of this cycle are discussed. Then, a review of common pyroelectric materials is presented with emphasis on polymeric and ceramic materials. This chapter closes with a discussion of the desirable properties required for maximum pyroelectric energy generation performance.

2.1 Material considerations

Dielectric materials, also known as electrical insulators, can withstand an applied electric field without conducting electrical charges through their bodies. They are frequently used in capacitors for energy storage as well as for power conditioning. Figure 2.1 depicts a dielectric film with thickness b (in m) and surface area A (in m^2) sandwiched between two electrodes subjected to an electric field $\vec{E}$ (in V/m). The field is perpendicular to the surface of the film and its amplitude is given by,

$$E = \frac{V}{b} \tag{2.1}$$

where V is the applied voltage (in V). The maximum electric field that the material can withstand without being conductive is called the electric breakdown field or dielectric strength E_b [2]. For applied fields larger than E_b, the material is no longer electrically insulated and instead charges are conducted through it.

The applied electric field causes electrical charges to accumulate at the surface of the
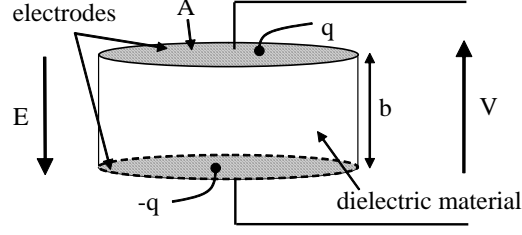
Figure 2.1: Schematic of a dielectric material with electrodes subjected to an electric field $\vec{E}$.

material. The amount of charges per unit surface area is the so-called electric displacement D (in C/m^2). For a linear and isotropic material, D is defined as,

$$D = \epsilon_r \epsilon_0 E + P \tag{2.2}$$

where ϵ_r is the relative dielectric constant, ϵ_0 is the vacuum permittivity (in C/V·m) and P is the polarization density (in C/m^2). Here, the electric displacement, electric field, and polarization vectors are assumed to be collinear and normal to the film's surface. For simplicity, and unless otherwise noted, the directions of all vectors are assumed to be the same so that only their magnitudes are necessary.

Classifications

There are a total of 32 crystal classes of dielectric materials [2]. Twenty of these crystal classes lack a center of symmetry and are called piezoelectrics. Among these twenty classes, ten demonstrate a unique polar axis and exhibit spontaneous polarization. They are named pyroelectrics. Out of the ten pyroelectric crystal classes, there exists a smaller group referred to as ferroelectrics that have two or more orientational stages which can be switched from one state to another by applying an electric field [2]. These states have identical structure, but differ only in their electric polarization vector at zero applied electric field. The remaining ten pyroelectric classes are known as paraelectrics which do not display spontaneous polarization, but can be polarized by an electric field. Note that while all ferroelectrics are pyroelectric and all pyroelectrics are piezoelectric, the converse is not true. Figure 2.2 illustrates how

these different crystals can be classified into these different categories.
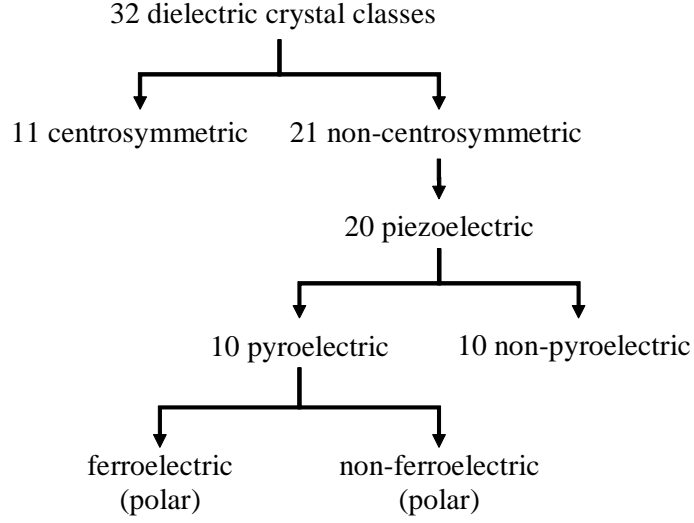
Figure 2.2: Classification of dielectric crystal symmetry classes depicting the relationship between piezeoelectric, pyroelectric, and ferroelectric materials [2].

2.2   Pyroelectric effect

The displacement of the atoms from their equilibrium positions upon heating and cooling results is a result of the pyroelectric effect. Changes in temperature cause proportional changes in the electric displacement according to [3],

$$dD = p_c dT \tag{2.3}$$

where p_c is the pyroelectric coefficient (in C/m^2·K) defined as [3],

$$p_c = \left(\frac{\partial D}{\partial T}\right)_{E,\sigma} = \left(\frac{\partial P_S}{\partial T}\right)_{E,\sigma} \tag{2.4}$$

where σ is the elastic stress (in Pa) and E is the electric field (in V/m). The pyroelectric coefficient is a vector which can be treated as a scalar if the electrodes are normal to the polarization axis. The electric current I_p generated by pyroelectric materials during heating

and cooling is given by [4],

$$I_p = Ap_c \frac{dT}{dt} \tag{2.5}$$

Note that Equation (2.5) is not valid for large temperature changes due to non-linear behavior [41].

Figure 2.3 depicts the pyroelectric effect taking place in pyroelectric films [3]. The spon-
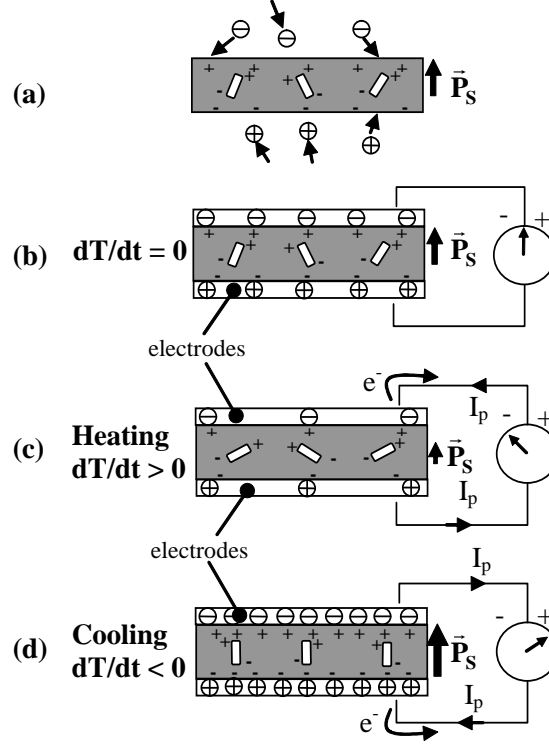
Figure 2.3: Schematic of a pyroelectric sample (a) by itself and with electrodes and connected to an ammeter (b) at constant temperature, (c) while being heated, and (d) while being cooled (adapted from Lang [3]).

taneous polarization of a bare slab naturally attracts free charges such as electrons and ions to its surface as shown in Figure 2.3a. Now, consider the case when electrodes are attached to the top and bottom surfaces of the pyroelectric film and connected to an ammeter. At steady-state ($dT/dt = 0$), the spontaneous polarization remains constant and therefore no current flows through the ammeter as shown in Figure 2.3b. However, as temperature increases ($dT/dt > 0$), electric dipole moments lose their orientations, leading to a decrease

in spontaneous polarization as illustrated in Figure 2.3c. Upon cooling ($dT/dt < 0$), the spontaneous polarization increases and the current read by the ammeter reverses sign as depicted in Figure 2.3d.

2.3   Electrocaloric effect

The converse of the pyroelectric effect is the electrocaloric effect. It is the change in temperature caused by a change in applied electric field under adiabatic conditions [3]. The electrocaloric temperature change can be measured directly or indirectly. Direct measurements arise from the thermodynamic term $\frac{\Delta T}{\Delta E} = \left(\frac{\partial S}{\partial E}\right) / \left(\frac{\partial S}{\partial T}\right)$ evaluated during an electrocaloric effect cooling cycle. It requires precise calorimetry. Direct measurements have been performed by Kutnjak *et al.* [42] for multilayer capacitors. On the other hand, indirect measurements make use of a Maxwell relation $\left(\frac{\partial S}{\partial E}\right)_T = \left(\frac{\partial D}{\partial T}\right)_E$ to evaluate the entropy change given by

$$\Delta S = - \int_{E_1}^{E_2} \left(\frac{\partial D}{\partial T}\right)_E \mathrm{d}E. \tag{2.6}$$

Equation 2.6 can be simplified from the term $\Delta S = Q/T$ to yield the expression for adibatic temperature change

$$\Delta T = -\frac{1}{\rho} \int_{E_1}^{E_2} \frac{T}{c_p} \left(\frac{\partial D}{\partial T}\right)_E \mathrm{d}E. \tag{2.7}$$

Equation 2.7 shows that large electrocaloric effect can be observed with materials featuring large entropy change ΔS and large electric displacement span ΔD [43]. In addition, pyroelectric thin films capable of sustaining large electric field without electrical breakdown are desirable to achieve a large ΔT.

Sebald *et al.* [44] have shown theoretically that materials with large electrocaloric activity possess large pyroelectric constants $\left(\frac{\partial D}{\partial T}\right)$ and hence they are of interest in pyroelectric energy harvesting. Large electrocaloric effects have recently been demonstrated [43, 45–48]. For example, a temperature rise of 12 K was calculated for a change in electric field from 295 to 776 kV/cm across 350 nm thick zirconium rich PZT thin films, near the Curie temperature of 220°C [45]. Furthermore, Mischenko *et al.* [46] calculated large electrocaloric activity near

room temperature with 260 nm thick 0.9PMN-0.1PT thin films. The authors calculated a 5 K temperature rise as the electric field increased from 588 to 895 kV/cm near the Curie temperature of 60^oC. Similarly, studies on 210 nm thick 0.93PMN-0.07PT films suggested the possibility of a 9 K temperature rise for electric field between 0 and 723 kV/cm near 25^oC [47]. In addition, a 9 K temperature rise was calculated for 1 μm thick terpolymer poly(vinylidene fluoride trifluoroethylene-chlorofluoroethylene) [P(VDF-TrFE-CFE)] films of composition 59.2/33.6/7.2 mol.% between 0 and 3000 kV/cm near 45^oC [48]. More recently, Lu *et al.* [43] demonstrated a large electrocaloric effect on 8/65/35 PLZT thin films. The electrocaloric temperature change of $\Delta T = 40$ K was observed for 0.45 μm thick 8/65/35 PLZT at around 45^oC under an electric field of 125 MV/m.

2.4   Pyroelectricity/ferroelectricity

Pyroelectric materials possess a spontaneous polarization defined as the average electric dipole moment per unit volume in absence of an applied electric field [49]. The spontaneous polarization is strongly dependent on temperature due to the pyroelectric material's crystallographic structure [3]. A subclass of pyroelectric materials known as ferroelectric materials have a spontaneous polarization that can be switched between crystallographically-defined equilibrium states from $-P_S$ to $+P_S$ by reversing the external electric field [2]. Ferroelectric materials have a history-dependent response to a given set of external conditions such as electric field which results in a nonlinear hysteresis loop. Note that while all ferroelectrics are pyroelectric and all pyroelectrics are piezoelectric, the converse is not true.

Figure 2.4 shows the quasi-isothermal bipolar hysteresis curves between electric displacement D and electric field E exhibited by a nonlinear pyroelectric material at two different temperatures T_{cold} and T_{hot} [50–53]. It indicates that D does not vary linearly with E. These so-called D-E loops are traveled in a counter-clockwise direction. The D-E loops corresponding to T_{cold} and T_{hot} are characteristic of a typical ferroelectric and paraelectric material, respectively. Note that a paraelectric material can still polarize but only when an external electric field is applied. As a ferroelectric material is heated, the hysteresis curves
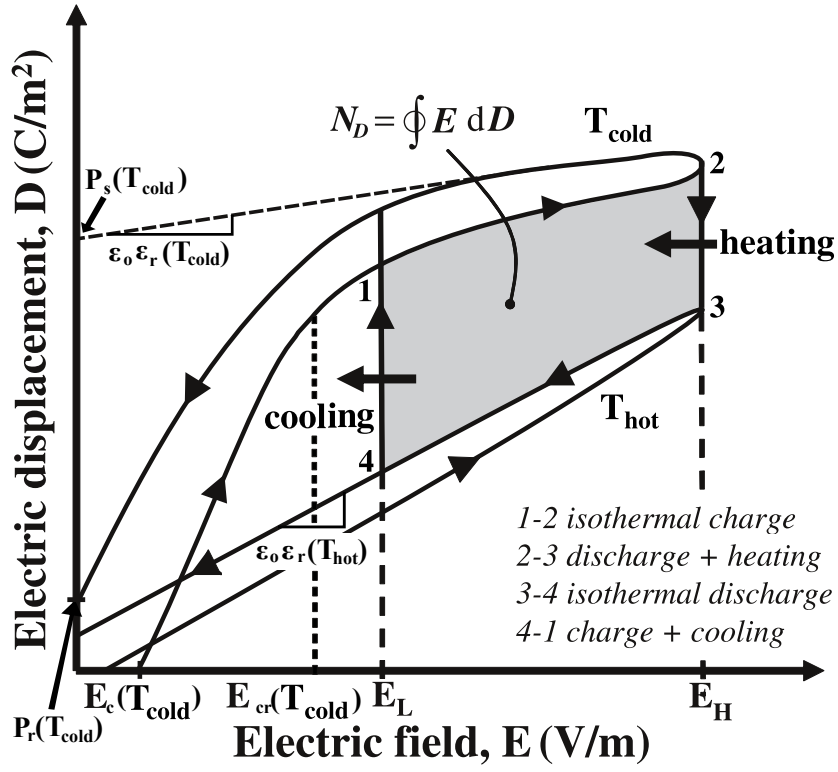
Figure 2.4: Isothermal bipolar electric displacement versus electric field (D-E) hysteresis loops for a typical pyroelectric material at temperatures T_{hot} and T_{cold} along with the Olsen cycle. The electrical energy generated per cycle is represented by the area enclosed between 1-2-3-4.

become more narrow and linear until it transforms into a line through the origin. A ferroelectric material undergoes a phase transition from ferroelectric to paraelectric when it is heated above its Curie temperature denoted by T_{Curie}. Then, the spontaneous polarization vanishes. Pyroelectric energy conversion makes use of this phase transition to generate a current. The electric displacement D of an isotropic pyroelectric material at electric field E and temperature T can be expressed as [2,54]

$$D(E,T) = \varepsilon_0 \varepsilon_r(T) E + P_s(T) \tag{2.8}$$

where ε_o is the vacuum permittivity ($= 8.854 \times 10^{12}$ F/m) and $\varepsilon_r(T)$ is the relative permittivity of the material at electric field E and temperature T. The saturation polarization denoted by $P_s(T)$ is estimated as the electric displacement in the linear fit of D versus E extrapolated from a finite electric field to zero electric field as illustrated in Figure 2.4. The slope of this linear fit is equal to the product $\varepsilon_0 \varepsilon_r(E,T)$. In this case, $\varepsilon_r(E,T)$ corresponds to the large field dielectric constant. The remnant polarization $P_r(T)$ corresponds to the polarization under zero applied electric field and the coercive field $E_C(T)$ corresponds to the electric field required to reach zero polarization. The critical electric field $E_{cr}(T)$ was estimated from the inflection point in the isothermal D-E loop.

Note that the polarization density of a pyroelectric material can be expressed as the sum of (1) the induced polarization due to the displacement of space charges, ions, and electrons in the material in the presence of an electric field and (2) the polarization due to the spontaneous alignment of dipoles in the material. Therefore, Equation 2.2 can be rewritten as Equation 2.8 for a pyroelectric material.

Furthermore, when a pyroelectric material is heated, it experiences thermal expansion and thermal stresses. All pyroelectric materials are piezoelectric, and therefore, the piezoeletric effect indirectly induces further polarization. However, the piezoelectric contribution to polarization is less than 10% of the total polarization and is neglected in this work.

2.5 Olsen cycle

2.5.1 Principle

The so-called Olsen cycle in the electric displacement-electric field (D-E) diagram of a pyroelectric material is analogous to the Ericsson cycle defined in the pressure versus specific volume diagram of a working fluid. The cycle was developed by Olsen and co-workers between 1978 and 1985 [2–4, 25, 36, 55–57]. It consists of two isothermal and two isoelectric processes performed on a pyroelectric element (PE) in the electric displacement versus electric field (D-E) diagram [19] as illustrated in Figure 2.4. A pyroelectric element consists of a pyroelectric thin film and its metallic electrodes deposited on both faces. Process 1-2 consists of charging the PE at T_{cold} by increasing the applied electric field from E_L to E_H. Process 2-3 corresponds to discharging the PE by heating it from T_{cold} to T_{hot} under constant electric field E_H. Process 3-4 consists of reducing the electric field from E_H to E_L under isothermal conditions at T_{hot}. Finally, Process 4-1 closes the cycle by cooling the PE from T_{hot} to T_{cold} under constant electric field E_L. In brief, the principle of the Olsen cycle is to charge a capacitor via cooling under low electric field and to discharge it under heating at higher electric field.

The area enclosed by the clockwise 1-2-3-4 loop in the D-E curve represents the electric energy produced per unit volume of material per cycle denoted by N_D (in J/L/cycle) and defined as [19]

$$N_D = \oint E \mathrm{d}D. \tag{2.9}$$

The corresponding power density P_D (in W/L) produced by the pyroelectric element is expressed as

$$P_D = N_D f \tag{2.10}$$

where f is the cycle frequency. Note that N_D is also dependent on the cycle frequency [30,58]. It is evident that (i) increasing T_{hot} and decreasing T_{cold} and/or (ii) increasing the electric field span (E_H - E_L) results in larger energy generated. However, this is limited by the thermoelectromechanical stress that the sample can withstand.

2.5.2 Physical modeling

Recently, Kandilian *et al.* [53] developed a physical model predicting the amount of energy harvested by relaxor ferroelectric materials undergoing the Olsen cycle. The model accounted for temperature-dependent properties of the material. The energy density N_D was expressed as [53]

$$N_D(E_L, E_H, T_{cold}, T_{hot}) = (E_H - E_L) \left\{ \frac{\varepsilon_0}{2} \left[\varepsilon_r(T_{cold}) - \varepsilon_r(T_{hot}) \right] (E_H + E_L) + \right.$$
$$\left. P_s(T_{cold}) - P_s(T_{hot}) + \frac{d_{33} x_3}{s_{33}} \right\} \quad (2.11)$$

where $\varepsilon_r(T_{cold})$ and $\varepsilon_r(T_{hot})$ are the low frequency relative permittivities of the pyroelectric material at the cold and hot operating temperatures T_{cold} and T_{hot}, respectively. The saturation polarizations of the material at T_{cold} and T_{hot} are denoted by $P_s(T_{cold})$ and $P_s(T_{hot})$, respectively, and expressed in C/m^2. Note that Kandilian *et al.* [53] erroneously called $P_s(T)$ the spontaneous polarization instead of saturation polarization as sometimes found in the literature [59]. The piezoelectric coefficient d_{33} is expressed in C/N, s_{33} is the elastic compliance (in m^2/N), and $x_3 = \alpha_3(T_{hot} - T_{cold})$ where α_3 is the linear thermal expansion coefficient (in K^{-1}). Note that this model was based on the assumption that the dielectric contribution to the primary pyroelectric coefficient was negligible compared with the dipole contribution (See Equation (8) in Ref. [53]). The model successfully predicted the energy density harvested by PMN-32PT [53] and PZN-5.5PT [58]. Here also, the model predictions will be compared with the energy density experimentally measured with 8/65/35 PLZT.

2.6 Phase transitions

Figure 2.5 displays an electric displacement D versus electric field E curve for a typical ferroelectric material at three different temperatures T_1, T_2, and T_3 such that $T_1 < T_2 < T_3$. At T_1, the material is ferroelectric with a large saturation polarization. As the material is heated to $T_2 > T_1$, the hysteresis curve degenerates into a slim loop and the saturation polarization decreases. For temperature T_3 beyond the Curie temperature, the saturation polarization is zero and the material is paraelectric [60, 61]. The temperature at which the

transition from ferroelectric to paraelectric occurs is denoted by T_{Curie}. Pyroelectric energy converters make use of the phase transitions to generate additional electrical energy.
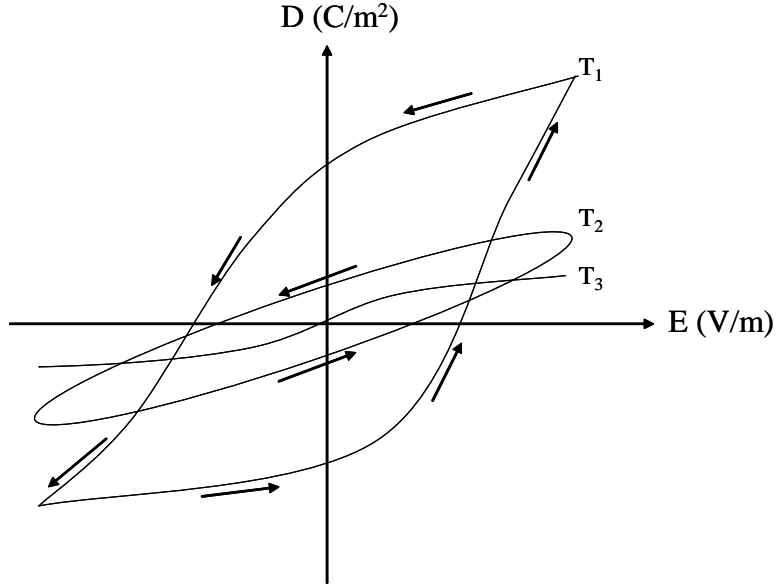
Figure 2.5: Electric displacement versus electric field for a dielectric material that transitions from ferroelectric to paraelectric phase at temperatures below and above the Curie temperature T_{Curie} ($T_1 < T_2 < T_{Curie} < T_3$).

2.7 Leakage current

Leakage current has often been incriminated for reducing the performance of pyroelectric materials used as power generators [4, 25, 36, 55]. Ideally, the resistance of the pyroelectric element should be infinite since it is a dielectric material. This would correspond to zero leakage across the PE. In reality, however, the resistance is finite and decreases as the applied electric field and temperature increase. As a result, a so-called leakage current denoted I_L flows through the PE, thus reducing the electrical energy produced [4, 25, 36, 55]. Figure 2.6 indicates that a pyroelectric material can be represented by (i) a current generator I_p, (ii) a capacitor C_{PE}, and (iii) a resistor R_{PE} in parallel. The PE behaves as a current generator where the direction of current reverses upon heating and cooling. It has (i) a capacitance
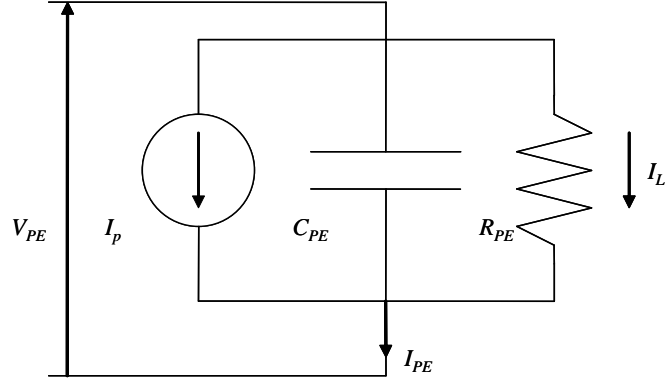
Figure 2.6: Equivalent circuit of a pyroelectric element during cooling [4].

since it is a dielectric film with two electrodes and (ii) a finite resistance since the material conducts at high temperatures and electric fields.

Figure 2.7 shows a typical Olsen cycle for a pyroelectric element (a) with no leakage current ($R_{PE} = \infty$) and (b) with leakage current (finite R_{PE}). Note that in Figure 2.7a the

(a) Ideal case, $I_L = 0$ (b) In practice, $I_L > 0$
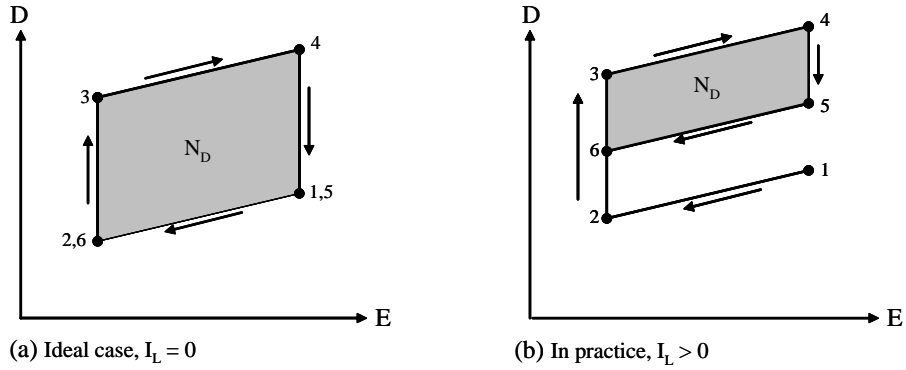
Figure 2.7: Pyroelectric conversion cycle for a pyroelectric element (a) in absence and (b) in presence of a leakage current.

cycle starts and ends at the same point while in Figure 2.7b the charge across capacitor C_1 increases over time due to leakage current. This decreases the size of the enclosed area and the generated power. Therefore, in order to efficiently convert thermal energy into electrical energy, the leakage current must be reduced.

2.7.1 Parameters affecting leakage current

Ideally, one would want to increase the temperature and electric field spans applied to the PE in order to enlarge the surface area described by the Olsen cycle in the D-E curve shown in Figure 2.4. Unfortunately, these benefits are counter-balanced by the fact that the leakage current increases with (i) increasing temperature, (ii) increasing electric field, and (iii) the time during which a large electric field E_H is applied to the PE.

2.7.2 Practical solutions

In order to limit the leakage current, the following strategies can be implemented,

1. Reduce the maximum operating temperature. Although this results in lower pyroelectric current I_p, it also increases the net output due to an even larger reduction in the leakage current I_L [4].

2. Reduce the maximum voltage V_H for the same reasons as described above [4].

3. Decrease the time during which the PE is subjected to high temperatures and voltages (process 2-3) [4].

4. Bake out, or vacuum heat, the pyroelectric material before attaching the electrodes in order to evaporate all solvents within the material [36].

5. Pre-polarize the PE which reduces the leakage current by increasing the film resistance [55].

2.8 Pyroelectric materials

The most important component in pyroelectric energy conversion is the pyroelectric material. This section reviews the different types of pyroelectric materials available in nature with emphasis on polymers and ceramics. They include

1. ceramics such as lead zirconate titanate (PZT), barium titanate ($BaTiO_3$), and lithium titanate ($LiTiO_3$) [2],

2. single crystals such as lead magnesium niobate-lead titanate (PMN-PT) and lead zirconate niobate-lead titanate (PZN-PT) [62–65],

3. polymers like polyvinylidene fluoride (PVDF), polyvinylidene fluoride trifluoroethylene (P(VDF-TrFE)), polyvinylidene fluoride trifluoroethlyene chlorofluoroethylene (P(VDF-TrFE-CFE)) [2, 57],

4. biological materials including bovine phalanx, femur bones, and collagen (found in fish scales and hair) [3, 66], and

5. minerals such as tourmaline and quartz [3].

Ceramics based on the lead zirconate titanate system (PZT) are the most commonly used material since they are mechanically and chemically robust [3]. These materials feature high Curie temperatures and can be used for high temperature space applications. In addition, variation of the Zr/Ti ratio and the addition of dopants in PZT may favorably alter the physical properties of the ceramics [3]. On the other hand, polyvinylidene fluoride polymer (PVDF) and its copolymers are cheap to fabricate, can be operated at low temperatures, and possess large energy densities per unit mass. The choice of material may be a tradeoff between expense and performance.

2.8.1 Polymer PVDF and co-polymer P(VDF-TrFE)

One prominent pyroelectric polymer, PVDF, and its copolymer P(VDF-TrFE) have received more attention than any other polymeric materials as they have been used in biomedical and industrial applications [2]. These polymeric materials are attractive since they have large pyroelectric coefficients. For example, P(VDF-TrFE) has a pyroelectric coefficient of 40 μC/m^{2}K representing the highest among any polymers ever reported [67]. Moreover, it has been shown that polymeric pyroelectric materials possess low density, low cost, high

flexibility, and a larger dielectric strength. In fact, P(VDF-TrFE) has an electric breakdown field E_b that is 25 times greater than that of PZT [23], thus making it very attractive for pyroelectric power generation applications.
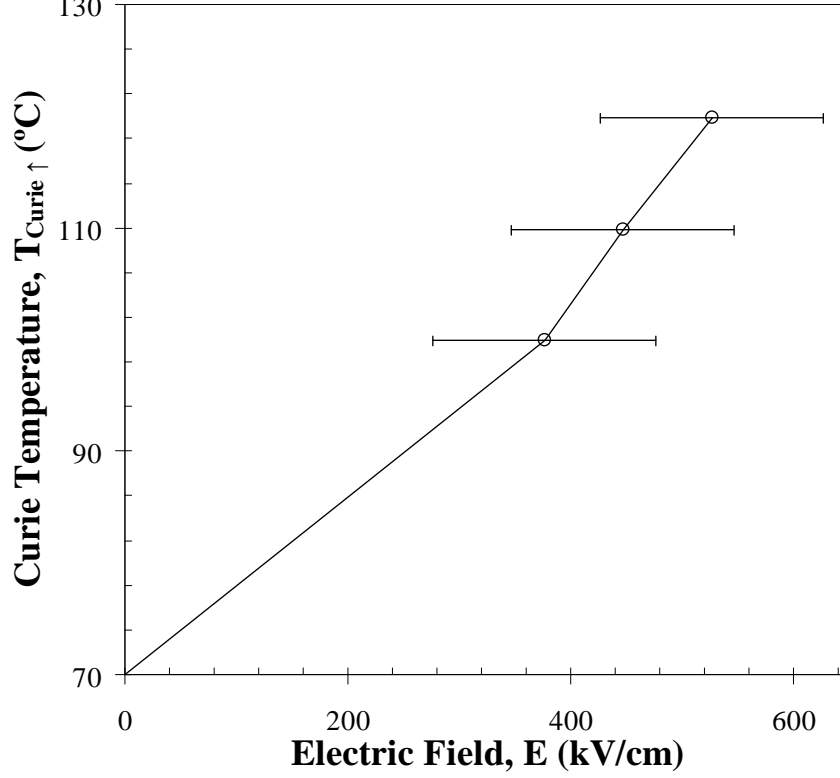
Figure 2.8: Ferroelectric to paraelectric phase transition temperature as a function of applied electric field for 60/40 P(VDF-TrFE) [5].

Figure 2.8 shows the ferro-paraelectric phase transition temperature T_{Curie} as a function of applied electric field for 60/40 P(VDF-TrFE) [5]. It reveals that T_{Curie} increases with the applied electric field. At zero field, T_{Curie} is approximately 70°C and increases to 120°C when the field is 527 kV/cm. The lower T_{Curie} of P(VDF-TrFE) compared to ceramics makes it attractive for low temperature waste heat harvesting.

PVDF has at least four crystal phases, including the α, β, γ, and δ-phases. While the α-phase is paraelectric and more stable, the β-phase exhibits the strongest ferroelectric properties [56]. When cooled from liquid to solid states in absence of external stresses, PVDF

crystallizes into the non-polar α-phase. Alternatively, the β, γ, and δ-phases are achieved by simultaneously deforming and poling the polymer [2, 56]. Electric poling is a process by which the α-phase crystals are converted into β-phases by the alignment of dipole moments of individual crystallites in the direction of an applied electric field [56]. Unlike PVDF, co-polymer P(VDF-TrFE) crystallizes into the ferroelectric β-phase in absence of external stresses [55]. Re-poling P(VDF-TrFE) occurs spontaneously and requires only cooling below T_{Curie}. On the contrary, re-poling PVDF requires mechanical deformation or electric poling yet again.

2.8.2 Relaxor ferroelectric PLZT ceramics

Relaxor ferroelectric materials have been studied extensively due to their (i) exceptional electro-optic properties for optical shutters, (ii) outstanding electrostrictive coefficient for actuators, and (iii) large dielectric constant for capacitors [68, 69]. The $x/65/35$ PLZT system is a commonly used relaxor ferroelectric consisting of x mol.% lanthanum doped into a 65 mol.% lead zirconate and 35 mol.% lead titanate solid solution $[Pb_{1-x}La_x(Zr_{0.65}Ti_{0.35})_{1-x/4}O_3]$. The chemical substitution of A-site lead Pb^{2+} with aliovalent lanthanum La^{3+} in lead zirconate titanate (PZT) introduces dipolar defects which break translational lattice symmetry due to the different sizes and ion valences. It also weakens the coupling between ferroelectric-active oxygen octahedral in the unit cell, thus preventing spontaneous formation of a long-range ordered state [70]. The lanthanum donor dopant increases structural and compositional disorder responsible for inducing relaxor behavior and contributes to the strong electromechanical coupling [71–73]. Furthermore, the lanthanum doping counteracts the p-type conductivity of PZT and increases the electrical resistivity of PLZT materials by at least three orders of magnitude [74].

The phase diagram [75, 76] of $x/65/35$ PLZT ceramics with $5 \leq x \leq 9$ mol.% feature rhombohedral crystal symmetry and are near the rhombohedral ferroelectric-mixed ferroelectric/cubic phase boundary [76]. The phase transition of the $x/65/35$ PLZT system depends on the applied electric field, temperature, and frequency [77–80]. It is paraelectric beyond

the Burns temperature $T_B \simeq 350^o$C corresponding to the Curie temperature of the La-free composition [81]. Upon cooling below T_B, the material transforms from paraelectric to ergodic relaxor resulting in domain alignment and enlargement of the domain correlation radius [69]. As domains grow and coalesce into polar clusters characteristic of the ferroelectric state, random fields induced in the relaxor state become suppressed [69].

The phase transition between ergodic relaxor (nanodomain) and ferroelectric (macrodomain) is field-dependent and occurs at the Curie temperature T_{Curie}. The latter can be determined from the maximum of the pyroelectric coefficient $(\partial D/\partial T)_{\sigma,E}$ versus temperature T curve measured under a specified electric field E. The material can revert phase from ferroelectric to ergodic relaxor by heating it above T_{Curie} and/or depoling below a critical electric field $E_{cr}(T)$. In x/65/35 PLZT, the ferroelectric phase cannot be established spontaneously upon cooling (under zero electric field) [79]. However, the ferroelectric phase can be induced and stabilized from the ergodic relaxor phase by applying an external electric field E greater than $E_{cr}(T)$ [82–85].

Relaxor ferroelectrics are different from classical ferroelectric materials in that the former exhibit strong frequency dispersion in dielectric permittivity below the temperature corresponding to the maximum permittivity [69]. This dispersion is attributed to the distribution of time constants associated with reorientation of polar nanodomains.

2.8.3 Performance of pyroelectric materials

The following lists properties desirable in pyroelectric materials to achieve maximum electrical energy and power output.

1. Large pyroelectric coefficient in order to generate a large pyroelectric current according to Equation (2.5).

2. Large spontaneous polarization so that more charges can be stored on the material's surface to produce a large pyroelectric current.

3. Large dielectric strength to enable large applied electric field during the Olsen cycle

without breakdown.

4. Small leakage current caused by electrical conduction through the material that reduces the energy density.

5. Short discharge time of the surface charges in order to minimize cycle period and to maximize power density.

6. Small heat capacity to enable rapid isoelectric heating and cooling processes of the Olsen cycle to maximize power density.
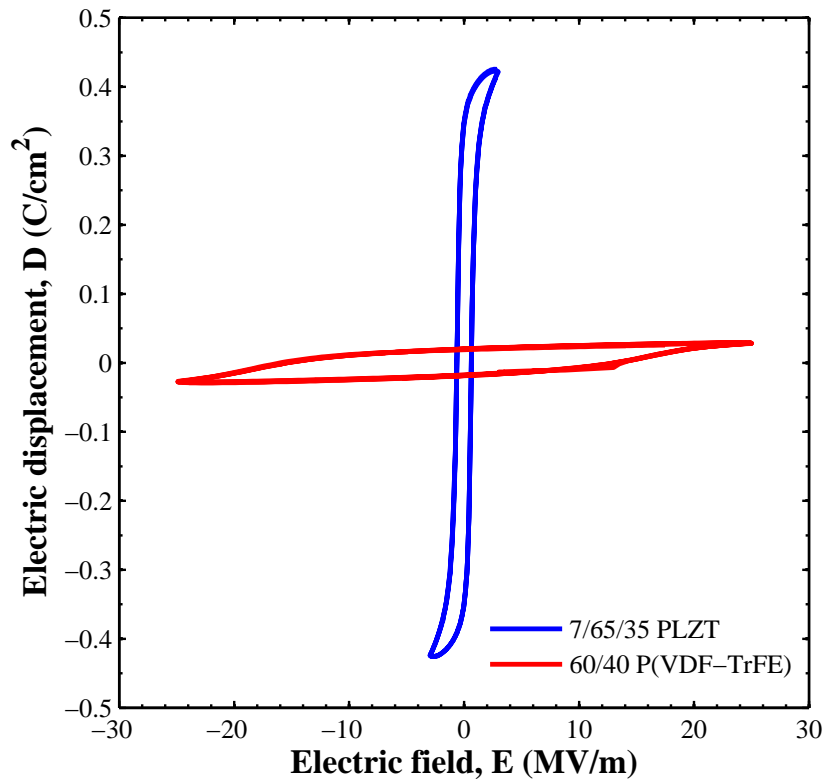
Figure 2.9: Isothermal D-E loops generated by 8/65/35 PLZT and 60/40 P(VDF-TrFE) measured at room temperature.

Figure 2.9 compares the isothermal D-E loops measured at room temperature for 8/65/35 PLZT and 60/40 P(VDF-TrFE). It shows that although PLZT ceramics possess lower dielectric breakdown compared to co-polymer P(VDF-TrFE), the PLZT materials features

significantly larger polarization and electric displacement. To produce very large energy densities, it is necessary to identify materials possessing both large polarization changes and high dielectric strength.

2.9 Heat transfer modes and Olsen cycle
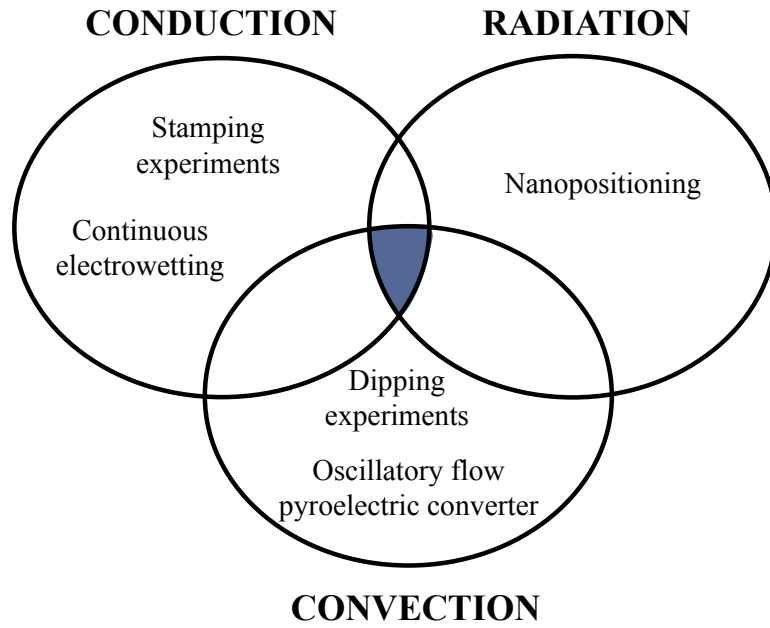
Figure 2.10: Experiments using heat conduction, nanoscale radiation, and convective heat transfer to cool and heat a pyroelectric element between T_{cold} and T_{hot} during the Olsen cycle.

Figure 2.10 identifies conduction, convection, and radiation as three possible heat transfer mechanisms for cooling and heating a pyroelectric material between T_{cold} and T_{hot} during the Olsen cycle. The following subsections summarize previous studies implementing the Olsen cycle with forced convection and nanoscale radiation.

2.9.1 Dipping experiments

A simple method for implementing the Olsen cycle is to successively dip the PE in hot and cold baths under different temperatures and specified electric fields [6]. The time-dependent heating and cooling is achieved by forced convection. The experimental setup and technique is described in detail in Chapter 3. The so-called "dipping experiments" are performed to assess the maximum amount of energy and power that can be generated under somehow idealized conditions without considering challenges associated with heat transfer limitations and devices assembly. Moreover, it facilitates the rapid screening for promising pyroelectric materials to be used in energy harvesting devices.

Olsen et $al.$ [5] performed such "dipping experiments" on 70-100 μm thick 60 mol.%/40 mol.% P(VDF-TrFE) films in hot and cold 100 cSt silicone oil baths at 25 and 100-120°C, respectively. The low electric field was kept constant at 0.2 MV/m and the high electric field E_H varied between 20 and 60 MV/m. A maximum output energy density of 900 J/L/cycle was reported at 0.125 Hz for $T_{hot} = 120^o$C and $E_H = 50$ MV/m. This corresponds to a power density of 112.5 W/L. However, it remains unclear whether these experimental results were averaged over multiple cycles and if they were repeatable.

Ikura [4] reported a maximum power density of 13.3 W/L for 60/40 P(VDF-TrFE) subjected to dipping experiments at 0.256 Hz. The operating temperatures were between 58 and 76°C while the electric field was cycled between 4 and 48 MV/m. Khodayari et $al.$ [29] performed the Olsen (or Ericsson) cycle on [110]-poled single crystal PZN-4.5PT and generated 24.4 W/L at 0.1 Hz for temperatures between 100 and 160°C and electric field between 0 and 1.0 MV/m. Meanwhile, Navid et $al.$ [6] performed the Olsen cycle on commercial, purified, and porous 60/40 P(VDF-TrFE) films under quasiequilibrium conditions. The latter refer to operations when the electric displacement reached a steady state during isoelectric field heating (process 2-3) and cooling (process 4-1) before the electric field was varied to perform processes 3-4 and 1-2, respectively. The 60/40 P(VDF-TrFE) films were dipped into cold and hot 50 cSt silicone oil baths at 25°C and 100-120°C, respectively. The low electric field was $E_L = 20$ MV/m and the high electric field E_H varied between 30 and 60 MV/m. The

maximum power density generated were 58 W/L, 36 W/L, and 18 W/L for commercial, purified, and porous films, respectively [6]. In addition, Kandilian et al. [53] studied the pyroelectric energy generation of 140 μm thick single crystal PMN-32PT capacitors poled in the [001] direction. The material was alternatively dipped into a cold silicone oil bath at 80°C and a hot one with temperature ranging from 130 to 170°C. The electric field was cycled between 0.2 and 0.9 MV/m. A maximum energy density of 100 J/L/cycle was obtained at 0.049 Hz, corresponding to a power density of 4.92 W/L, for processes performed under quasiequilibrium conditions. McKinley et al. [58] performed the same procedure on [001]-poled PZN-5.5PT and generated 11.7 W/L for temperatures between 100 and 190°C and electric field between 0 and 1.5 MV/m.

Recently, Lee et al. [86] performed the dipping experiments on relaxor ferroelectric 8/65/35 PLZT. A maximum energy density of 888 J/L/cycle was generated at 0.0178 Hz, corresponding to a power density of 15.8 W/L, for operating temperatures between 25 and 160°C and electric field cycled between 0.2 and 7.5 MV/m. Chin et al. [87] performed a similar procedure on 9.5/65/35 PLZT ceramics and achieved a maximum power density of 55 W/L at 0.125 Hz. The Olsen cycle was performed between 3 and 140°C and electric field from 0.2 to 6.0 MV/m. These studies [86, 87] demonstrated that the energy conversion performance of PLZT is strongly dependent on the material composition and operating temperatures and electric fields. In fact, T_{Curie} was reported to be -25, -10, 65, 150, 240, and 310°C for the 65/35 Pb/Ti ratio and $x = 10$, 9, 8, 7, 6, and 5 mol.%, respectively [68]. An increase in lanthanum dopant concentration hinders the onset of long-range ferroelectric order upon cooling [69]. This contributes to Curie temperature reduction from 310 to -25°C as lanthanum doping level increases from 5 to 10 mol.% [69]. Additionally, the remnant polarization and dielectric constant of rhombohedral ferroelectric x/65/35 PLZT were large compared to other PLZT compositions [76].

These results suggest that PLZT is a very promising pyroelectric material to employ in pyroelectric converters. The lanthanum concentration in PLZT can be advantageously adjusted in order to match the temperature range available in a particular application. The power output of pyroelectric converters implementing the Olsen cycle using conduction

[52, 88–90], convection [5, 7, 19–22, 50], or radiation [31] could also be significantly improved by employing a multistaging technique [22]. The latter consists of strategically placing a series of pyroelectric materials in the order of increasing T_{Curie} between a cold and a hot temperature source. This could be achieved by superimposing PLZT films with increasing amount of La doping.

2.9.2 Forced convection devices

The power output and efficiency of a pyroelectric converter undergoing the Olsen cycle can be significantly improved by using (1) multistaging [22] and (2) heat regeneration [19] during the Olsen cycle. Multistaging involves the placement of different pyroelectric materials with increasing Curie temperatures from the cold to the hot sources. Heat regeneration reduces heat losses from the system by cycling the heat required to increase the temperature of the PE back and forth between itself and the working fluid. It has been established theoretically that pyroelectric conversion based on heat regeneration using an oscillating working fluid and the Olsen cycle can reach Carnot efficiency between a hot and a cold thermal reservoir [36]. However, limitations in reaching Carnot efficiency include (i) leakage current, (ii) heat losses to the surrounding, and (iii) sensible (thermal) energy required to heat the material.

Several prototypical pyroelectric energy converters [19–22, 36] implementing the Olsen cycle were designed and built in the 1980's. Olsen *et al.* [5, 19–22] assembled the only regenerative and multistage device built to date using 250 μm thick lead zirconate stanate tinanate (PZST) as the pyroelectric materials and silicone oil with viscosities of 50 and 200 cSt as the working fluids. The electric field was cycled between 4 and 28 kV/cm. The cold and hot source temperatures were 145 and 178°C, respectively. A piston was used to vertically oscillate the working fluid back and forth between a cold and a hot source [22]. Temperature oscillations within the PE films were achieved by laminar forced convection between the silicone oil and the PE. A maximum power density of 33 W/L was obtained at 0.26 Hz. The maximum efficiency of 1.05% was achieved at 0.14 Hz, corresponding to 12% of the Carnot efficiency. Moreover, due to the high cost of PZST per Watt generated

($10,000/W), Olsen *et al.* [36] built a device using inexpensive 30 to 70 μm thick 73/27 mol.% P(VDF-TrFE) films sandwiched between electrodes and rolled in a spiral stack placed into a cylindrical chamber containing silicone oil. The maximum output energy density of this device was 30 J/L/cycle at 0.079 Hz, while operating at temperatures between 20 and 90°C and electric fields between 230 and 530 kV/cm. In these prototypes, pumping was performed by a step motor with a piston amplitude of 8-10 cm. Ceramic stacks were used to ensure laminar flow of working fluid over the pyroelectric elements as turbulence would result in mixing of cold and hot fluids, therefore disrupting the temperature gradients.

More recently, Nguyen *et al.* [7] assembled and operated a prototypical pyroelectric converter using 60/40 P(VDF-TrFE). The experimental design was inspired by the device assembled by Olsen *et al.* [36] and informed by numerical simulations performed by Navid *et al.* [26]. The maximum energy density was 130 J/L/cycle at 0.061 Hz between 66.4 and 83°C and 202 and 379 kV/cm. In addition, the maximum power density obtained was 10.7 W/L at 0.12 Hz between 67.3 and 81.4^{o}C and 202 and 379 kV/cm [7].

2.9.3   Nanoscale radiation

Plank's blackbody radiation theory imposes a limit on the maximum radiative transfer between two objects at a given temperature. It is only applicable when the gap between participating thermal radiation objects is much larger than the peak radiation wavelength (d $>>$ λ_{max}) [91]. According to Wien's displacement law (λ_{max}T = 2898 μm·K), the peak radiation wavelength λ_{max} is around 10 μm for the temperature range between $\sim$ 300 and 400K. However, for gap sizes much smaller or comparable to the peak wavelength (d $<<$ λ_{max}), thermal radiation can be increased by three orders of magnitude [92]. The thermal radiation enhancement in the near-field is attributed to evanescent waves tunneling through small gap interfaces [31]. Wave tunneling relies on evanescent waves which decay exponentially with distance away from the surface at which they are formed. These non-propagating waves only transport energy when an object is brought close to an emitter. In the case of dielectric materials, surface waves called surface phonon polaritons are excited by infrared

radiation due to coupling between the electromagnetic field and optical phonons [92]. The photon tunneling at dielectric interfaces contribute to significant increase in radiative heat transfer. Recent studies [91, 93, 94] have reported strong near-field effects between a silica microsphere and flat silica surface as well as between two plane parallel glass surfaces. Consequently, it is advantageous to combine nanoscale radiation and pyroelectric energy conversion for harvesting low-grade waste heat.

Devices previously operated by Olsen *et al.* [19–22, 36] and Nguyen *et al.* [7] utilized laminar forced convection between a working fluid and the PE. In these devices, the flow must be laminar since turbulence would disrupt the proper oscillation temperature gradients of the PE [31]. However, laminar flow restricted the operating frequencies of the device and as a result the energy harvested was limited. On the contrary, radiative heat transfer takes place at the speed of light and therefore a pyroelectric material can reach its phase transition temperature rapidly during the Olsen cycle when heated by nanoscale radiation [31]. Furthermore, these pyroelectric converters utilized a piston to oscillate the working fluid over the PE. By replacing the piston with a nanoscale piezoelectric actuator that consumes less than ~ 30 mW, the power consumption of a pyroelectric converter can be minimized and the device's thermal efficiency can be increased.

Recently, Fang *et al.* [31] performed numerical simulations of a pyroelectric converter harvesting nanoscale thermal radiation using 60/40 P(VDF-TrFE) and 0.9PMN-PT. The converter consists of a composite pyroelectric plate oscillating between hot and cold aluminum plates separated by nano-sized gaps [31]. The aluminum plates were coated with a 1 μm thick SiO_2 absorbing layer to further enhance radiative heat fluxes. The latter can be explained by the fact that silicon dioxide SiO_2 is a dielectric material exhibiting large absorption index at wavelengths around 10 μm. The PE plate consisted of a 60/40 P(VDF-TrFE) film or a 0.9PMN-PT composite thin film also coated with SiO_2. Note that in these simulations, the device was assumed to operate under vacuum to minimize friction on the oscillating PE plate and to reduce heat losses to the surrounding. Indeed, the presence of air in the nanogap may cause heat conduction to dominate nanoscale thermal radiation.

The simulations showed that an efficiency of 0.2% and an electrical power output of 0.84

mW/cm^2 was possible by using 60/40 P(VDF-TrFE) with cold and hot sources at 273 and 388 K, respectively. For multilayer composite thin film 0.9 PMN-PT, an efficiency of 1.35% and a power output of 6.5 mW/cm^2 was predicted for cold and hot plates at 283 and 383 K [31]. The simulated operating frequency was 1.2 Hz, more than ten times greater than that of actual devices employing laminar convective heat transfer [6, 7, 31]. Unfortunately, maintaining a nanoscale gap ($\sim$ 100 nm or less) between the PE and the hot or cold plates can be challenging. In the limiting case, the PE can be placed in thermal contact with the hot and cold sources. Then, heat is transferred by conduction. The thermal response of the PE heated by heat conduction is expected to be slower than that obtained with other heat transfer modes. Indeed, conductive heat transfer is a diffusive process limited by thermal contact resistance between the PE and the cold or hot plates.

CHAPTER 3

Pyroelectric Waste Heat Energy Harvesting Using Heat Conduction

This chapter is concerned with practical implementnation of the Olsen cycle using conductive heat transfer on 60/40 P(VDF-TrFE) films. The effects of various operating conditions were systematically investigated.

3.1 Experiments

3.1.1 Sample

Commercial 60/40 P(VDF-TrFE) films were synthesized by the same method described in Ref. [51]. A hydraulic press was utilized to form the P(VDF-TrFE) pellets into thin films. The PE used in the present study was 60.45 μm thick and approximately 2 cm in diameter. The cross-sectional area of the aluminum electrodes was 1 cm x 1 cm.

3.1.2 Experimental setup

Figure 3.1 shows a schematic of the experimental setup. It consisted of a thermal and an electrical sub-system.

Thermal subsystem

The thermal system consisted of two 3 cm x 2.5 cm x 1.27 cm cold and hot aluminum blocks. They were used as the cold and hot sources maintained at the temperatures T_C and

T_H, respectively. A 50 W Omega CS-10150 cartridge heater was embedded in the hot block and its temperature T_H was controlled by an Omega CN-7823 proportional integral derivative (PID) temperature controller. The cold block was maintained at room temperature by free convection to the surrounding air at atmospheric pressure. A thermal conductive epoxy Omegabond-200 [95] layer with high electrical resistance and high thermal conductivity was applied on the top surfaces of both blocks. It electrically isolated the PE's electrodes from the metallic blocks while minimizing the thermal contact resistance. Its thermal conductivity was 1.384 W/m·K and its electrical resistivity was on the order of $10^{15}\Omega$·cm [95]. The PE sample was taped to the flat base of a wooden stamp. The wooden stamp allowed for convenient and safe handling of the film under various applied pressures. J-type thermocouples were embedded at the center of the hot and cold blocks. In addition, a J-type thermocouple was attached to the top of the film in such a way that it was in thermal contact but not in electrical contact with the electrodes. Since the film thickness was only tens of micrometers, the temperatures measured by the thermocouple were assumed to be the same across the film.

Electrical subsystem

Figure 3.2 shows the electrical subsystem used for performing the Olsen cycle. The electrical subsystem served two main purposes:

1. To control the voltage applied to the pyroelectric element and impose V_L or V_H at appropriate time during the Olsen cycle (see Figure 2.4).

2. To determine the power generated by the pyroelectric element by measuring the voltage V_{PE} and charges q_{PE} displayed by the pyroelectric elements.

It consisted of a modified Sawyer-Tower circuit [54] to apply the required electric field and to measure charge Q collected on the PE electrodes. A resistive voltage divider was placed in parallel with the Sawyer-Tower bridge to control the electric field applied to the material. Voltage V_1 across the film capacitor $C_1 = 9.82$ μF was measured using a Burr-Brown DIFET electrometer (OPA128) to minimize discharge of the capacitor connected to
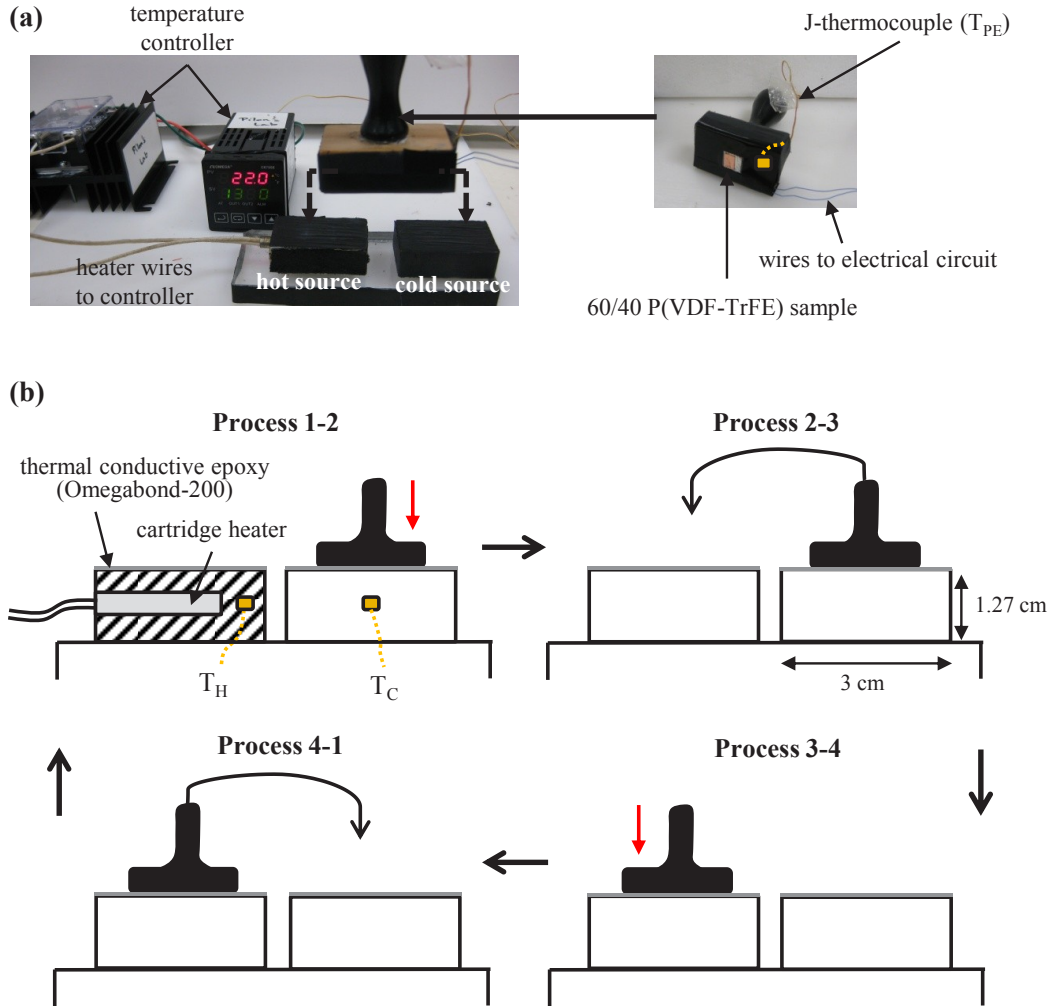
Figure 3.1: (a) Thermal subsystem used to create periodic temperature oscillations during the Olsen cycle as well as the PE-stamp assembly (b) Schematic of each process in the Olsen cycle during stamping experiments.
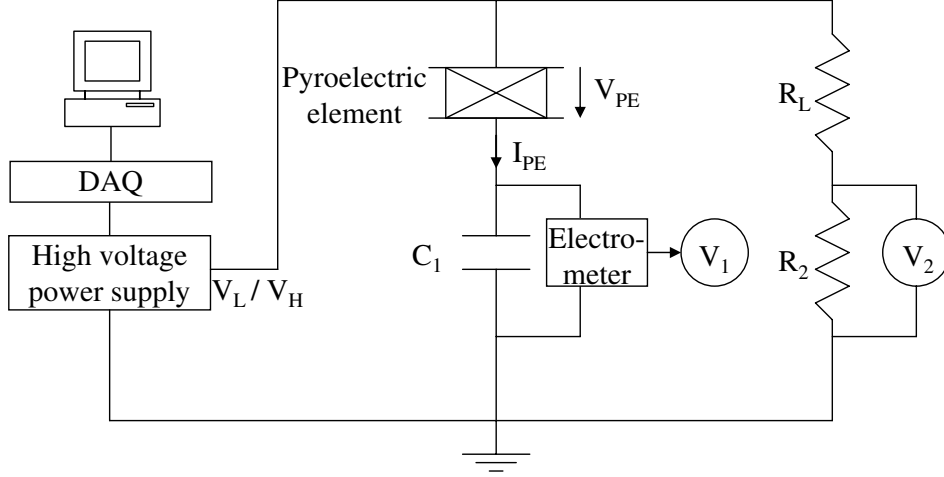
Figure 3.2: Electrical circuit used in the stamping experiments to prepole and measure the electrical resistivity ρ_R of the pyroelectric element and to perform the Olsen cycle.

an IOtech 3000 series data acquisition system (DAQ). The resistor $R_L = 10.55$ $M\Omega$ acted as a voltage divider to scale down the voltage across the resistor $R_2 = 21.8$ $k\Omega$ in order to match the maximum voltage input of 10 V of the DAQ. The electric field was applied by a computer generated function through the DAQ connected to a TREK 610E high voltage power supply. The magnitude of the film electric displacement D was defined as

$$D = \frac{Q}{A} = \frac{C_1 V_1}{A} \tag{3.1}$$

where $A = 1$ cm^2 is the film surface area. The magnitude of the electric field across the PE was calculated from Ohm's law and Kirchhoff's law and expressed as

$$E = \frac{V_{PE}}{b} = \frac{V_2(1 + R_L/R_2) - V_1}{b} \tag{3.2}$$

where b is the pyroelectric film thickness. Then, the D-E diagram can be generated using this approach.

3.1.3 Electric poling

Electric poling is a process in which dipole moments of individual crystallite are aligned in the direction of the applied electric field [56]. Poling also increases the crystallinity of

the pyroelectric material and its orientational order [96]. Thus, the process increases the material electrical resistivity [97].

P(VDF-TrFE) is subject to leakage current particularly at high electric fields and/or high temperature [25, 36, 98, 99]. Leakage current refers to the phenomenon whereby charges that accumulate at the surface of the pyroelectric element are transported through its body [6]. In this process, energy is dissipated as Joule heating and in turn reduces the energy and power densities generated [7]. The leakage current is expressed as

$$i_L = C_1 \frac{dV_1}{dt} \tag{3.3}$$

where V_1 is the voltage across the capacitor C_1 as shown in Figure 3.2. The same circuit was used to prepole the pyroelectric films. Then, the electrical resistivity of the PE was estimated as

$$\rho_R = \frac{V_{PE}A}{i_L b} \tag{3.4}$$

Several techniques can be used to reduce leakage current. First, the maximum operating temperature T_{hot} and maximum electric field E_H in the Olsen cycle can be reduced. In addition, increasing the frequency of the pyroelectric cycle can reduce leakage current by limiting the time during which the PE operates at E_H and T_{hot}. Furthermore, purifying pyroelectric materials may reduce leakage by eliminating defects in the film [25]. Finally, the PE can be poled prior to performing the Olsen cycle to increase its electrical resistance [51]. Maintaining a non-zero electric field ($E_L \simeq 200$ kV/cm) was recommended to keep the P(VDF-TrFE) films properly poled during the cooling Process 1-2 in the Olsen cycle [5, 25, 36, 51].

3.1.4 Experimental procedure

First, the P(VDF-TrFE) film was poled under an electric field of 200 kV/cm to increase its electrical resistivity [51]. The temperature of the hot block was set to $T_H = 90^oC$. Then, the stamp-assembly supporting the PE was brought in thermal contact with the hot block for 70 minutes. The PE resistivity was monitored over time until it reached a steady state. Then, poling was complete and the Olsen cycle was performed.

To create the time-dependent temperature oscillations required in the Olsen cycle, the PE was successively heated and cooled by manually pressing it against the hot and cold blocks. The time required for the film to reach the temperatures T_H and T_C of the hot and cold reservoirs (Processes 2-3 and 4-1) was greater than that to completely charge or discharge the PE (Processes 1-2 and 3-4). Thus, sufficient time ($\sim$8 s) was allowed in Process 4-1 for the sample's electric displacement to reach steady-state ($\partial D/\partial t = 0$). However, due to large leakage current at high temperatures, the sample was placed on the hot block for only $\sim$4 s (Process 2-3) before lowering the electric field (Process 3-4). In other words, Process 2-3 was terminated before the sample had completely discharged and before a steady-state temperature had been reached. The phase transition may have been incomplete.

The epoxy layer that electrically insulated the cold and hot block, introduced a thermal contact resistance and reduced heat transfer between the PE and hot or cold blocks. In fact, its thermal conductivity was small compared with that of metals and its surface was uneven. Therefore, pressure was applied between the PE and the hot or cold blocks to try to reduce the thermal contact resistance.

The Olsen cycle was performed for high electric fields E_H ranging from 290 to 475 kV/cm. The low electric field E_L was set as 200 kV/cm to prevent depoling of the film during the cycle [6]. The cold and hot source temperatures were maintained at 25 and 110°C, respectively, by analogy with the "dipping experiments" reported in Ref. [6]. In the "dipping experiments", commercial P(VDF-TrFE) films immersed in silicone oil baths could withstand electric fields as high as 600 kV/cm [51]. Unfortunately, in the present "stamping experiments", the film was unable to sustain electric fields larger than 475 kV/cm in air because the dielectric breakdown field of air is lower than that of silicone oil [100].
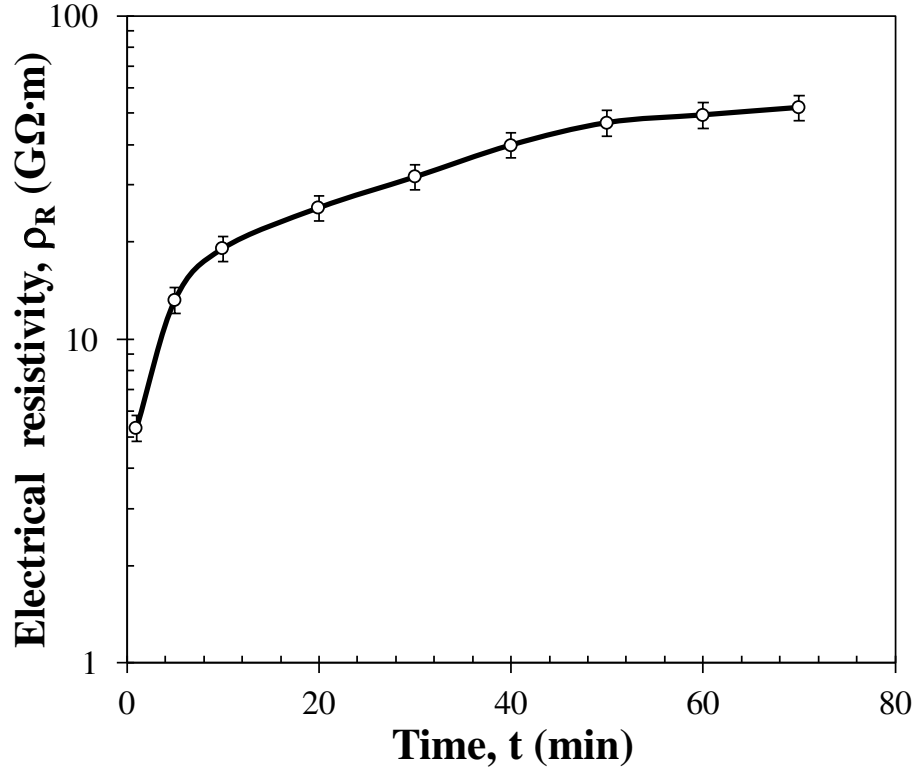
Figure 3.3: Electrical resistivity of a 1 cm x 1 cm area and 60.45 μm thick 60/40 P(VDF-TrFE) film poled at $E = 200$ kV/cm and $T_{hot} = 90^{o}$C as a function of time.

3.2 Results and discussion

3.2.1 Electrical resistivity

Figure 3.3 plots the film electrical resistivity ρ_R of the commercial 60/40 P(VDF-TrFE) sample as a function of time during poling at $T_{hot} = 90^oC$ and $E = 200$ kV/cm. The film resistivity increased by a factor of 4.79 during the first 20 minutes of poling. After 70 minutes, it reached $5.22\text{x}10^{10}$ $\Omega\cdot$m and did not change noticeably as poling continued. The increase in film resistivity during poling was possibly attributed to the gradual transport of ionic impurities contained within the film to its electrodes [25].

3.2.2 Temperature oscillations

Figure 3.4 shows the temperature of the PE during seven consecutive Olsen cycles at frequencies ranging from 0.066 to 0.078 Hz. The cold source temperature T_C was 25^oC and the hot source temperature T_H was 110^oC. The average minimum and maximum temperatures of the PE during one cycle are denoted by T_{cold} and T_{hot}, respectively. The PE temperature oscillated between $T_{cold} = 45.2^oC$ and $T_{hot} = 94.8^oC$ on average. Note that $T_H > T_{hot}$ and $T_C < T_{cold}$ due to the thermal contact resistance between the PE and the hot or cold blocks and the relatively short time they were in thermal contact with each other.

The following subsections report on the effects of several experimental parameters which affect energy density, namely the (i) leakage current, (ii) high electric field E_H, (iii) hot source temperature T_H, and (iv) pressure applied between the aluminum blocks and the PE. The experimental data obtained in this study are summarized in Table 3.1.

3.2.3 Effect of leakage current

Figure 3.5 plots the D-E diagram obtained for an Olsen cycle performed under electric fields between $E_L \simeq 200$ and $E_H \simeq 350$ kV/cm and cold and hot sources at $T_C = 25^oC$ and $T_H = 110^oC$, respectively. It indicates that the Olsen cycle did not start and end at the same point, as Points 4 and 4' did not coincide. The offset was caused by leakage
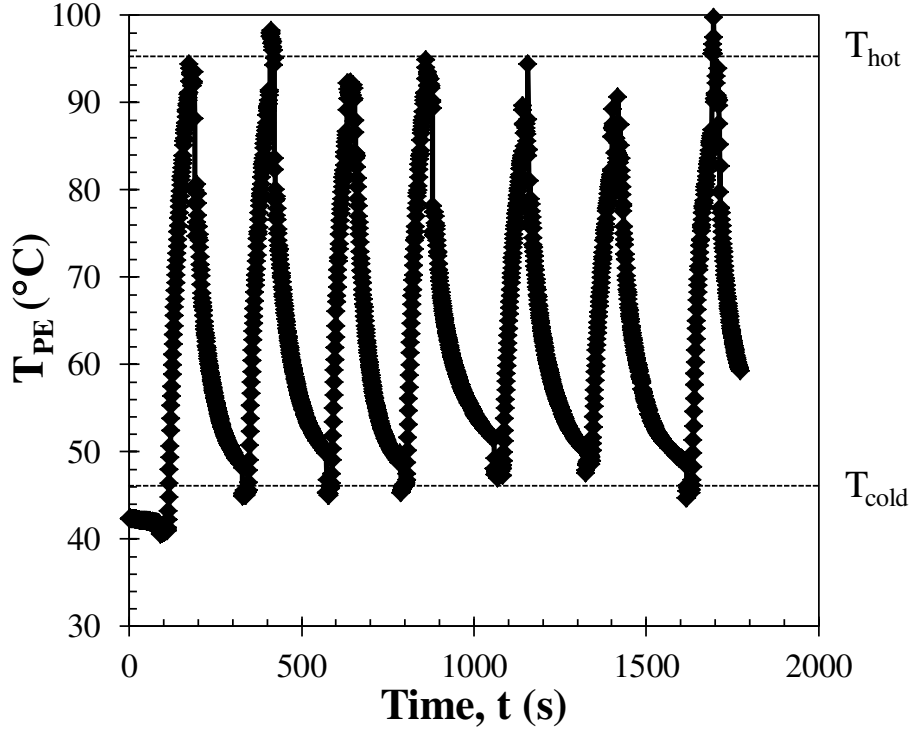
Figure 3.4: Temperature of the PE over seven consecutive Olsen cycles. The operating conditions were $T_C = 25^oC$, $T_H = 110^oC$, $E_L = 200$ kV/cm, and $E_H = 350$ kV/cm while the cycle frequency ranged from 0.066 to 0.077 Hz.

Table 3.1: List of operating conditions and results obtained in the stamping experiments. The imposed conditions were $E_L = 200$ kV/cm, $T_C = 25^oC$, $T_H = 110^oC$.

| E_H | N_D | P_D | ΔT_{PE} | T_{cold} | T_{hot} | f |
kV/cm	J/L/cycle	W/L	^oC	^oC	^oC	Hz
290	77.8	4.99	33.9	52.2	86.1	0.064
300	101	6.03	56.3	42.7	99.0	0.060
320	145	10.80	41.2	50.4	91.6	0.075
330	148	9.02	49.7	47.0	96.7	0.061
350	**155**	10.3	55.1	46.8	99.7	0.066
350	146	**11.2**	49.6	44.8	99.4	0.077
350	154	10.5	48.2	49.3	97.5	0.068
350	143	10.4	46.4	48.0	94.4	0.073
350	115	8.90	41.7	47.5	89.2	0.077
379	150	9.72	37.5	55.0	92.5	0.064
475	72.6	5.38	56.3	40.7	97.0	0.074
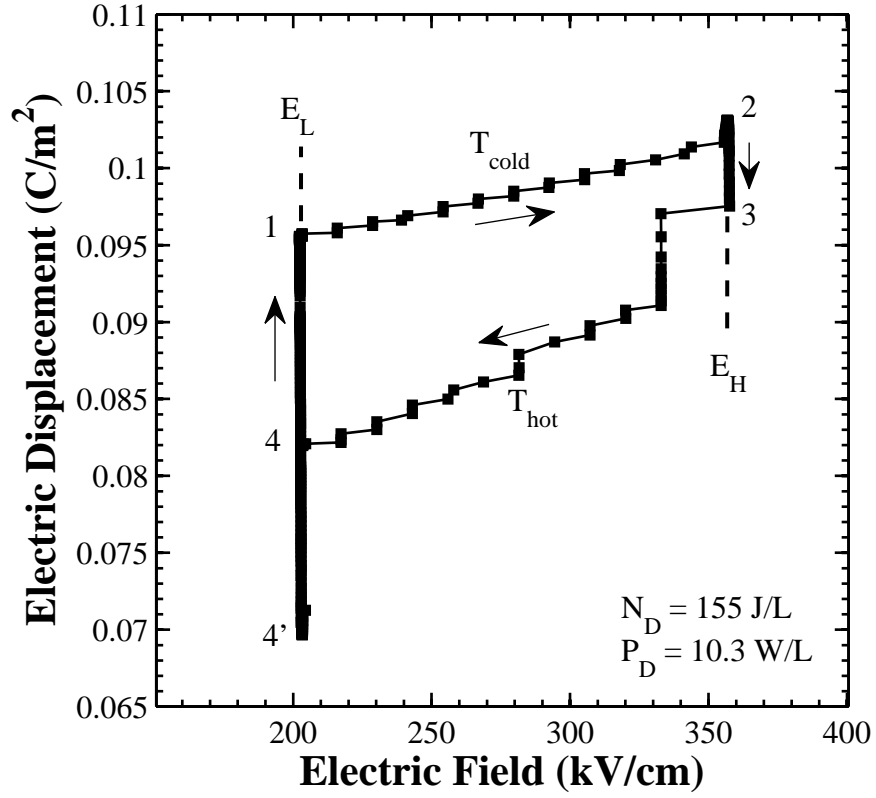
Figure 3.5: Experimental Olsen cycle in the electric displacement versus electric field (D-E) diagram obtained with a 1 cm x 1 cm area and 60.45 μm thick 60/40 P(VDF-TrFE) film, between $T_C = 25^oC$ and $T_H = 110^oC$ with $E_L = 200$ kV/cm and $E_H = 350$ kV/cm.

current through the PE film [6]. It reduced the electrical energy produced during the Olsen cycles. Indeed, the leakage current increases with increasing temperature and applied electric field [6]. Kouchachvili *et al.* [24] attributed the leakage current to the presence of ionic impurities within the PE film. The current-carrying impurities become mobile and drift towards the electrodes under high temperatures and high electric potentials. Note that Process 3-4 did not follow a smooth path because the phase transition from ferroelectric to paraelectric was incomplete during Process 2-3. Here, an energy density of 155 J/L/cycle was estimated by applying the trapezoidal rule on the 1-2-3-4 region of the D-E curve.

3.2.4 Effect of hot source temperature T_H

The Curie temperature of 60/40 P(VDF-TrFE) was reported to be 66^oC under zero applied electric field [51], 92.5^oC at 300 kV/cm, and 120^oC at 527 kV/cm [5]. When the hot source temperature T_H was set below 110^oC, the temperature T_{hot} reached by the film during the Olsen cycles fell below the Curie temperature when the applied high electric field exceeded 350 kV/cm. As a consequence, a complete ferroelectric to paraelectric transition was not observed for $E_H > 350$ kV/cm. However, when the hot source temperature was increased from 110 to 130^oC to further increase T_{hot}, electrical sparks were observed during the Olsen cycles. We speculate that the short-circuit was due to the reduction in the dielectric strength of air near the hot block with increasing temperatures [100]. In addition, increasing the hot source temperature beyond 110^oC resulted in excessive leakage current. Under these conditions, the rate of surface charges conducting through the film exceeded the rate of electrical discharge during Process 2-3 over time. This resulted in crossovers in the D-E curves between Processes 1-2 and 3-4. Therefore, the hot source temperature T_H of 110^oC was found to be optimum to maximize energy density for 60/40 P(VDF-TrFE).

Effect of high electric field E_H

Figure 3.6 shows the energy density produced in the stamping experiments as a function of applied high electric field E_H spanning from 290 to 475 kV/cm. The cold and hot source

temperatures were 25°C and 110°C, respectively. The low electric field E_L was set as 200 kV/cm and the cycles operated at frequencies between 0.060 and 0.077 Hz. The range of high electric field E_H was selected by analogy with our previous pyroelectric energy generation experiments using 60/40 P(VDF-TrFE) [6, 7]. Figure 3.6 indicates that the energy density increased with increasing E_H up to 350 kV/cm before decreasing for higher electric field. The largest amount of energy generated was 155 J/L/cycle for $E_H = 350$ kV/cm at 0.066 Hz, corresponding to a power density of 10.3 W/L. The associated cycle was shown in Figure 3.5. This can be explained by the fact that as the high electric field E_H increased, the electric field span (E_H - E_L) increased, resulting in large energy and power densities produced during the Olsen cycle according to Equations (2.9) and (2.10). However, leakage current was also found to increase with increasing electric field. Overall, increasing E_H beyond 350 kV/cm resulted in a reduction in the generated energy density.

3.2.5   Effect of applied pressure

The thermal contact resistance between the PE and aluminum blocks can be reduced by increasing the pressure applied to the film [101]. In turn, this could reduce the time necessary for the sample to reach the cold and hot source temperatures, thus increasing the power density. The pressure applied to the PE throughout the Olsen cycle varied from 0 to ∼200 kPa. However, application of excessive pressure (> 200 kPa) caused electrical short-circuits in the PE when in contact with the hot block. This could be attributed to the development of microcracks between the electrodes when pressed against the uneven aluminum blocks. No significant effects on the heating and cooling times were observed for applied pressures smaller than 200 kPa.

Discussion

The Olsen cycle requires the application of high electric fields across the pyroelectric material. The corresponding voltages can be prohibitively large for implementation in devices. However, the use of very thin film would substantially reduce the voltage required. Then,
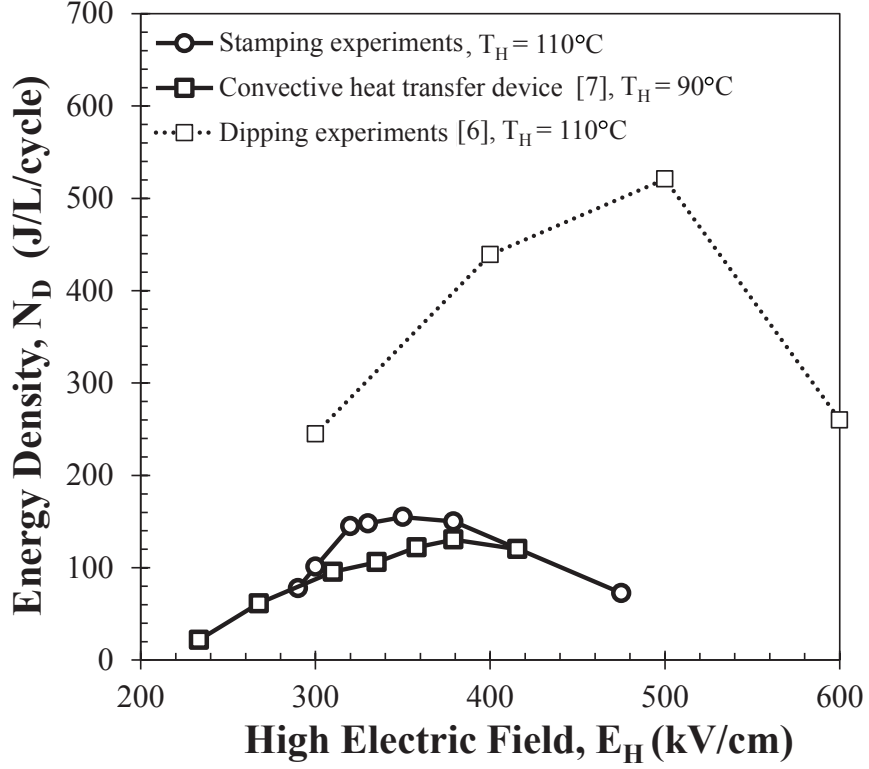
Figure 3.6: Comparison of energy density N_D as a function of high electric field E_H obtained in the stamping experiments with previously reported experiments. Operating conditions were (1) $E_L = 200$ kV/cm, $E_H = 290$ to 475 kV/cm, $T_C = 25^oC$ (present study), (2) $E_L = 200$ kV/cm, $E_H = 300$ to 600 kV/cm, $T_C = 25^oC$ (dipping experiments) [6], and (3) $E_L = 202$ kV/cm, $E_H = 233$ to 475 kV/cm, $T_C = 25^oC$ (convective heat transfer device) [7].

the Olsen cycle may be performed by using several batteries connected in series. Leakage current however may increase with decreasing film thickness [102, 103].

3.2.6 Comparison with other heat transfer modes

Figure 3.6 compares the energy density obtained for 60/40 P(VDF-TrFE) as a function of high electric field E_H in the present study with results reported for "dipping experiments" [6] and the pyroelectric converter constructed by Nguyen *et al.* [7]. It indicates that the heat transfer mechanism used to generate temperature oscillations played an important role in the amount of pyroelectric energy generated. Figure 3.6 also establishes that the largest energy density generated in the "stamping experiments" (155 J/L/cycle) exceeded the 130 J/L/cycle obtained with the device reported in Ref. [7] for similar operating conditions, $T_{hot} = 83^oC$ and $E_H = 223.7$ to 415.6 kV/cm. However, it was significantly smaller than the energy densities obtained in "dipping experiments" [6]. This can be attributed to the higher PE temperatures ($T_{hot} = 100^oC$) and higher applied electric fields ($E_H = 600$ kV/cm) imposed in the "dipping experiments" [6] compared with $T_{hot} = 87$ to 96^oC and $E_H = 290$ to 475 kV/cm in the "stamping experiments". This was made possible by the use of silicone oil which has a larger electric breakdown field strength than air [100].

Finally, Table 3.1 indicates that the maximum values of power density and energy density did not correspond to the same operating frequency. In addition, the peak power density of 11.2 W/L at 0.077 Hz observed in the present study was a slight improvement over the 10.7 W/L at 0.12 Hz reported by Nguyen *et al.* [7]. However, the present procedure is significantly simpler to implement.

3.2.7 Comparison with other pyroelectric energy conversion methods

Attempts have been made to use the pyroelectric effect to produce electricity from temperature oscillations but without using the Olsen cycle. Unfortunately, this approach resulted in relatively small power density regardless of the heating and cooling methods considered as predicted by van der Ziel [38]. Cuadras *et al.* [32] blew periodic pulses of hot and cold

air to create temperature oscillations in PZT and PVDF samples. They achieved a power density of 0.0012 W/L at 0.0088 Hz with 100 μm thick PZT for temperatures between 31 and 62°C. Mane *et al.* [33] used infrared radiation for heating and natural convection for cooling lead zirconate titanate (PZT), pre-stressed PZT composite, and single-crystal PMN-30PT samples. The maximum power density achieved was 0.00864 W/L with 270 μm thick PMN-30PT at frequency 0.1 Hz corresponding to a temperature swing of about 8.4^{o}C. Similar experiments using radiative heating were performed by Buchanan *et al.* [104] on 1 μm thick PZT 90/10 samples. They obtained about 0.0016 W/L at 5 Hz between 80 and 110°C. Ravindran *et al.* [35, 88] operated a pyroelectric generator that utilizes the pressure expansion of air to move heat from a heat source to 200 μm PZT attached to a heat sink. The authors reported a power density of 0.15 W/L at 0.42 Hz for a temperature difference of 79.5 K. Chang *et al.* [105] built a pyroelectric energy harvesting device that utilizes shape memory alloy springs to oscillate a LaTiO$_3$ sample in thermal contact between a hot and a cold reservoir maintained at 310 and 300 K, respectively. The maximum power produced was 0.0521 W/L at 0.01 Hz. Finally, Sebald *et al.* [106] generated a 2°C temperature variation across 850 μm thick single crystal PMN-25PT and harvested 3.76 W/L at 1 Hz.

The above results should be compared with those achieved by performing the Olsen cycle. In fact, Table 3.2 compares the maximum power density achieved using either the Olsen cycle or the pyroelectric effect for different materials, temperature ranges, and frequencies. In particular, Olsen *et al.* [22] obtained 33.9 W/L in a device at 0.26 Hz between 150 and 180°C using PZST. Nguyen *et al.* [7] achieved 10.7 W/L in a device similar to that of Olsen *et al.* [22] but operating at 0.12 Hz between 67.3 and 81.4^{o}C using 60/40 P(VDF-TrFE). Ikura [4] reported a maximum power density of 13.3 W/L for 60/40 P(VDF-TrFE) subjected to dipping experiments at 0.256 Hz between 58 and 76°C. Similarly, Navid *et al.* [6] reported 52.1 W/L for 60/40 P(VDF-TrFE) dipping experiments at 0.10 Hz between 25 and 110°C. In the present study, we have achieved 11.2 W/L at 0.077 Hz between 44.8 and 99.4^{o}C using 60/40 P(VDF-TrFE) and a new stamping technique. Other results for single crystal PMN-32PT [53] and PZN-5.5PT [58] are also reported in Table 3.2. Overall, performing the Olsen cycle enables one to generate significantly more power than by simply using the pyroelectric

effect.

Table 3.2: Comparison of maximum power density achieved using either the Olsen cycle or the pyroelectric effect for different materials, temperature ranges, and frequencies.

Material	Technique	T_{cold} ^oC	T_{hot} ^oC	f Hz	P_D W/L	Ref.
PZST	Olsen cycle	156.8	177.4	0.26	33.9	[22]
73/27 P(VDF-TrFE)	Olsen cycle	23.0	67.0	0.079	2.38	[36]
60/40 P(VDF-TrFE)	Olsen cycle	58.3	76.5	0.256	13.3	[4]
60/40 P(VDF-TrFE)	Olsen cycle	67.3	81.4	0.12	10.7	[7]
60/40 P(VDF-TrFE)	Olsen cycle	25.0	110.0	0.10	52.1	[6]
PZN-4.5PT	Olsen cycle	100.0	160.0	0.10	24.3	[29]
PZN-5.5PT	Olsen cycle	100.0	190.0	0.10	11.7	[58]
PMN-32PT	Olsen cycle	80.0	170.0	0.049	4.92	[53]
PZT	Pyroelectric effect	80.0	110.0	5.0	1.2×10^{-3}	[104]
PZT	Pyroelectric effect	31.0	62.0	0.00875	1.6×10^{-3}	[32]
PZT	Pyroelectric effect	14.0	93.5	0.42	0.15	[35, 88]
LiTaO$_3$	Pyroelectric effect	27.0	37.0	0.01	5.21×10^{-2}	[105]
PMN-30PT	Pyroelectric effect	32.0	40.4	0.10	8.64×10^{-3}	[33]
PMN-25PT	Pyroelectric effect	N/A	N/A	1.0	3.76	[106]

3.3   Chapter summary

This chapter reported the energy and power densities generated by subjecting 60/40 P(VDF-TrFE) films to the Olsen cycle. Heating and cooling of the film were achieved by conductive heat transfer using a stamping technique. Results were compared with data collected from a device using laminar forced convective heat transfer [7] and from dipping experiments [6]. The largest energy density generated by 60/40 P(VDF-TrFE) in this study was 155 J/L/cycle

at 0.066 Hz with cold and hot temperatures of 25 and 110°C, respectively, and electric field cycled between 200 and 350 kV/cm. These operating conditions represent a tradeoff between maximizing applied high electric field E_H and hot source temperature T_H, on the one hand, and minimizing leakage current on the other. Moreover, the energy and power densities obtained in the current study were larger than those achieved by the device assembled by Nguyen *et al.* [7]. Finally, the proposed stamping procedure can be implemented in a compact automated device.

CHAPTER 4

Pyroelectric Waste Heat Energy Harvesting Using Relaxor Ferroelectric 8/65/35 PLZT and the Olsen Cycle

This chapter is concerned with experimental measurements of energy densities generated by ferroelectric relaxor 8/65/35 PLZT undergoing the Olsen cycle. The effects of various operating conditions were systematically investigated to explore their effects on the energy and power generation.

4.1 Experiments

4.1.1 Samples

Hot isostatically pressed 8/65/35 PLZT ceramics with grain diameter around 5 μm were acquired from Aura Ceramics, Inc., New Hope, MN, USA. The specimen was cut into seven samples with thickness ranging from 290 to 720 μm using a diamond abrasive saw. Rectangular gold electrodes were sputtered on opposite faces. Electrical wires were bonded to the electrodes using conductive silver epoxy. Table 6.1 lists the thickness and the cross-sectional dimensions of each sample used in this study. Note that the electrodes in Samples 5 to 7 did not fully cover the faces. This electrode configuration was chosen in order to minimize electrical conduction (leakage current) around the samples' edges.

Table 4.1: Thickness and cross-sectional area of the different 8/65/35 PLZT samples and their electrodes investigated in this study.

Sample #	Thickness (μm)	Electrode size (cm x cm)	Sample size (cm x cm)
1	490	0.810 x 0.900	0.810 x 0.900
2	720	0.815 x 0.950	0.815 x 0.950
3	600	0.90 x 0.950	0.900 x 0.950
4	650	0.979 x 0.838	0.979 x 0.838
5	370	0.845 x 0.653	0.991 x 0.843
6	370	0.833 x 0.644	0.993 x 0.839
7	290	0.414 x 0.429	0.876 x 0.852

4.1.2 Experimental setup

Two thermally insulated beakers containing Dow Corning 100 cSt silicone oil were maintained at temperatures $T_C = T_{cold}$ and $T_H = T_{hot}$ by temperature-controlled hot plates [6,53]. J-type thermocouples were immersed in each bath to monitor and control their temperature. The samples were alternatively dipped between the cold and hot baths to create the temporal temperature oscillations required in the Olsen cycle. Sufficient time ($\sim$20 to 60 s) was given for the sample's electric displacement to reach steady-state ($\partial D/\partial t = 0$) during Processes 2-3 and 4-1 before varying the electric field and then moving the sample from one bath to the other. This ensures that the cycle was performed under quasiequilibrium conditions to achieve the maximum energy density. Note that the thermal time constant can be estimated as $\tau_t = \rho c_p / h b$ [101] where h is the heat transfer coefficient, b is the sample thickness, while ρ and c_p are the sample density and specific heat, respectively. For example, the thermal time constant was estimated to be 2.5 s for a 290 μm thick 8/65/35 PLZT sample with $\rho = 7900$ kg/m^3 [107], $c_p = 329$ J/kg.K [108], and $h = 300$ W/m^2·K corresponding to convective quenching in an oil bath [109].

The electrical subsystem used to perform the Olsen cycle consisted of a modified Sawyer-

Tower circuit [54] to apply the required electric field across the pyroelectric material and to measure the charge Q collected at the electrode surfaces. Details of the circuit used in the present study were provided in Section 3.2 and need not be repeated. This circuit was also used to measure the unipolar and bipolar D-E loops at various temperatures.

4.1.3   Experimental procedure

4.1.3.1   Isothermal D-E loops

Isothermal unipolar and bipolar D-E loops were collected at 45, 65, 100, 110, 120, 130, and 160°C for Samples 4 to 6 and at 25 and 160°C for Sample 7 using the electrical circuit previously discussed. The measurements were taken while the sample was immersed in a silicone oil bath maintained at the desired temperature. For bipolar loop measurements, a continuous triangular voltage signal was applied across the sample at 0.33 Hz, corresponding to the frequency at which the electric field was changed during isothermal Processes 1-2 and 3-4 in the Olsen cycle. The amplitude of the applied voltage corresponded to an electric field cycled between -2.5 and +2.5 MV/m. Similarly, the applied voltage for unipolar D-E loop measurements corresponded to an electric field varying from 0 to 2.5 MV/m. These measurements were taken at 0.66 Hz, corresponding to the same rate of change in electric field as that imposed to collect the 0.33 Hz bipolar D-E loops.

Moreover, the saturation polarization $P_s(T)$, the remnant polarization $P_r(T)$, and the relative permittivity $\varepsilon_r(T)$ of 8/65/35 PLZT samples were evaluated by linearly fitting the upper curves of isothermal bipolar D-E loops corresponding to a decrease in electric field from E_H to E_L as shown in Figure 2.4.

4.1.3.2   Olsen cycle

The Olsen cycle was performed on 8/65/35 PLZT at various electric fields and temperatures to investigate their respective effects on the energy generated. For example, the low electric field E_L was varied between 0 and 0.4 MV/m and the high electric field E_H from 0.4 to

7.5 MV/m. The cold source temperature T_{cold} was either 25, 45, or 65°C, while the hot source temperature was varied from 100 to 160°C. The Olsen cycles were recorded in the D-E diagram and the energy density N_D, defined in Equation (2.9), was estimated by applying the trapezoidal rule.

4.1.3.3 Physical modeling of the Olsen cycle

Recently, Kandilian *et al.* [53] developed a physical model predicting the amount of energy generated by relaxor ferroelectric materials undergoing the Olsen cycle. The model accounted for temperature-dependent properties of the material. The energy density N_D was expressed as [53]

$$N_D(E_L, E_H, T_{cold}, T_{hot}) = (E_H - E_L) \left\{ \frac{\varepsilon_0}{2} \left[\varepsilon_r(T_{cold}) - \varepsilon_r(T_{hot}) \right] (E_H + E_L) + \right.$$
$$\left. P_s(T_{cold}) - P_s(T_{hot}) + \frac{d_{33}x_3}{s_{33}} \right\} \quad (4.1)$$

where $\varepsilon_r(T_{cold})$ and $\varepsilon_r(T_{hot})$ are the low frequency relative permittivities of the pyroelectric material at the cold and hot operating temperatures T_{cold} and T_{hot}, respectively. The saturation polarizations of the material at T_{cold} and T_{hot} are denoted by $P_s(T_{cold})$ and $P_s(T_{hot})$, respectively, and expressed in C/m^2. Note that Kandilian *et al.* [53] erroneously called $P_s(T)$ the spontaneous polarization instead of saturation polarization as sometimes found in the literature [59]. The piezoelectric coefficient d_{33} is expressed in C/N, s_{33} is the elastic compliance (in m^2/N), and $x_3 = \alpha_3(T_{hot} - T_{cold})$ where α_3 is the linear thermal expansion coefficient (in K^{-1}). Note that this model was based on the assumption that the dielectric contribution to the primary pyroelectric coefficient was negligible compared with the dipole contribution (See Equation (8) in Ref. [53]). The model successfully predicted the energy density generated by PMN-32PT [53] and PZN-5.5PT [58]. Here also, the model predictions will be compared with the energy density experimentally measured with 8/65/35 PLZT.

4.2 Results and discussion

4.2.1 D-E loops
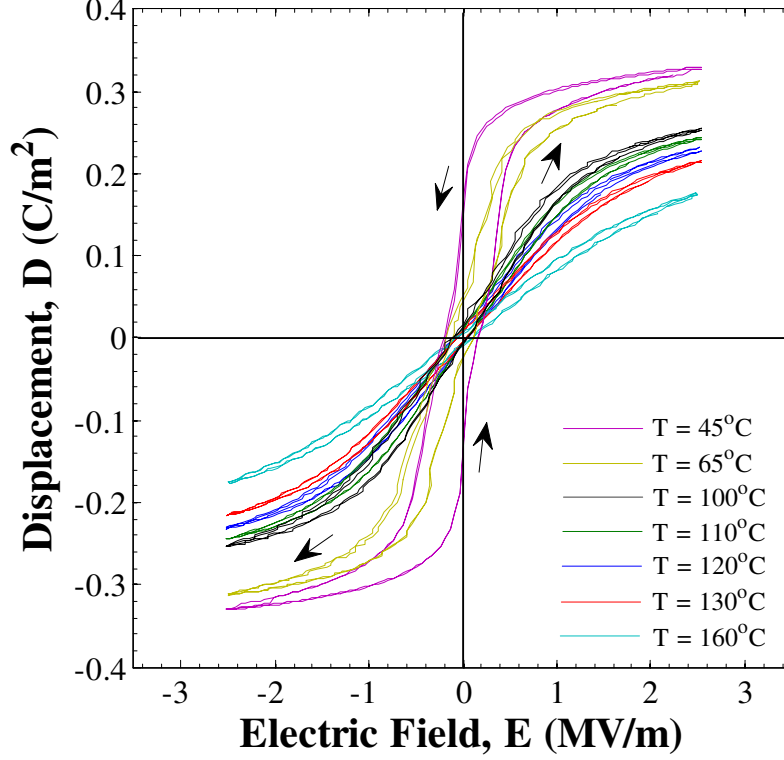
Figure 4.1: Bipolar isothermal electric displacement versus electric field (D-E) hysteresis curves at various temperatures. The D-E paths travel in a counter-clockwise direction. The electric field was cycled between -2.5 and +2.5 MV/m at 0.33 Hz. The D-E loops at 45 and 65°C correspond to the ferroelectric phase while those at 100, 110, 120, 130 and 160°C indicate that the material was in the ergodic relaxor phase.

Figure 4.1 plots the bipolar D-E loops at 45, 65, 100, 110, 120, 130, and 160°C measured at 0.33 Hz with Sample 4. The electric field was isothermally cycled between -2.5 MV/m and +2.5 MV/m. The isothermal D-E loops corresponding to 45 and 65°C featured square loops typical of a ferroelectric state. On the other hand, the D-E loops corresponding to 100, 110, 120, 130, and 160°C exhibited slim linear hysteresis with small remnant polarization ($P_r \leq 0.02$ C/m^2) indicating that the material was in the ergodic relaxor phase. Note that the

upper curve of unipolar D-E loops (not shown) were nearly identical to the bipolar D-E loops between 0 and 2.5 MV/m for the temperatures investigated in this study. Thus, analysis of the upper curves of unipolar or bipolar D-E loops resulted in nearly identical values of saturation and remnant polarizations $P_s(T)$ and $P_r(T)$ and relative permittivity $\varepsilon_r(T)$.

Moveover, the isothermal bipolar D-E loops corresponding to the ferroelectric phase plotted in Figure 4.1 show the non-linear behavior of the electric displacement D with respect to the electric field E. The electric displacement decreased sharply for a decreasing applied electric field around the critical electric field $E_{cr}(T)$. This non-linearity was also observed for [110]-oriented PZN-4.5PT by Zhu *et al.* [30] and was attributed to electric-field induced phase transitions. The sudden decrease in electric displacement D around $E_{cr}(T)$ could also be explained by the 180° polarization switching in which the polarization of each crystal's unit cell reversed direction from $+P$ to $-P$ when the polarization vector aligned with the applied electric field vector [71, 83, 110, 111]. Thus, the saturation polarization and relative permittivity varied non-linearly as a function of electric field and the dielectric properties required in Equation (4.1) were estimated from two piecewise regions of the isothermal bipolar D-E loops corresponding to the decreasing electric field branch. The electric displacement was assumed to depend linearly on the electric field in each region corresponding to electric field decreasing (i) from E_H to $E_{cr}(T)$ and (ii) from $E_{cr}(T)$ to E_L.

4.2.2 Effect of low electric field E_L

Figure 4.2 shows the average energy density generated by Sample 4 for five different Olsen cycles performed with low electric field E_L equal to 0, 0.1, 0.2, 0.3, and 0.4 MV/m. The high electric field was set as 1.5 MV/m while the cold and hot source temperatures were maintained at 65 and 160^oC, respectively. The error bars correspond to two standard deviations or 95% confidence interval. The energy density reached a maximum at $E_L = 0.2$ MV/m. In fact, the electric displacement vanished during Process 4-1 for E_L set as 0 MV/m since this relaxor ferroelectric material possessed small remnant polarization at either temperatures used [69]. In other words, the sample was unable to retain its polarization at zero electric
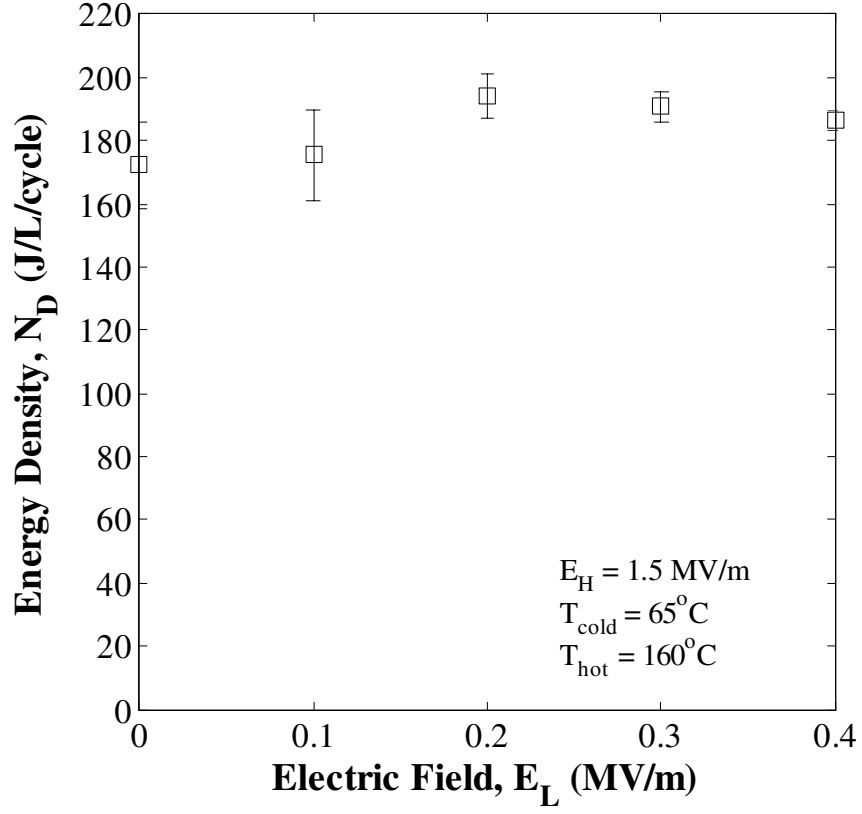
Figure 4.2: Energy density as a function of low electric field E_L varying from 0 to 0.4 MV/m. The high electric field was set as $E_H = 1.5$ MV/m while the cold and hot source temperatures were maintained at $T_{cold} = 65^oC$ and $T_{hot} = 160^oC$, respectively.

field. As a result, lowering the low electric field E_L from 0.2 to 0 MV/m resulted in a reduction in the energy density from 192 to 172 J/L/cycle. Meanwhile, raising the low electric field E_L from 0.2 to 0.4 MV/m reduced the energy density from 192 to 187 J/L/cycle, due to the reduced electric field span (E_H - E_L). Therefore, all measurements reported in the remainder of this study will correspond to E_L = 0.2 MV/m.

4.2.3 Sample variability

Figure 4.3 shows the energy density as a function of high electric field E_H between 0.4 and 1.5 MV/m collected from four different samples for temperatures T_{hot} equal to (a) 100°C, (b) 110°C, (c) 120°C, and (d) 130°C. The low electric field E_L was 0.2 MV/m while the cold source temperature T_{cold} was maintained at 65°C. The energy generated represent the averaged values over five cycles performed under quasiequilibrium. Here also, the error bars represent a 95% confidence interval. Figure 4.3 indicates that sample variation was larger for low values of temperature T_{hot} and electric field E_H. In fact, the largest sample variation was found for T_{hot} = 100°C and E_H = 0.4 MV/m, with a maximum relative difference among samples of 19.7%. Meanwhile, sample variability was the lowest for T_{hot} = 130°C and E_H = 1.5 MV/m, with a maximum relative difference among samples of 9.1%. These results establish the consistency and repeatability of experimental measurements not only from one cycle to the next but also from one sample to the next.

4.2.4 Effect of cold source temperature T_{cold}

Figures 4.4 and 4.5 show the average energy density generated by Sample 4 as a function of high electric field E_H ranging from 0.4 to 2.5 MV/m for cold source temperature T_{cold} equal to 65 and 45°C, respectively. Here also, the hot source temperature T_{hot} was equal to (a) 100°C, (b) 120°C, (c) 130°C, and (d) 160°C. The low electric field was set as E_L = 0.2 MV/m. Figures 4.4 and 4.5 establish that the energy density N_D increased as the cold source temperature T_{cold} decreased. For example, for the conditions E_H = 2.5 MV/m and T_{hot} = 160°C, the energy density increased from 343 to 442 J/L/cycle, or by 29%, when T_{cold} was
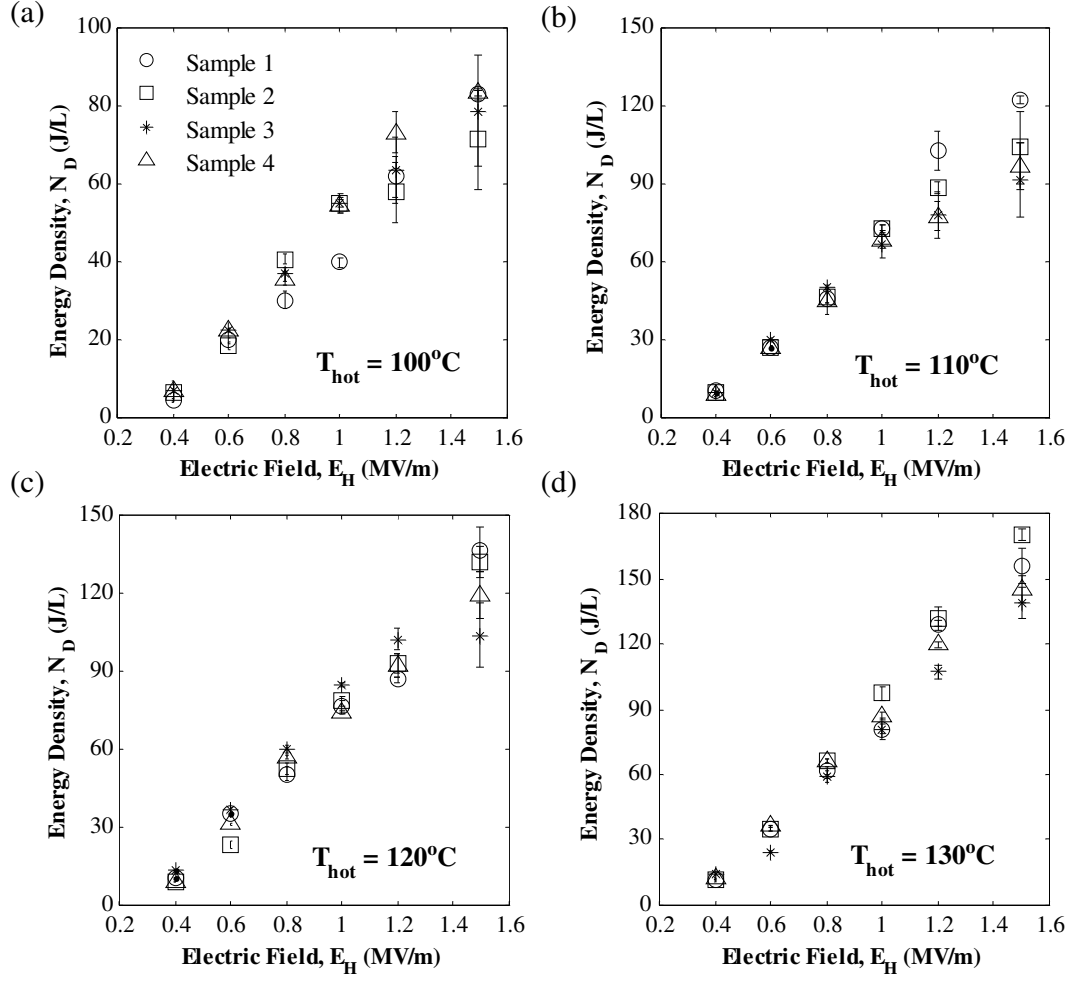
Figure 4.3: Experimentally measured energy density of 8/65/35 PLZT as a function of high electric field E_H for samples 1 to 4. The hot source temperature T_{hot} was equal to (a) 100°C, (b) 110°C, (c) 120°C, and (d) 130°C. The high electric field E_H ranged from 0.4 to 1.5 MV/m. The cold source temperature T_{cold} and low electric field E_L were set as 65°C and 0.2 MV/m, respectively. Sample variability was greatest at low temperatures and low electric fields.
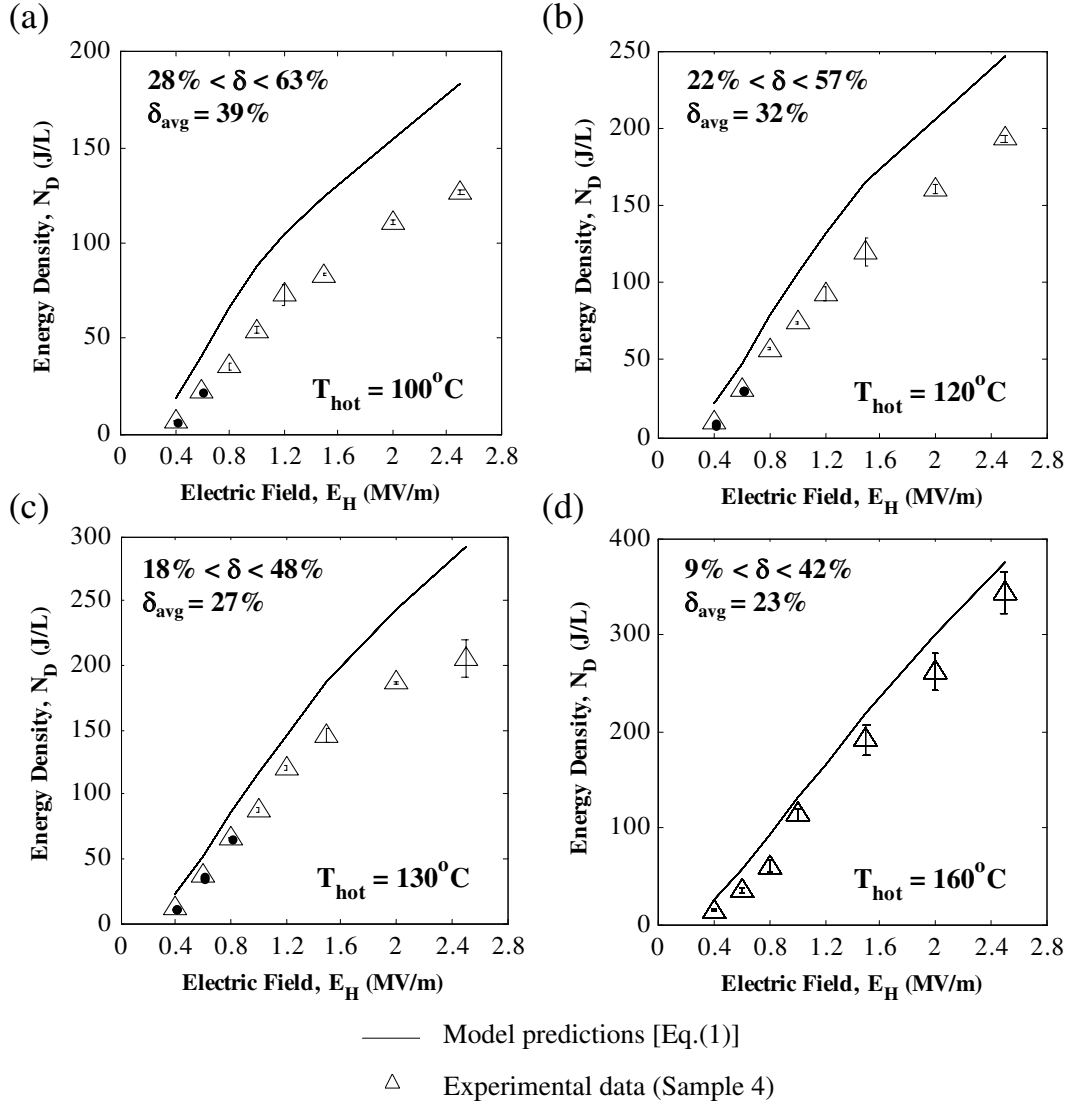
Figure 4.4: Experimentally measured energy density generated by 8/65/35 PLZT (Sample 4) as a function of high electric field. The hot source temperature T_{hot} was equal to (a) 100°C, (b) 120°C, (c) 130°C, and (d) 160°C. The high electric field E_H ranged from 0.4 to 2.5 MV/m. The cold source temperature T_{cold} and low electric field E_L were set as 65°C and 0.2 MV/m, respectively. The relative error between the model predictions and experimental data is denoted by δ.
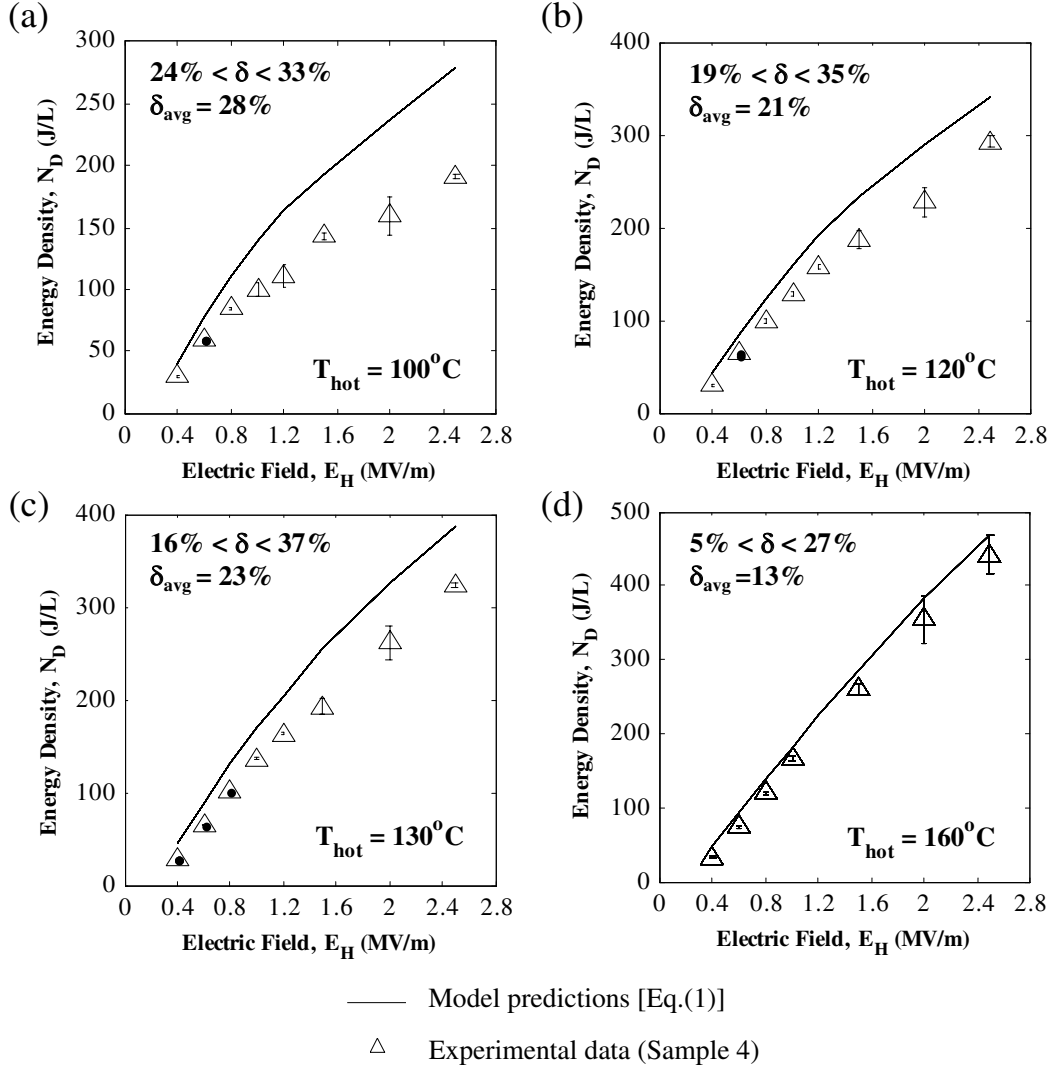
Figure 4.5: Experimentally measured energy density generated by 8/65/35 PLZT (Sample 4) as a function of high electric field. The hot source temperature T_{hot} was equal to (a) 100°C, (b) 120°C, (c) 130°C, and (d) 160°C. The high electric field E_H ranged from 0.4 to 2.5 MV/m. The cold source temperature T_{cold} and low electric field E_L were set as 45°C and 0.2 MV/m, respectively. The relative error between the model predictions and experimental data is denoted by δ.

reduced from 65 to 45°C. Indeed, this was attributed to the increase in electric displacement span $[D(E,T_{cold}) - D(E,T_{hot})]$. In other words, more free charges were collected at the electrode surface as T_{cold} was lowered. However, reducing T_{cold} from 65 to 45°C increased the cycle period from 51.9 to 124 s and in turn decreased the corresponding power density from 6.61 W/L to 3.56 W/L. This reduction in power density was attributed to an increase in the time required for isoelectric cooling (Process 4-1) and discharging (Process 2-3) to be performed under quasiequilibrium conditions. It is a consequence of the slow dielectric relaxation of PLZT in the ergodic relaxor phase [69]. The dipole reorientation contributing to the polarization change becomes slower at low temperatures due to the increased energy barrier required to activate and reorient the polar nanodomains [112,113].

4.2.5 Effect of hot source temperature T_{hot}

Figures 4.4 and 4.5 also establish that the energy density increased as the hot source temperature T_{hot} was raised from 100 to 160°C for a given high electric field E_H. Between T_{cold} and $T_{hot} \geq T_{Curie}$, the 8/65/35 PLZT samples underwent a phase transition from ferroelectric (polar) to ergodic relaxor (non-polar). In fact, the largest energy density was obtained at T_{hot} near the ferroelectric-ergodic relaxor phase transition temperatures $T_{Curie} \leq 160^o$C. However, increasing the operating temperature difference (T_{hot} - T_{cold}) in excess of 135°C resulted in large thermal stresses causing the sample to crack.

Effect of high electric field E_H

Figures 4.4 and 4.5 indicate that, for a given hot source temperature T_{hot}, the energy density N_D increased as the high electric field E_H increased. Indeed, raising E_H increased the electric field span (E_H - E_L) resulting in larger energy densities as suggested by Figure 2.4 and Equation (4.1). However, the high electric field E_H was physically limited by the sample's dielectric strength which was determined experimentally as 2.5 MV/m for samples with bare gold electrodes. We speculate that large strains were electrically-induced within the samples when they were subject to cyclic high magnitude electrical loading, causing microcracks to

60

develop along the domain boundaries [114]. In addition, electric field concentrations were formed such that the relative permittivity at the crack interior and the ceramic body were different thus producing a strain [115,116]. Ultimately, the propagation of these field-induced cracks led to sample failure [72]. Each sample used in this study cracked after ~ 200 to 300 Olsen cycles due to a combination of thermal stress and field-induced strains.

Two strategies were explored to increase the electrical breakdown field of 8/65/35 PLZT samples and maximize E_H. First, the specimen thickness was reduced from 650 μm (Sample 4) to 370 μm (Samples 5 and 6) and 290 μm (Sample 7), since the electrical breakdown strength of ceramics was reported to increase with decreasing sample thickness [114]. This can be explained by the presence of fewer defects typically contained in thinner samples. Furthermore, a silicone conformal coating was applied to the PLZT Samples 5 to 7 to reduce their susceptibility to cracking as suggested by Ref. [64]. Implementation of these strategies in Sample 5 resulted in an increase of the material electrical breakdown from 2.5 to 4.5 MV/m for the operating conditions $T_{cold} = 45^oC$, $T_{hot} = 160^oC$, and $E_L = 0.2$ MV/m. Then, the maximum energy density generated per cycle increased by more than 50% from 442 J/L (Sample 4) to 668 J/L (Sample 5).

4.2.6 Maximum energy density
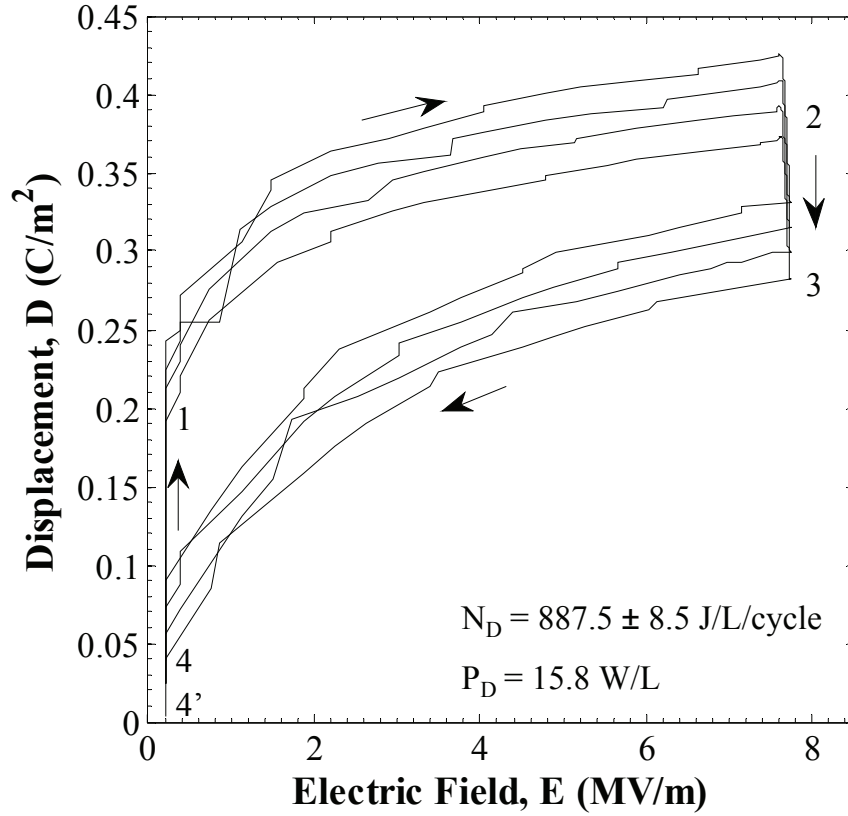
Figure 4.6: Electric displacement versus electric field diagram containing four experimental Olsen cycles (Sample 7). The electric field was cycled between 0.2 and 7.5 MV/m. The cold source temperature T_{cold} and hot source temperature T_{hot} were 25 and 160°C, respectively. The average energy density over four cycles was 887.5 J/L at 0.0178 Hz, corresponding to the largest energy generated by 8/65/35 PLZT in this study.

Figure 4.6 presents four consecutive Olsen cycles performed on Sample 7 at 0.0178 Hz, corresponding to the maximum energy density achieved experimentally with this material. The cold and hot source temperatures were 25 and 160°C while the electric field was cycled between $E_L = 0.2$ MV/m and $E_H = 7.5$ MV/m, respectively. An energy density of 887.5 ± 8.5 J/L/cycle was obtained, corresponding to a power density of 15.8 W/L.

Figure 4.6 shows that the D-E paths of the Olsen cycles were not closed since Points 4 and 4' did not coincide. The offset was caused by leakage current across the PLZT ceramic

at high temperatures and/or large electric fields [6, 25, 36, 99]. The loss in energy density associated with the leakage current was estimated to be 15-20%. Moreover, note that the Olsen cycles did not follow a smooth path between E_L and E_H during isothermal Processes 1-2 and 3-4 in the D-E diagram. It indicates that these processes were not performed under quasiequilibrium conditions [58]. This can be attributed to the inhomogeneity of the sample caused by the microcracks. Indeed, microcracks may have propagated along the grain boundaries of the sample while the Olsen cycle was performed under high electric fields and/or high temperatures [115]. These fractures introduced spatial variation in the local electric field near the crack front [116].

4.2.7 Discussion

The maximum energy density of 888 J/L/cycle produced by 8/65/35 PLZT should be compared with those achieved by other pyroelectric materials. In fact, Table 4.2 compares the maximum energy density generated from the Olsen cycle for different materials, temperature ranges, and operating electric fields. Note that a maximum energy density of 900 J/L/cycle using 60/40 P(VDF-TrFE) was reported by Olsen et $al.$ [5] for temperatures between 25^oC and 120^oC and electric field cycled between 20 and 60 MV/m. However, it is unclear whether these experimental results were averaged over multiple cycles and if they were repeatable. In fact, Navid et $al.$ [6] produced 204 J/L/cycle averaged over 5 cycles for the same material, temperature range, and operating electric fields. To the best of our knowledge, the maximum energy density reported in the present study for 8/65/35 PLZT is the largest energy density experimentally measured repeatably over multiple cycles.

4.2.8 Model predictions

As previously discussed, the electric displacement $D(E, T)$ of 8/65/35 PLZT varies nonlinearly when the electric field decreases from E_H to E_L. Therefore, the dielectric properties required in Equation (4.1) were retrieved for two piecewise regions of the isothermal bipolar D-E loops corresponding to isothermal field reduction (i) from E_H to $E_{cr}(T)$ and (ii) from

Table 4.2: Comparison of maximum energy density achieved using the Olsen cycle (or Ericsson cycle) for different materials, temperature ranges, and operating electric fields.

Material	T_{cold} ^oC	T_{hot} ^oC	E_L MV/m	E_H MV/m	$N_{D,max}$ J/L/cycle	Ref.
PZST	157	177	0.4	3.2	131	[22]
PZST	145	178	1.2	3.2	130	[19]
PZST	146	159	0.0	2.9	100	[23]
PZST	110	170	0.0	2.8	0.4	[21]
73/27 P(VDF-TrFE)	23	67	23.0	53.0	30	[36]
60/40 P(VDF-TrFE)	58	77	4.1	47.2	52	[4]
60/40 P(VDF-TrFE)	67	81	20.3	37.9	130	[7]
60/40 P(VDF-TrFE)	25	110	20.0	50.0	521	[6]
60/40 P(VDF-TrFE)	25	120	20.0	60.0	900	[5]
61.3/29.7/9 P(VDF-TrFE-CFE)	0	25	0.0	25.0	50	[117]
PZN-4.5PT	100	160	0.0	2.0	217	[29]
PZN-5.5PT	100	190	0.0	1.2	150	[58]
PMN-10PT	30	80	0.0	3.5	186	[44]
PMN-32PT	180	170	0.0	0.9	100	[53]
8/65/35 PLZT	25	160	0.2	7.5	888	Present study

$E_{cr}(T)$ to E_L. The critical electric field $E_{cr}(T)$ was estimated from the inflection point in the isothermal D-E loop. It was found to increase with increasing temperature. Table 4.3 summarizes the critical field $E_{cr}(T)$, saturation and remnant polarizations $P_s(T)$ and $P_r(T)$, and relative permittivity $\varepsilon_r(T)$ of Sample 4 for temperatures between 45 and 160°C. The energy density predicted by the piecewise model can be expressed as the sum of two components

$$N_D = N_D(E_L, E_{cr}, T_{cold}, T_{hot}) + N_D(E_{cr}, E_H, T_{cold}, T_{hot}) \tag{4.2}$$

where the function $N_D(E_{L/H}, E_{cr}, T_{cold}, T_{hot})$ is given by Equation (4.1). The contribution from the region of decreasing electric field from E_H to $E_{cr}(T)$ can be predicted by Equation (4.1) using the saturation polarization $P_s(T)$. The contribution from the region of decreasing electric field from $E_{cr}(T)$ to $E_L = 0.2$ MV/m can be predicted by Equation (4.1) using the remnant polarization $P_r(T)$ instead of $P_s(T)$.

Table 4.3: Critical electric field $E_{cr}(T)$, spontaneous polarization $P_s(T)$, remnant polarization $P_r(T)$, and relative permittivity $\epsilon_r(T)$ of 8/65/35 PLZT (Sample 4) retrieved for two piecewise regions of isothermal bipolar D-E loops in the temperature range between 45 and 160°C.

T (^{o}C)	45	65	100	110	120	130	160
$E_{cr}(T)$ (MV/m)	0.4	0.6	1.2	1.5	1.6	1.8	–
$E_H = 2.5$ MV/m to $E_{cr}(T)$							
$\epsilon_r(T)$	2624	3700	3977	3714	3700	3849	6439
$P_s(T)$ (C/m^2)	0.265	0.220	0.155	0.151	0.139	0.118	0.0145
$E_{cr}(T)$ to $E_L = 0.2$ MV/m							
$\epsilon_r(T)$	10850	26050	15040	12547	11243	9651	6439
$P_r(T)$ (C/m^2)	0.232	0.0856	0.0221	0.0188	0.0181	0.0148	0.0145

Figures 4.4 and 4.5 compare systematically the energy density obtained experimentally with predictions of Equation (4.2) for four hot source temperatures $T_{hot} = 100, 120, 130$, and 160°C and E_H ranging from 0.4 to 2.5 MV/m. The cold source temperature T_{cold} was set as

65°C (Figure 4.4) and 45°C (Figure 4.5). Note that the thermal expansion term $d_{33}x_3/s_{33}$ [54] corresponding to the secondary pyroelectric coefficient was ignored in the model predictions for PLZT. Indeed, Kandilian [53] observed that for PMN-32PT, the Olsen cycle extended beyond the electric displacement bounded by the isothermal D-E loops. This was attributed to the contribution of thermal expansion to the energy density [53]. However, in the case of 8/65/35 PLZT, the Olsen cycles fell within the bounds of the isothermal D-E loops at both T_{cold} and T_{hot}. Therefore, the thermal expansion did not contribute to the energy density generated. Similar observations were made for PZN-5.5PT [58].

Figures 4.4 and 4.5 also report the range and the average value of the relative error between experimental data and model predictions, denoted by δ and δ_{avg}, respectively. For example, the average relative error reached 39% and 28% for $T_{cold} = 65^o$C and $T_{cold} = 45^o$C at $T_{hot} = 100^o$C, respectively. For such low value of $T_{hot} = 100^o$C, a small absolute difference in energy density resulted in a large relative error. However, the model predicted the experimental data reasonably well, for $T_{cold} = 45^o$C and $T_{hot} \geq 100^o$C and for $T_{cold} = 65^o$C and $T_{hot} \geq 130^o$C. In these cases, the average relative error between model predictions and experimental data was less than 30%.

Figure 4.7 shows the isothermal bipolar D-E loops collected on Sample 4 at $T_{cold} = 45^o$C and T_{hot} equal to (a) 100°C, (b) 120°C, (c) 130°C, and (d) 160°C overlayed with the corresponding Olsen cycles measured for $E_L = 0.2$ MV/m and $E_H = 2.5$ MV/m. Figure 4.7 illustrates the discrepancies between model predictions and experimental data. In fact, the Olsen cycles did not span the electric displacement between the isothermal bipolar D-E loops corresponding to T_{cold} and T_{hot}. They also did not fully overlap with the isothermal bipolar D-E loops at T_{cold} when electric field increased from E_L to E_H (Process 1-2). We attribute the latter to a sudden increase in electric displacement associated with a field-induced phase transition [30] and/or possibly the existence of mixed phases [118] when the applied electric field increased from E_L to E_{cr} during the Olsen cycle. By contrast, this sharp increase in electric displacement was absent in the bipolar D-E loop at T_{cold}. The discrepancies between the paths followed by the isothermal D-E loops and the Olsen cycle may also be explained by the electrocaloric temperature change during process 1-2 and 3-4. The temperature of a
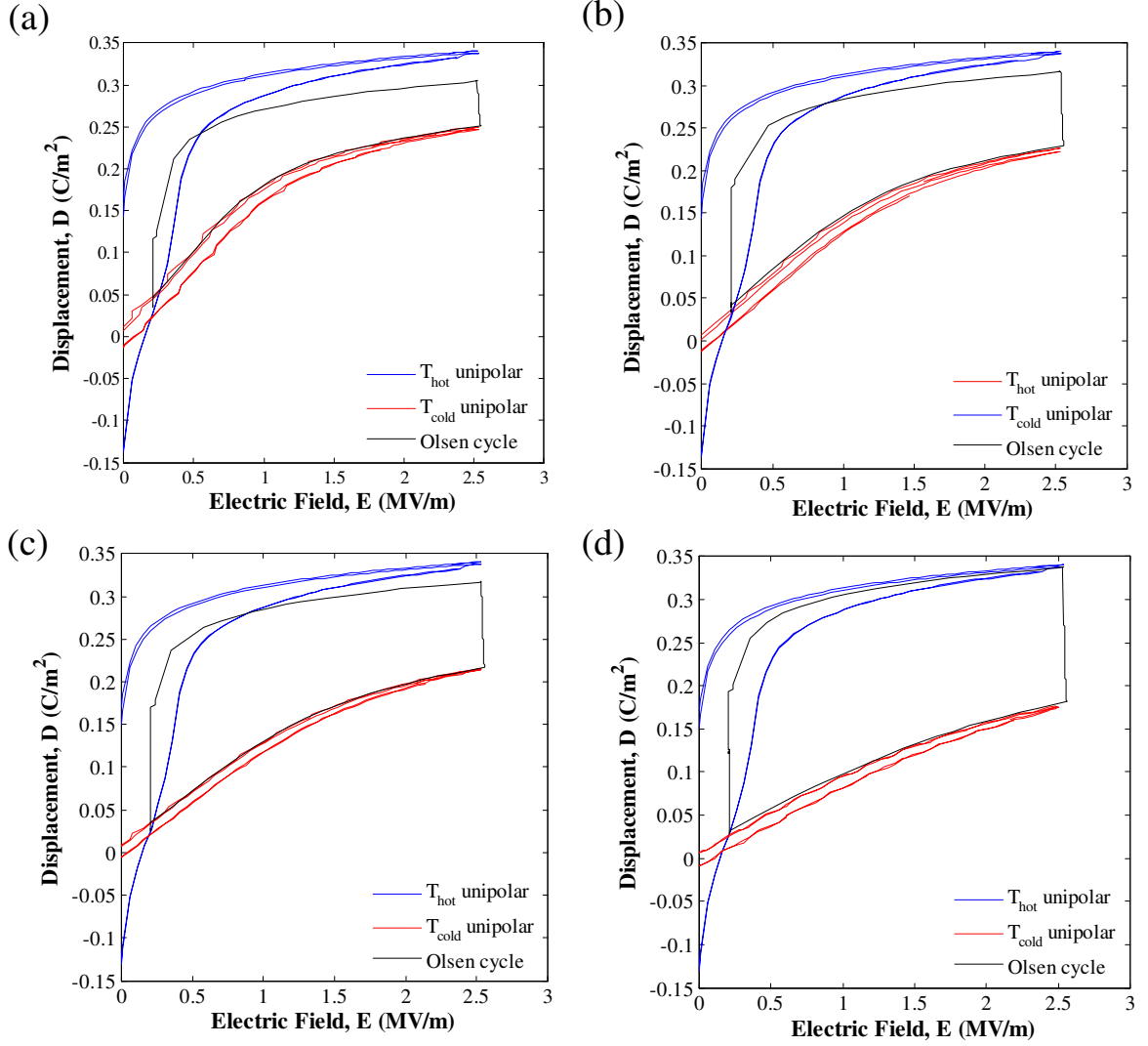
Figure 4.7: D-E diagram of isothermal bipolar D-E loops and experimental Olsen cycles for 8/65/35 PLZT (Sample 4). The temperature T_{hot} was equal to (a) 100°C, (b) 120°C, (c) 130°C, and (d) 160°C while $T_{cold} = 45$°C, $E_L = 0.2$ MV/m, and $E_H = 2.5$ MV/m. The Olsen cycle was vertically displaced to coincide with the D-E curve at T_{hot}.

pyroelectric material may increase or decrease when the electric field is raised or withdrawn (process 1-2 and 3-4). Indirect electrocaloric measurements for 8/65/35 PLZT [119] showed a small temperature change ΔT of 0.15, 0.52, 0.65, 0.68, and 0.64^{o}C at 45, 100, 120, 130, and 160°C, respectively, for electric field between 0 and 2.5 MV/m. However, the electrocaloric temperature change may be relevant in thin films capable of sustaining large electric field spans. In fact, a temperature change of 40K was observed in 0.45 μm thick 8/65/35 PLZT at 45°C for an electric field span $\Delta E = 125$ MV/m.

Overall, the model predictions were relatively good given the range of parameters explored, the simplicity of the model which did not account for leakage current, and the complexity of the physical phenomena taking place during the Olsen cycle.

4.3   Chapter summary

In this chapter, the energy densities generated by ferroelectric relaxor 8/65/35 PLZT undergoing the Olsen cycle were experimentally measured. A maximum energy density of 888 J/L/cycle corresponding to a power density of 15.8 W/L was obtained at 0.0178 Hz for operating temperatures between $T_{cold} = 25^o$C and $T_{hot} = 160^o$C and electric field cycled between $E_L = 0.2$ MV/m and $E_H = 7.5$ MV/m. The maximum electric field and temperature swing were limited by electrical breakdown and thermal stress, respectively. Sample variability was relatively small particularly at high temperatures and large electric fields. Moreover, increasing the operating temperature difference (T_{hot} - T_{cold}) increased the energy density generated but in turn reduced the power density produced due to an increase in the time required to perform isoelectric cooling and heating (Processes 4-1 and 2-3) under quasiequilibrium conditions. Furthermore, the electrical breakdown strength and thus the energy and power densities of 8/65/35 PLZT increased as the sample thickness decreased. Finally, the experimental results confirmed the validity of the physical model [53] developed to predict energy densities of ferroelectric relaxors subjected to the Olsen cycle.

CHAPTER 5

Direct Thermal to Electrical Energy Conversion using 9.5/65/35 PLZT Ceramics in the Ergodic Relaxor Phase

This chapter is concerned with experimental measurements on 9.5/65/35 PLZT ceramic samples subject to the Olsen cycle. The effects of various operating conditions were systematically investigated for different pyroelectric materials to explore their respective effects on the energy and power generation performance over a wide range of conditions.

5.1 Experiments

5.1.1 Samples

Hot isostatically pressed 9.5/65/35 PLZT ceramics with grain diameter around 5 μm were obtained from Aura Ceramics, Inc., New Hope, MN, USA. Six samples with 10 mm x 10 mm rectangular cross-sections were cut from bulk blocks using a diamond blade. The samples were then polished by applying figure-eight strokes on sandpaper to achieve thicknesses ranging from 190 to 500 μm. Rectangular gold (Au) or platinum (Pt) electrodes were sputtered onto opposite faces of the samples about 1-2 mm from the edges. The electrode area was chosen to be smaller than the overall sample area in order to reduce electrical conduction around the sample edges [86]. Electrical wires were bonded to the electrodes using silver epoxy. Silicone conformal coating was also applied to both faces of the samples and cured at 65°C for one hour to increase their dielectric strength [120]. Table 5.1 summarizes the thickness and cross-sectional area of the six 9.5/65/35 PLZT samples investigated in this

study.

Table 5.1: Thickness and cross-sectional area of six different 9.5/65/35 PLZT samples and their electrodes investigated in this study.

Sample #	Electrode Material	Thickness μm	Sample size mm x mm	Electrode size mm x mm
8	Au	250	10.07 x 9.75	9.51 x 8.55
9	Au	275	8.35 x 8.13	7.62 x 7.42
10	Au	500	7.57 x 6.94	5.28 x 4.70
11	Pt	250	7.43 x 7.02	6.35 x 6.28
12	Pt	250	7.43 x 7.02	6.19 x 6.50
13	Pt	190	7.43 x 7.02	6.10 x 7.34

5.1.2 Electrical and thermal subsystems

The electrical subsystem used to measure isothermal D-E loops and to perform the Olsen cycle consisted of a modified Sawyer-Tower bridge circuit. It was used to apply the required electric field across the pyroelectric element and to measure the charge Q across the electrode surfaces. Details of the circuit used in the present study were provided in Chapter 3.2 and in Refs. [6,53,86] and need not be repeated.

The thermal subsystem consisted of two beakers containing dielectric fluids Dow Corning 100 cSt silicone oil or Fluorinert FC-70 maintained at T_{cold} and T_{hot} by temperature-controlled hot plates [6,53,86]. Dow Corning oil was used for temperatures above room temperature. Fluorinert was used for temperatures near 0°C. Each beaker contained a magnetic stirrer to ensure uniform temperature. For temperatures below room temperature, the cold beaker was placed in an ice bath. Oil temperatures were monitored using K-type thermocouples.

5.1.3 Experimental procedure

5.1.3.1 Isothermal D-E loops

Isothermal bipolar D-E loops were measured by immersing the samples in silicone oil baths maintained at temperatures $T_{cold} = 23^oC$ and $T_{hot} = 140^oC$. The D-E loops were collected by applying a continuous triangular voltage signal across the sample at 0.1 Hz. This frequency corresponded to that of the isothermal electric field changes occurring in processes 1-2 and 3-4 of the Olsen cycle. D-E loops were measured with increasing electric field span. The applied electric field E_H was increased in 1.0 MV/m increments from 3.0 MV/m to 6.0 MV/m and then in 0.25 MV/m increments as E_H approached 6.75 MV/m.

5.1.3.2 Olsen cycle

The Olsen cycle was performed on all samples under various electric fields, temperatures, and frequencies to investigate their respective effects on the energy and power generated. The energy density N_D generated by the Olsen cycle and given by Equation (2.9) was numerically estimated using the trapezoidal rule. The power density was computed according to Equation (2.10). Preliminary tests (not shown) indicated that the energy density N_D reached a maximum for low electric field $E_L = 0.2$ MV/m. Therefore, all measurements reported in the remainder of this study corresponds to $E_L = 0.2$ MV/m. On the other hand, the high electric field E_H was varied from 2.0 to 6.75 MV/m. Similarly, the cold source temperature T_{cold} was either 3 or 23^oC and the hot source temperature T_{hot} was equal to 140^oC. As discussed earlier, decreasing T_{cold} should result in a larger energy density. Between T_{cold} and $T_{hot} \geq T_{Curie}$, the 9.5/65/35 PLZT samples underwent a phase transition from ferroelectric to ergodic relaxor accompanied by a significant decrease in electric displacement D. Therefore, large energy densities could be achieved near the ferroelectric-relaxor phase transition temperature T_{Curie} reported to be below 0^oC [121]. However, the temperature T_{cold} was physically limited to 3^oC. Between $T_{cold} = 3^oC$ and $T_{hot} = 140^oC$, the 9.5/65/35 PLZT samples featured a significant difference in electric displacement D but only in the presence of an electric field.

Finally, the overall cycle frequency was defined as $f = (\tau_{12} + \tau_{23} + \tau_{34} + \tau_{41})^{-1}$ where τ_{ij} corresponds to the duration of process i-j. It was varied between 0.025 and 0.16 Hz by changing the duration of the isoelectric field heating process 2-3 and cooling process 4-1 denoted by τ_{23} and τ_{41}, respectively. For example, the times τ_{23} and τ_{41} varied between $\sim$ 1 and $\sim$ 10 s. However, the durations of the isothermal processes 1-2 (τ_{12}) and 3-4 (τ_{34}) were kept constant at $\sim$ 1.5 s. Quasiequilibrium conditions were achieved when the electric displacement reached steady state, i.e., $(\partial D/\partial T) = 0$, during processes 2-3 and 4-1 before the electric field was varied in processes 3-4 and 1-2, respectively. Operating the Olsen cycle under quasiequilibrium conditions resulted in the maximum energy density [58]. On the other hand, to maximize the power density, the Olsen cycle was performed athigher frequencies by reducing the duration of isoelectric field processes 2-3 and 4-1.

5.2   Results and discussion

5.2.1   Isothermal D-E Loops and Olsen cycle

Figure 5.1 presents typical isothermal bipolar D-E loops measured with Sample 11 at T_{cold} = 23°C and T_{hot} = 140°C between 0.2 and 4.0 MV/m at 0.1 Hz. The sample exhibited the slim-loop relaxor behavior at 140°C typically observed in x/65/35 PLZT ceramics with x = 9 to 10% [75]. Note that the bipolar D-E loops were similar among samples for any given temperature. Upon a decrease in temperature below T_{Curie}, the remnant polarization of relaxor ferroelectric materials typically increases from around zero in the relaxor state to finite values in the ferroelectric state. The Curie temperature was reported to be below 0°C for 9.5/65/35 PLZT [121]. Unfortunately, these temperatures were prohibitively low to impose in the experimental setup used. Figure 4.1 shows that 9.5/65/35 PLZT did not exhibit remnant polarization at 3 or 140°C, indicating that the material remained in the ergodic relaxor state at these temperatures. However, the material became polarized under an applied electric field and then an absolute difference in electric displacement was observed.

Moreover, Figure 5.1 also depicts an experimental Olsen cycle performed under quasi-
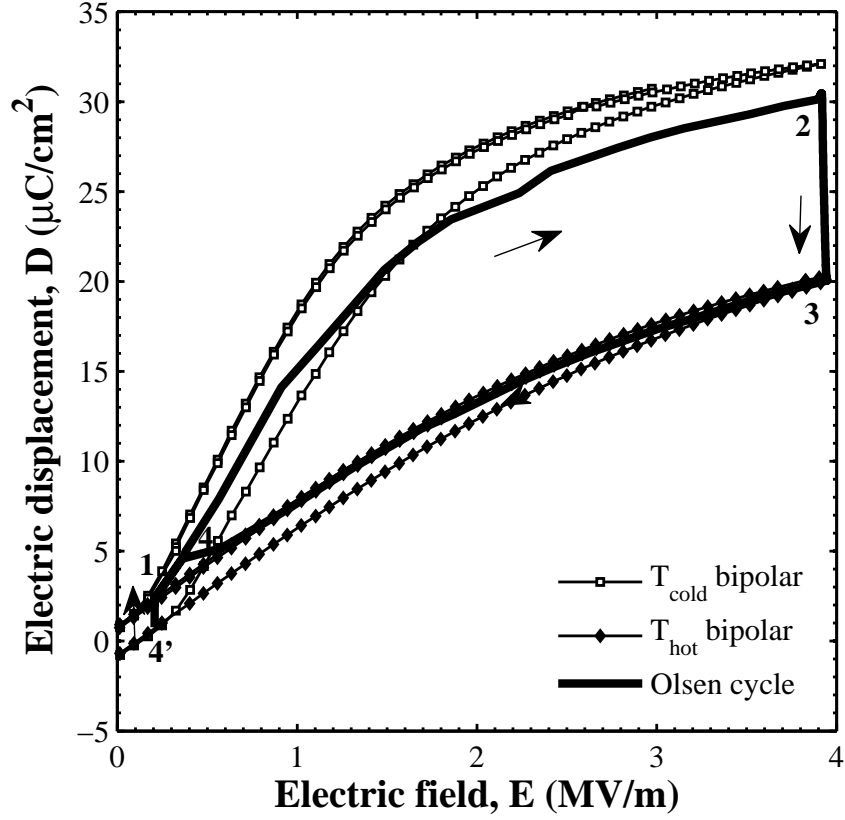
Figure 5.1: D-E diagram of isothermal bipolar D-E loops and Olsen cycle performed under quasiequilibrium conditions for a 250 μm thick 9.5/65/35 PLZT sample (Sample 11). The temperatures T_{cold} and T_{hot} were equal to 23 and 140°C, respectively, while the electric field was cycled between $E_L = 0.2$ MV/m and $E_H = 4.0$ MV/m. The Olsen cycle was vertically displaced to coincide with the isothermal D-E curve at T_{hot}.

equilibrium conditions at $f = 0.038$ Hz, for the same sample, at temperatures between T_{cold} = 23°C and T_{hot} = 140°C and electric fields cycled between E_L = 0.2 MV/m and E_H = 4.0 MV/m. Process 3-4 follows the decreasing electric field path of the isothermal D-E loop at T_{hot}. However, process 1-2 did not follow the increasing electric field path of the isothermal D-E loop at T_{cold}. The fact that the Olsen cycle did not span the electric displacement between the isothermal bipolar D-E loop corresponding to T_{cold} may be attributed to the existence of mixed ferroelectric and ergodic relaxor phases [118,122] when the applied electric field increased from E_L to $E_{cr}(T)$ during the Olsen cycle. These phases co-exist likely due to slow stabilization of the ferroelectric phase from the relaxor phase caused by parasitic interactions between defects and polar nanoregions [122].

Furthermore, notice that points 4 and 4' of the Olsen cycle do not coincide. The offset was attributed to leakage current across the PLZT ceramic often observed at high temperatures and/or large electric fields [6, 25, 36, 99]. Additionally, the change in electric displacement was negligibly small in the isoelectric cooling process 4'-1 for T_{cold} = 3°C and T_{hot} = 140°C indicating that this process in the Olsen cycle can be performed on 9.5/65/35 PLZT nearly instantaneously. This was made possible by operating at temperatures corresponding to the relaxor phase with small remnant polarization. Indeed, for 8/65/35 PLZT, this was a long process of the Olsen cycle [86] caused by slow dipole-dipole relaxation [69].

5.2.2 Effect of high electric field E_H

Figure 5.2 shows (a) the energy density and (b) the power density generated by Samples 8 to 11 under quasi-equilibrium conditions for cycle frequencies between 0.029 and 0.057 Hz. The high electric field E_H ranged from 2.0 to 6.75 MV/m while the low electric field E_L was maintained at 0.2 MV/m. The cold and hot source temperatures were 23 and 140°C, respectively. Each data point corresponds to the average over five Olsen cycles while the error bar corresponds to two standard deviations or 95% confidence interval. Figure 5.2 indicates that the largest sample variation in energy density was found for E_H = 3.0 MV/m with a maximum relative difference among samples of 23%. Meanwhile, sample variability
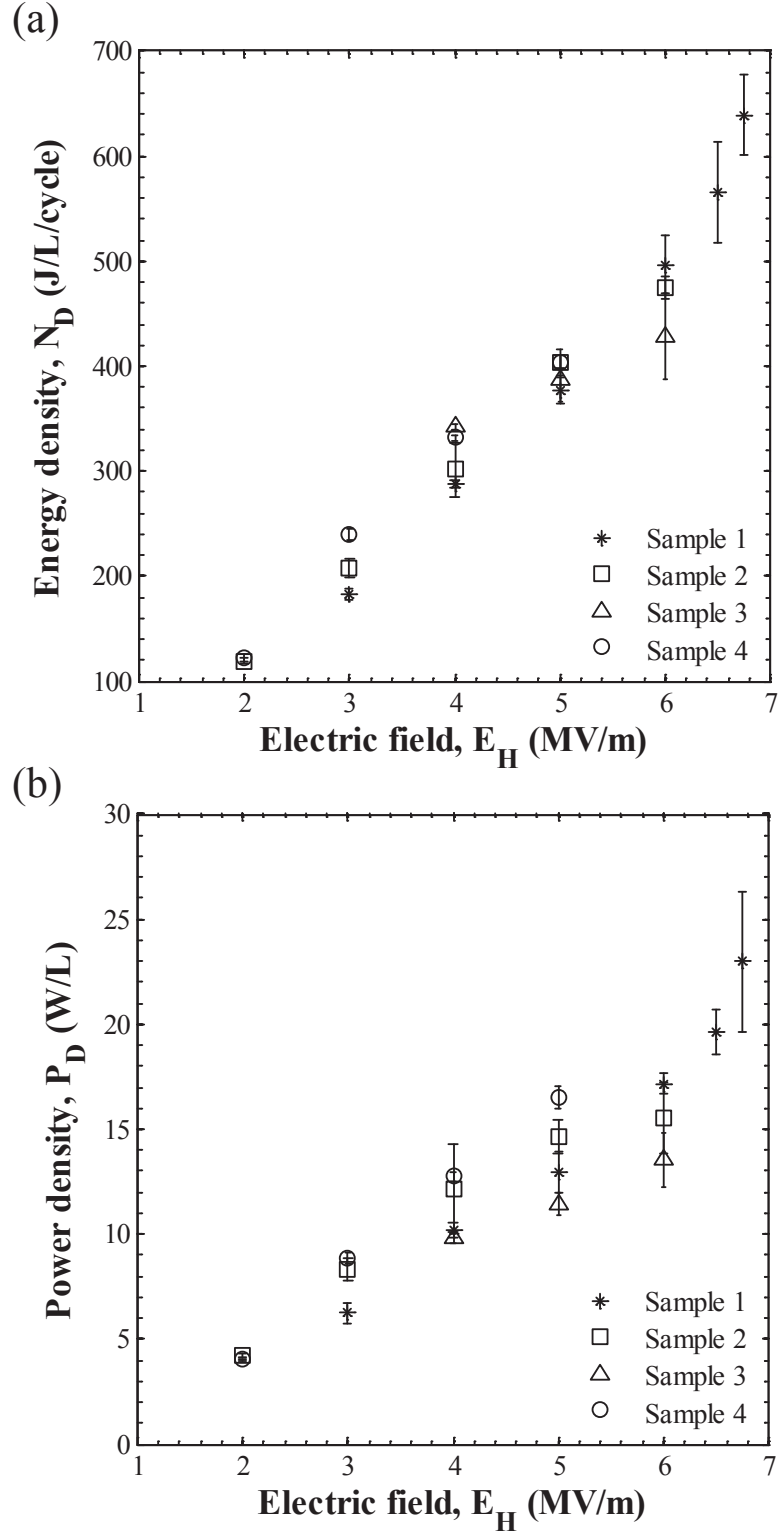
Figure 5.2: (a) Energy density and (b) power density generated by 9.5/65/35 PLZT (Samples 8 to 11) as a function of high electric field E_H between 2.0 and 6.75 MV/m under quasiequilibrium conditions. The low electric field E_L was set as 0.2 MV/m, while the cold and hot source temperatures were equal to $T_{cold} = 23^oC$ and $T_{hot} = 140^oC$, respectively.

was the lowest for $E_H = 5.0$ MV/m, with a maximum relative difference among samples of 6%. These results establish the consistency and repeatability of experimental measurements not only from one cycle to another but also from one sample to another.

Figure 5.2a also indicates that raising the electric field span (E_H - E_L) resulted in larger energy densities. For example, the energy density generated by a 250 μm thick sample increased by 38.4% from 240 to 332 J/L/cycle when the high electric field E_H increased from 3.0 to 4.0 MV/m. However, the maximum value of E_H was limited by the samples' dielectric breakdown. For example, beyond an electric field threshold, cracks formed within the sample. The formation of cracks may be attributed to mechanical stresses in the material along the grain boundaries due to spatially varying electric fields causing preferential domain wall motion [123]. Microcracks may then propagate along the grain boundaries of the samples under the cyclic electric field loading. This phenomenon was previously observed in 9.4/65/35 PLZT for applied electric fields around 0.3 MV/m [115]. Additionally, the crack lengths of Vicker's indentation test under zero field have been shown to increase with increasing temperature [115]. Thus, the combination of cycling high temperature and high electric field caused the samples to fracture.

5.2.3   Effect of sample thickness b

The dielectric breakdown strength of ceramics was reported to increase with decreasing sample thickness [114]. Consequently, the effect of sample thickness on the energy and power densities was investigated with Samples 8 to 10 whose thickness was 250, 275 and 500 μm, respectively. Figure 5.2 shows that a reduction in sample thickness enabled larger electric fields to be applied across the sample without causing electrical breakdown. In fact, samples with thickness 500 μm (Sample 10) and 250 μm (Sample 11) had electric field breakdown of 6.0 and 6.75 MV/m, respectively. This resulted in a maximum energy density of 427.8 and 636.9 J/L/cycle, corresponding to a power density of 13.6 and 22.7 W/L, respectively. The increase in breakdown field can be explained by the presence of fewer domains in thinner samples. Therefore, thinner films had fewer grain boundaries and lower occurrences of crack

formation. This, in turn, enabled larger energy and power densities to be achieved.

Furthermore, using PLZT thin films offers advantages including (i) a substantial reduction in the applied voltage delivered to the electrical circuit during the Olsen cycle, (ii) faster thermal response, and (iii) smaller size and less weight for easier integration into devices. For example, as the specimen thickness was reduced from 500 μm (Sample 10) to 250 μm (Sample 8), the power density was found to increase by 26% from 13.56 to 17.15 W/L for high electric field $E_H = 6.0$ MV/m. This may be explained by a reduction in the thermal time constant associated with thinner films and the increase in cycle frequency f from 0.030 to 0.035 Hz. In addition, only 6 V applied across a 10 μm thin PLZT film would be required to achieve an electric field of 6.0 MV/m instead of 1,140 V required across a 190 μm thick sample (Sample 13).

5.2.4 Effect of electrode material

Large mechanical stresses may be induced at the interface of two distinct materials subjected to large temperature variations if their thermal expansion coefficients feature large mismatch. Thus, the electrode material may affect the performance of pyroelectric materials. To investigate this effect, Pt or Au electrodes of identical thickness were deposited on 9.5/65/35 PLZT samples. The thermal expansion coefficient in the thickness direction of 9.5/65/35 PLZT, platinum, and gold were reported to be equal to 5.4 μm/m/^{o}C [75], 8.8 μm/m/^{o}C [124], and 14.2 μm/m/^{o}C [124] respectively. Figure 5.2b indicates that 9.5/65/35 PLZT samples of the same thickness with gold (Sample 8) or platinum (Sample 11) electrodes had similar power density for all frequencies. However, the samples with Pt electrodes (Samples 11-13) were capable of sustaining larger temperature swings (T_{hot} - T_{cold}) than the samples with Au electrodes (Samples 8-10). These results establish that it is important to utilize the electrode material which has the closest thermal expansion coefficient to that of the selected pyroelectric material. This may reduce the susceptibility of a pyroelectric material to thermomechanical breakdown upon repeated cycling with large temperature differences.

5.2.5   Effect of cold source temperature T_{cold}

As previously discussed, increasing the difference between T_{cold} and T_{hot} should result in larger energy density. Figure 5.3 shows (a) the energy density and (b) the power density generated by Samples 11 and 12 as a function of high electric field E_H and frequencies between 0.033 and 0.057 Hz corresponding to quasiequilibrium. The low electric field was set as $E_L = 0.2$ MV/m. The cold source temperature T_{cold} was maintained at 23°C (for Sample 11) or 3°C (for Sample 12). The hot source temperature was fixed at 140°C. Figure 5.3 establishes that for a given high electric field E_H, both the energy and power densities increased by an average of 44.6 J/L/cycle (16.7%) and 6.6 W/L (67%), respectively, as the cold source temperature T_{cold} was reduced from 23 to 3°C. Note that Sample 11 broke before we could perform tests for E_H larger than 5.0 MV/m. The increase in energy density was attributed to the increase in electric displacement span ΔD as T_{cold} was lowered. In other words, more free charges were collected at the electrode surface as T_{cold} decreased from 23 to 3°C.

Moreover, Lee *et al.* [86] observed that as T_{cold} was lowered, the energy density generated by 8/65/35 PLZT increased but the power density decreased. This was explained by the significant increase in time required for isoelectric field cooling process 4-1 to operate under quasiequilibrium conditions. By contrast, this process was short in 9.5/35/65 PLZT samples operating in the relaxor phase above T_{Curie}. A reduction in cold source temperature from 23 to 3°C had no significant effect on the quasiequilibrium cycle period. As a result, the power density of 9.5/65/35 PLZT increased as the cold source temperature T_{cold} was reduced from 23 to 3°C. Note that a reduction of T_{cold} from 3 to -50°C would increase the remnant polarization of 9.5/65/35 PLZT from around 0.01 to 0.11 C/m^2 [121]. This could result in larger energy density. However, the duration of process 4-1 would no longer be instantaneous. In fact, this process is typically rate-limiting for relaxor ferroelectric materials. Therefore, we speculate that decreasing T_{cold} from 3 to -50°C will result in lower power density.

(a)

(b)
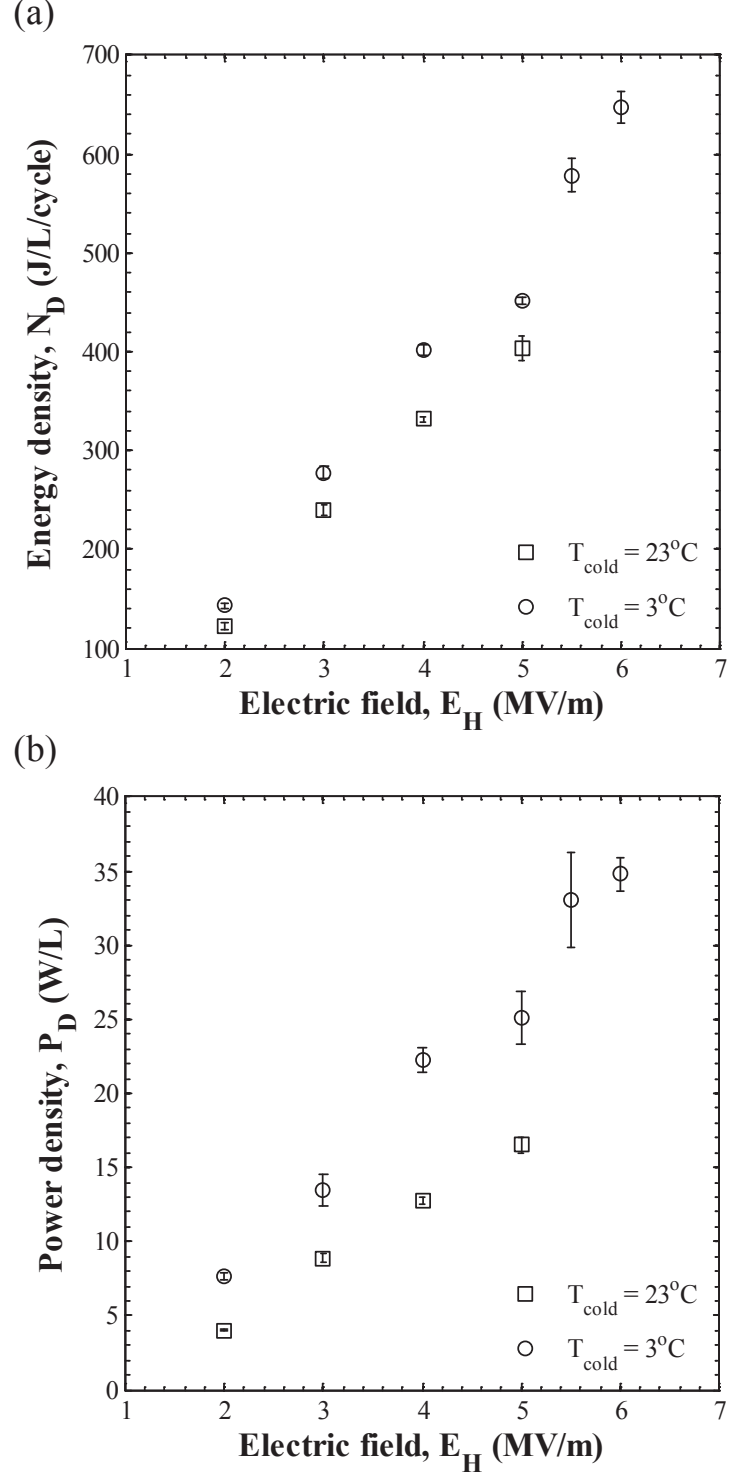
Figure 5.3: (a) Energy density and (b) power density generated by 9.5/65/35 PLZT for $T_{cold} = 23^oC$ (Sample 11) or 3^oC (Sample 10) as a function of high electric field E_H under quasiequilibrium conditions. The low electric field E_L was set as 0.2 MV/m and the hot source temperature was equal to $T_{hot} = 140^oC$.
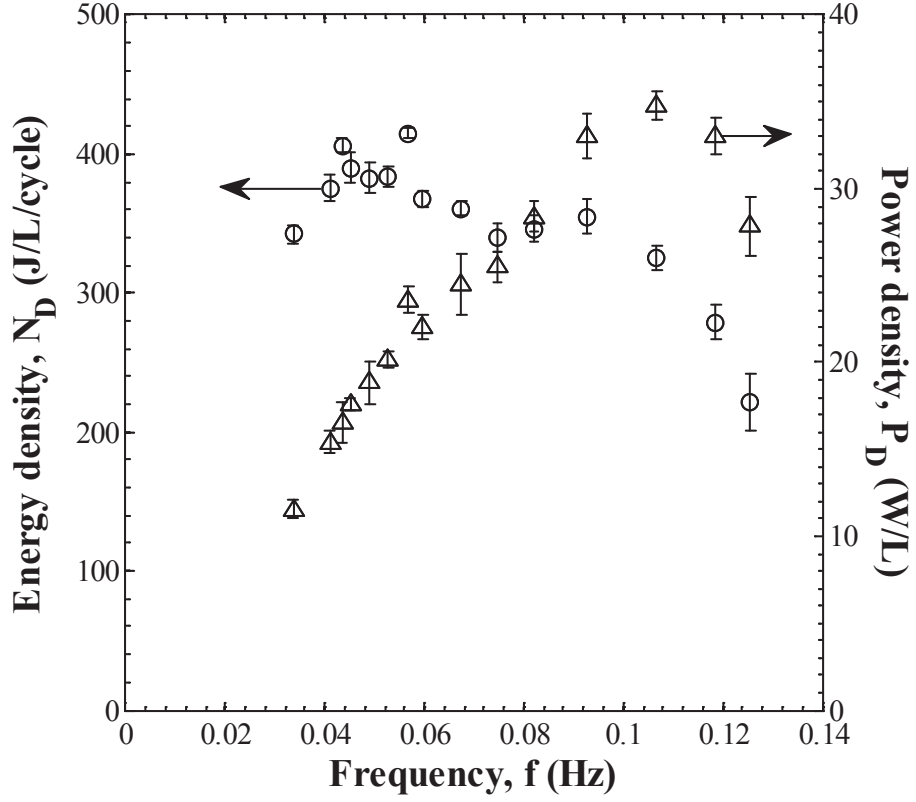
Figure 5.4: Energy and power densities generated by 9.5/65/35 PLZT (Sample 11) as a function cycle frequency. The cold and hot source temperatures were T_{cold} = 23°C and T_{hot} = 140°C, respectively. The low electric field E_L was set as 0.2 MV/m and the high electric field E_H was fixed at 5.0 MV/m.

5.2.6 Effect of cycle frequency f

Figure 5.4 plots both the energy and the power densities obtained with Sample 11 as a function of cycle frequency for $E_L = 0.2$ MV/m and $E_H = 5.0$ MV/m. The cold and hot temperatures were $T_{cold} = 23^oC$ and $T_{hot} = 140^oC$, respectively. The durations of the isothermal processes 1-2 (τ_{12}) and 3-4 (τ_{34}) were set at $\simeq 1.5$ s. Meanwhile, the duration of isoelectric field processes 2-3 (τ_{23}) and 4-1 (τ_{41}) were the same and ranged from about 1 to 10 s. The four different processes in the Olsen cycle performed at frequencies below 0.057 Hz corresponded to quasiequilibrium conditions.

Figure 5.4 shows that, under the above conditions, the energy density reached a maximum of 441 J/L/cycle at frequencies below 0.057 Hz and then decreased with increasing cycle frequency. Unfortunately, for frequencies below 0.057 Hz, the energy density decreased due to excessive leakage current. At such low frequencies, the duration of isoelectric field process 2-3 was longer than the time required for the electric displacement to reach steady state and this provided an opportunity for charges at the surface of the PE to conduct through its body. Indeed, leakage current increases with increasing time at which the PE operates at high electric fields. On the other hand, as the cycle frequency increased beyond 0.057 Hz, the energy density decreased due to a reduction in electric displacement span ΔD as the processes were not performed under quasiequilibrium conditions.

Additionally, Figure 5.4 indicates that under the above conditions, the power density P_D reached a maximum of 34.7 W/L at 0.11 Hz. Performing the Olsen cycle at frequencies greater than 0.11 Hz led to a smaller power output. This was due to the fact that the dipole realignment and phase transitions occurring during the isoelectric field processes 2-3 and 4-1 may not have time to be complete at larger frequencies. Moreover, although the energy density was smaller at 0.11 Hz than at 0.057 Hz, the smaller cycle time resulted in a larger power density. Overall, the maximum power density can be achieved by considering the expression $P_D = N_D(f)f$. It is a compromise between a small cycle time (large f) and large electric displacement span ΔD with minimal leakage current (large N_D).

Figure 5.5 plots the power density generated by Sample 12 as a function of cycle frequency

81
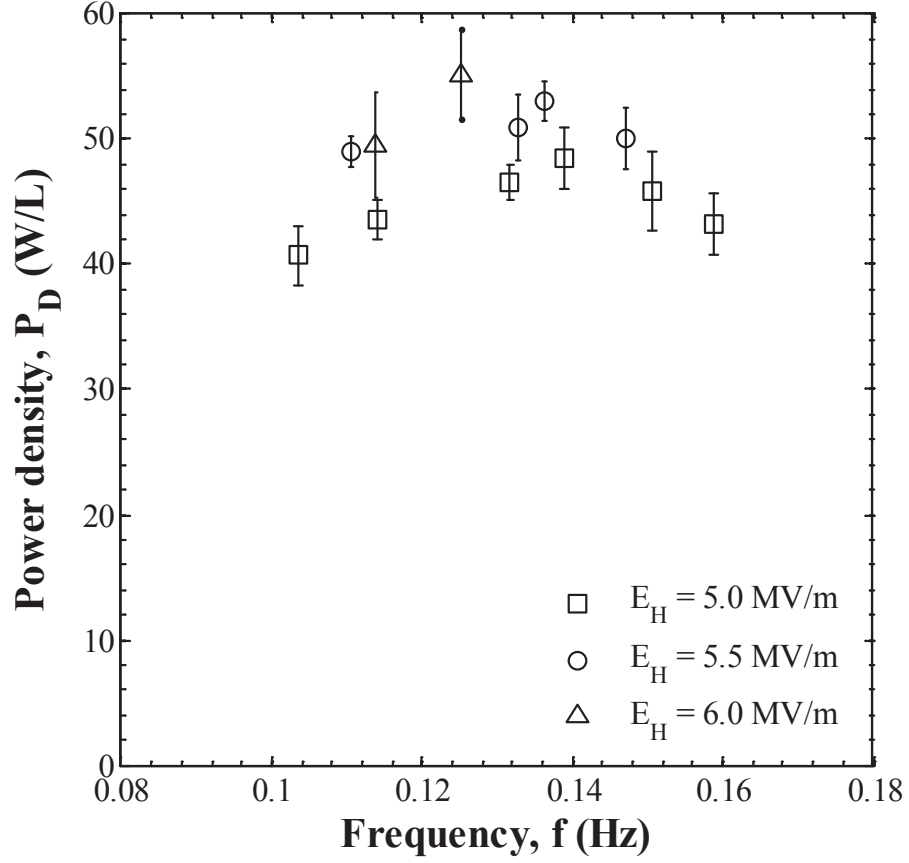
Figure 5.5: Power density generated by 9.5/65/35 PLZT (Sample 12) as a function of cycle frequency. The cold and hot source temperatures were $T_{cold} = 3^oC$ and $T_{hot} = 140^oC$, respectively. The low electric field E_L was set as 0.2 MV/m. The high electric field E_H was equal to either 5.0, 5.5, or 6.0 MV/m.

between 0.10 and 0.16 Hz. The low electric field E_L was set as 0.2 MV/m while the high electric field E_H was set as either 5.0 MV/m, 5.5 MV/m, or 6.0 MV/m. The cold and hot source temperatures were equal to $T_{cold} = 3^oC$ and $T_{hot} = 140^oC$, respectively. Preliminary tests (not shown) demonstrated that the change in electric displacement was negligibly small during process 4-1. Therefore, the duration of process 4-1 (τ_{41}) was set to be short at $\simeq 1$ s. Durations of processes 1-2 (τ_{12}) and 3-4 (τ_{34}) were kept identical and constant at $\simeq 1.5$ s. However, the duration of process 2-3 (τ_{23}) was varied from ~ 1 to 4 s. Figure 5.5 indicates that the peak power density increased with increasing high electric field E_H. The increase in electric field E_H in combination with the increase in rate of electric field change led to an increase in the enclosed 1-2-3-4 area (N_D) as shown in Figure 2.4 without requiring a decrease in the cycle frequency f. In addition, the decrease in the duration of process 4-1 (τ_{41}) from ~ 1 - 10 s to ~ 1 s resulted in an increase in the peak power frequency from 0.11 to 0.14 Hz.

Zhu *et al.* [30] studied the effect of time rate of change of the electric field on the energy density generated by [110]-poled PZN-4.5PT by performing the Olsen (or Ericsson) cycle. The authors reported that the energy density can be increased by decreasing the duration of process 1-2 and by increasing the duration of process 3-4 in the Olsen cycle. Moreover, a uniform increase in the time rate of change of electric field for both processes 1-2 and 3-4 resulted in a non-linear decrease in energy density [30]. However, the energy density remained nearly constant for rates of electric field change between 0.08 and 8.0 MV/m/s [30]. Consequently, it was assumed that the power densities presented in Figure 5.5 were not influenced by variations in the time rate of change in electric field from $E_L = 0.2$ MV/m to $E_H = 5.0$, 5.5, or 6.0 MV/m corresponding to similar time rates of 3.20, 3.53, and 3.87 MV/m/s, respectively.

5.2.7 Maximum power density

Figure 5.5 also shows that a maximum power density of 55.26 ± 7.99 W/L was obtained with Sample 12 at 0.125 Hz, corresponding to an energy density of 441.0 ± 29.4 J/L/cycle. The
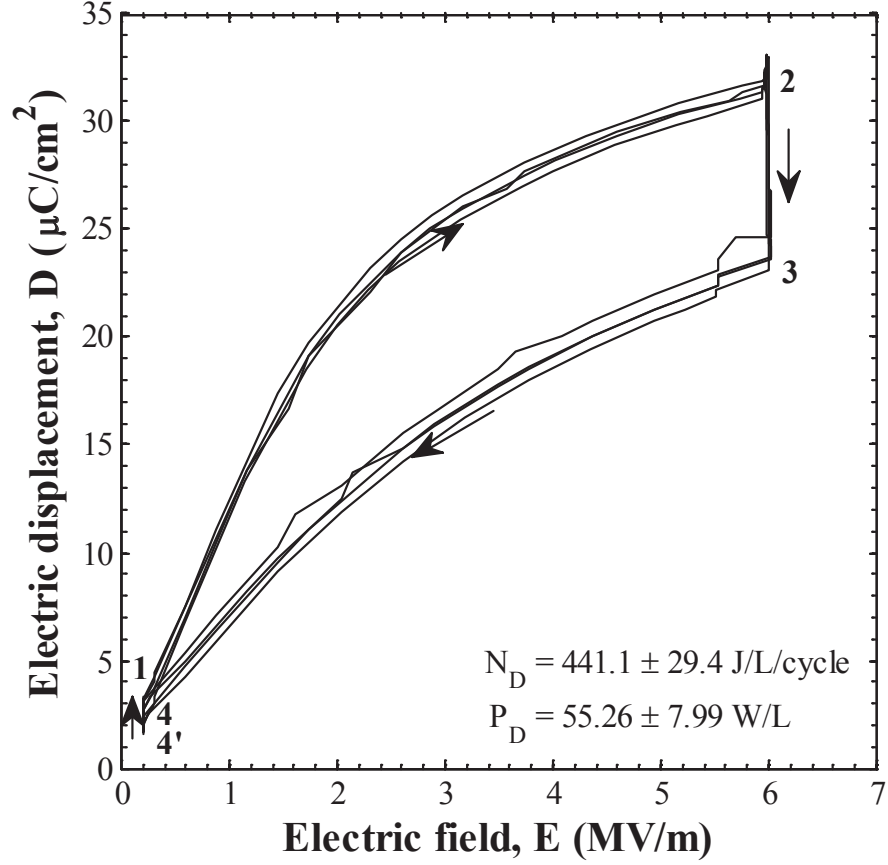
Figure 5.6: Electric displacement versus electric field diagram containing four experimental Olsen cycles (Sample 12). The electric field was cycled between 0.2 and 6.0 MV/m. The cold source temperature T_{cold} and hot source temperature T_{hot} were equal to 3°C and 140°C, respectively. The average power density over four cycles was 55.26 W/L at 0.125 Hz, corresponding to the largest power density generated by 9.5/65/35 PLZT in this study.

cold and hot source temperatures were $T_{cold} = 3^oC$ and $T_{hot} = 140^oC$, respectively, while the electric field was cycled between $E_L = 0.2$ MV/m and $E_H = 6.0$ MV/m. Figure 5.6 presents four consecutive Olsen cycles on the D-E diagram corresponding to this maximum power density. The Olsen cycles did not follow a smooth path between E_L and E_H during processes 1-2 and 3-4 in the D-E diagram indicating that the processes were not performed under quasiequilibrium conditions. Figure 5.6 also shows that the D-E paths of the Olsen cycles were not closed since Points 4 and 4' did not coincide. This indicates that leakage current was observed across the PLZT ceramic at high temperatures and/or large electric fields [6, 25, 36, 99].

The maximum power density of 55.3 W/L generated by 9.5/65/35 PLZT is an improvement over the 33.9 W/L produced by PZST ceramic [22], 24.3 W/L obtained by [110] PZN-4.5PT single crystal [29], 15.8 W/L achieved by 8/65/35 PLZT ceramic [86], 11.7 W/L generated by [001] PZN-5.5PT single crystal [58], and 4.92 W/L produced by [001] PMN-32PT single crystal. The reader is referred to Table 5.2 for the experimental conditions (T_{cold}, T_{hot}, E_L, E_H, f) used in these various studies. In addition, the power density produced by 9.5/65/35 PLZT is comparable to the 58 W/L generated by 60/40 P(VDF-TrFE) polymer for a similar temperature range [6]. However, using 9.5/65/35 PLZT offers advantages over 60/40 P(VDF-TrFE) in that it (i) possesses low leakage current, (ii) does not require electrical poling prior to performing the Olsen cycle, and (iii) requires smaller electric field E_H and applied voltages in the Olsen cycle (Table 5.2).

5.2.8 Sample durability

Pyroelectric materials for energy harvesting applications are meant to be integrated into devices where the Olsen cycle is expected to be performed for a very large number of cycles. However, large mechanical stresses are thermally and electrically induced within the samples under repeated thermal and electrical loading [125]. The excessive stresses may initiate the development of microcracks along the domain boundaries. These cracks lead to the gradual degradation of the material performance.

Table 5.2: Summary of maximum power density obtained using the Olsen cycle (or Ericsson cycle) for different materials, temperature ranges, operating electric fields, and frequencies.

Material	T_{cold} °C	T_{hot} °C	E_L MV/m	E_H MV/m	f Hz	$P_{D,max}$ W/L	Ref.
PZST	156.8	177.4	0.4	2.8	0.26	33.9	[22]
73/27 P(VDF-TrFE)	23.0	67.0	23.0	53.0	0.079	2.38	[36]
60/40 P(VDF-TrFE)	25.0	120.0	20.0	50.0	0.125	112.5	[5]
60/40 P(VDF-TrFE)	58.3	76.5	4.0	48.0	0.256	13.3	[4]
60/40 P(VDF-TrFE)	67.3	81.4	20.2	37.9	0.12	10.7	[7]
60/40 P(VDF-TrFE)	25.0	120.0	20.0	50.0	0.13	58.0	[6]
PZN-4.5PT	100.0	160.0	0.0	1.0	0.10	24.3	[29]
PZN-5.5PT	100.0	190.0	0.0	1.5	0.10	11.7	[58]
PMN-32PT	80.0	170.0	0.2	0.9	0.049	4.92	[53]
8/65/35 PLZT	25.0	160.0	0.2	7.5	0.0178	15.8	[86]
9.5/65/35 PLZT	3.0	140.0	0.2	6.0	0.125	55.3	Present study
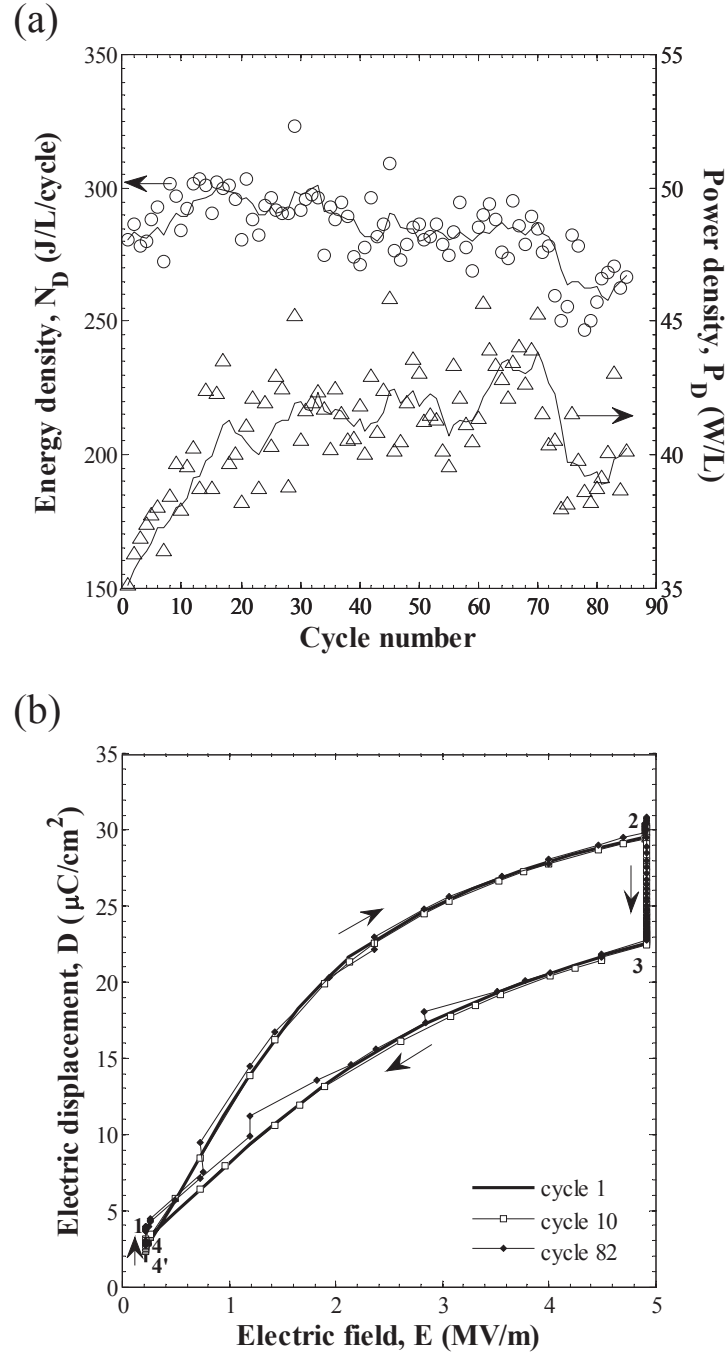
Figure 5.7: (a) Energy and power densities generated by 9.5/65/35 PLZT (Sample 13) as a function of cycle number. Solid lines (—) represent the 5 point moving average. The cold and hot source temperature was $T_{cold} = 23^oC$ and $T_{hot} = 140^oC$, respectively. The low and high electric field were set as $E_L = 0.2$ MV/m and $E_H = 5.0$ MV/m, respectively. The average cycle frequency was 0.144 ± 0.008 Hz. Cracks began to develop within the sample after about 72 successive cycles. (b) D-E diagram of the 1st, 10th, and 82nd Olsen cycle collected using Sample 13.

Therefore, a preliminary fatigue test was performed on Sample 13 to assess its durability. Sample 13 was subjected to around 85 successive Olsen cycles with operating temperatures between 23 and 140°C and electric field cycled between 0.2 and 5.0 MV/m. Figure 5.7a plots the energy and power densities generated by Sample 13 as a function of cycle number. Five-point moving averages are also plotted to guide the eye. A decrease in the energy and power densities was observed at around cycle 72, possibly marking the onset of stress-induced sample cracking. Figure 5.7b compares the 1st, 10th, and 82nd Olsen cycle on a D-E diagram. Between cycle 1 and cycle 82, the electric displacement span featured similar behavior at high electric fields. However, it is apparent that the electric displacement span decreased at low electric fields. This behavior is consistent with the fact that crack volume is directly correlated with polarization loss [126]. The latter can be explained by the concentration of defects present in microcracks limiting domain wall mobility [127]. Thus, the number of dipoles that can switch orientation under electric field cycling is reduced, corresponding to a decrease in polarization [127]. The degradation of performance with cycle number suggests that strategies to improve the electromechanical breakdown strength of PLZT ceramics should be explored and implemented in future studies to enhance the material and device reliability.

5.3   Chapter summary

This chapter was concerned with experimental measurements of the energy and power densities generated by subjecting electrostrictive 9.5/65/35 PLZT to the Olsen cycle. A maximum energy density of 637 $\pm$ 20 J/L/cycle was generated under quasiequilibrium conditions with a 250 μm thick sample and operating temperatures $T_{cold} = 3^o$C and $T_{hot} = 140^o$C while the electric field was cycled from $E_L = 0.2$ to $E_H = 6.0$ MV/m. A maximum power density of 55 $\pm$ 8 W/L was obtained at 0.125 Hz for the same specimen thickness, operating temperatures, and imposed electric fields. To the best of our knowledge, this power density is the largest achieved among pyroelectric single crystals and ceramics using the Olsen cycle. The dielectric strength and therefore the energy and power densities of the material increased

when the sample thickness decreased from 500 to 250 μm. Moreover, the electrode material was found to have no significant effect on the energy and power densities when the samples were subject to the same operating temperatures and electric fields. However, samples with electrode material possessing thermal expansion coefficients similar to that of PLZT were capable of withstanding larger temperature swings. The maximum applied electric field and temperature swings of the material were physically limited by the samples' dielectric breakdown and thermoelectromechanical stress leading to cracks, respectively. In addition, a fatigue test showed that the power generation gradually degraded while the sample was subject to repeated thermoelectrical loading. Additional investigation should focus on identifying pyroelectric materials featuring high electromechanical breakdown strength and large electric displacement span as presented in Chapter 6 for $x/65/35$ PLZT.

CHAPTER 6

Pyroelectric Energy Conversion using PLZT and Ferroelectric-Ergodic Relaxor Phase Transition

This chapter presents experimental measurements of the energy and power densities generated by samples with various compositions in the relaxor ferroelectric $x/65/35$ PLZT system subject to the Olsen cycle. PLZT thin films with various compositions were synthesized by the mixed oxide method and their temperature-dependent dielectric behavior was characterized.

6.1 Experiments

6.1.1 Material synthesis

Twelve $x/65/35$ PLZT ceramic samples with circular cross-sections were fabricated by the mixed oxide method [128]. They consisted of two samples for each lanthanum doping level $x = 5, 6, 7, 8, 9,$ and 10 mol.%. Figure 6.1 shows a block diagram summarizing the material synthesis procedure. The starting precursors included high purity ($\geq$ 99.9 mol.%) lead carbonate $PbCO_3$ (Hammond Lead Products Inc., Hammond, IN, USA), zirconium dioxide ZrO_2 (Magnesium Elektron Inc., Flemington, NJ, USA), lanthanum oxide La_2O_3 (Inframat Advanced Materials LLC, Manchester, CT, USA), and titanium dioxide TiO_2 (Ishihara Sangyo Kaisha Ltd., Japan). Each constituent was weighed in stoichiometric proportions with respect to the nominal composition of $Pb_{1-x}La_x(Zr_{0.65}Ti_{0.35})_{1-x/4}O_3$ ($x/65/35$ PLZT). The batch weights were adjusted to compensate for the weight loss on ignition (LOI) measured by heating each precursor material individually to 300°C at 10°C/min in an alumina

crucible and then cooling it down to room temperature. Deionized water, 1 wt.% ammonium hydroxide NH_4OH solution, and 5 wt.% Darvan dispersant (R.T. Vanderbilt Company Inc., Norwalk, CT, USA) were also mixed with the powder oxides. The suspension was ball milled using zirconia grinding media for 16 hours in order to increase powder homogeneity. Immediately thereafter, the slurry was poured through a strainer into a Pyrex dish and rinsed with deionized water. Then, the products were dried in an oven at 150°C in air for 2 hours. The resulting lumps of powder were crushed using an agate mortar and pestle. The milling, drying, and crushing processes were repeated once before the powders were deposited into an alumina crucible and calcined at 900°C for 6 hours.

Following this process, a 3 wt.% Paraloid B-67 binder (Rohm and Haas Company, Philadelphia, PA, USA) was added to the powder using acetone as the solvent. Then, the binderized powder was passed through a 100-mesh sieve to filter aggregated powders which contribute to a low packing efficiency. Fine powders were uniaxially cold-pressed into a 1.27 cm diameter pressing die (Across International LLC, Berkeley Heights, NJ, USA) at 17-21 MPa. In order to burn out the binder, the specimens were heated in a chamber furnace (Carbolite Ltd., Hope Valley, UK) in two stages. First, the specimens were ramp heated from 25 to 300°C at a rate of $\sim$2.3^{o}C/min and then held at 300°C for 2 hours. Then, the samples were heated from 300°C to 550°C at $\sim$4.1^{o}C/min and held at 550°C for 1 hour. Then, the discs were slowly cooled to room temperature. Once this process was completed, the specimens were sintered at 1300°C by heating them from 25°C to 1300°C at $\sim$10°C/min. Then, the temperature was held at 1300°C for 2 hours in a Pb rich atmosphere provided by excess $PbCO_3$ and ZrO_2 powders ($\sim$2.5 g) to compensate for the volatile evaporative loss of lead oxide above 800°C [129]. The excess lead ensures that the PLZT samples achieve full density by permitting a liquid phase to form in its grain boundaries during densification [129]. During the sintering process, pellets were fired onto a platinum foil to prevent diffusion of PLZT into its alumina substrate. The $PbCO_3$ and ZrO_2 powders were placed in an alumina combustion boat next to the pellets, all enclosed in an inverted alumina crucible. Finally, the specimens were cooled to room temperature to form dense PLZT ceramics.

Each x/65/35 PLZT sample was mechanically cut or sanded to achieve thicknesses rang-

(a) Powder preparation

Weigh PbO, La_2O_3, ZrO_2, and TiO_2 raw powders in stoichiometric proportions with respect to nominal $x/65/35$ PLZT composition

Adjust batch weights to compensate for loss of ignition (LOI)

Add 1 wt.% ammonium hydroxide, 5 wt.% dispersant, deionized water

Ball-mill suspension for 16 hours

Dry products in air at 150°C for 2 hours

Crush lump of powder with mortar and pestle

Repeat once

Calcinate powder at 900°C for 6 hours

Rinse powder with acetone and 3 wt.% binder

Pass fine powder through a mesh sieve

PLZT powders

(b) Sintering

Cold-press PLZT powder in pressing die at 17-21 MPa to form discs

Binder burnout

Heat from 25 to 300°C at 2°C/min
Hold at 300°C for 2 hours
Heat from 300 to 550°C at 4°C/min
Hold at 300°C for 1 hour
Cool discs to room temperature

Sinter discs in Pb-rich atmosphere at 1300°C for 2 hours

Cool sintered discs to room temperature

Dense PLZT samples

(c) Electrode deposition

Sputter Au electrodes on both faces

Bond wires to electrodes using silver epoxy

PLZT samples with Au electrodes

Figure 6.1: Procedure used to synthesize $x/65/35$ PLZT samples using the mixed oxide method. The processes include (a) powder preparation, (b) sintering, and (c) electrode deposition. The starting precursors were high purity raw powders and the final products were dense $x/65/35$ PLZT samples with Au electrodes.

ing from 180 to 200 μm. Circular gold (Au) electrodes were sputtered onto opposite faces of the polished samples about 2 mm from the edges by using a mask. The electrode area was chosen to be smaller than the overall sample area in order to reduce electrical conduction around the sample edges [86]. Electrical wires were bonded to the electrodes using silver epoxy. Silicone conformal coating was also applied to both faces of the samples and cured at 65°C for one hour to increase the samples' dielectric strength [120]. Table 6.1 summarizes the thickness and electrode cross-sectional area of each x/65/35 PLZT sample investigated in this study.

Table 6.1: Sample thickness and electrode cross-sectional area of the different x/65/35 PLZT samples investigated in this study.

Sample	Material	Thickness b (μm)	Electrode area A (mm^2)
14	5/65/35 PLZT	200	36.4
15	5/65/35 PLZT	180	33.2
16	6/65/35 PLZT	180	24.6
17	6/65/35 PLZT	200	32.7
18	7/65/35 PLZT	190	32.1
19	7/65/35 PLZT	210	32.8
20	8/65/35 PLZT	290	17.8
21	8/65/35 PLZT	180	36.7
22	9/65/35 PLZT	200	34.6
23	9/65/35 PLZT	210	33.4
24	10/65/35 PLZT	180	32.8
25	10/65/35 PLZT	190	33.2

6.1.2 Electrical and thermal subsystems

The electrical subsystem used to measure isothermal D-E loops and to perform the Olsen cycle consisted of a modified Sawyer-Tower bridge circuit. The loads consisted of a resistor in parallel and capacitor in series with the pyroelectric sample, denoted by R_2 and C_1 respectively in Fig.2 of Ref. [53]. It was used to apply the required electric field across the pyroelectric element and to measure the charge Q across the electrode surfaces. Details of the circuit used in the present study were provided in previous studies [6, 53, 86] and need not be repeated.

The thermal subsystem consisted of two beakers containing diphenyl-dimethylsiloxane dielectric fluid (Clearco DPDM-400) maintained at T_{cold} and T_{hot} [6, 53, 86]. This dielectric fluid is stable at temperatures up to 260^oC and possesses a large electrical resistivity ($\geq 10^{14}$ $\Omega\cdot$cm) for preventing high voltage arcing to the sample [130]. Each beaker contained a magnetic stirrer to ensure uniform dielectric oil bath temperatures. The latter were monitored using K-type thermocouples and maintained at their desired value by using temperature-controlled hot plates. The samples were alternatively immersed in hot and cold baths to create time-dependent temperature oscillations required in the Olsen cycle.

The thermal time constant of PLZT samples can be estimated as $\tau_t = \rho c_p/hb$ [101] where h is the convective heat transfer coefficient, b is the sample thickness, while ρ and c_p are the sample density and specific heat, respectively. For example, the thermal time constant for a 200 μm thick PLZT sample was estimated to be 1.73 s assuming $\rho = 7900$ kg/m^3 [107], $c_p = 329$ J/kg.K [108], and $h = 300$ W/m$^2\cdot$K corresponding to convective quenching in an oil bath [109]. This time constant indicates that the sample reached thermal equilibrium rapidly after it was transferred from one oil bath to the other during processes 2-3 and 4-1 of the Olsen cycle.

6.1.3 Experimental procedure

Two independent sets of measurements were performed on each $x/65/35$ PLZT composition studied to identify the conditions and values of (a) the maximum energy density (Samples 14,

16, 18, 20, 22) and (b) the maximum power density (Samples 15, 17, 19, 21, 23). Figure 6.2 illustrates the systematic procedure used to perform these measurements. First, isothermal dielectric hysteresis loops were measured and analyzed. Then, the effects of low and high electric fields E_L and E_H on the energy and power densities were successively assessed for each sample.

6.1.3.1 Isothermal D-E loops

Isothermal bipolar D-E loops were systematically collected for each sample by using the electrical circuit previously discussed. The D-E loops were measured to analyze the material's temperature-dependent dielectric behavior and to select the operating temperatures of the Olsen cycle accordingly. For $x/65/35$ PLZT with x ranging from 5 to 9 mol.%, the measurements were taken upon heating in 10-40°C intervals while the samples were immersed in a dielectric fluid bath maintained at constant temperature ranging from 3 to 250°C. For 10/65/35 PLZT, the measurements were performed in (i) an insulated dewar with samples exposed to liquid oxygen maintained at temperatures between -110 and 0°C and (ii) an isothermal oil bath kept at temperatures between 0 and 40°C. All bipolar D-E loop measurements were carried out by imposing a continuous triangular voltage signal across the sample at 0.1 Hz. This frequency corresponded to that of the isothermal electric field changes during processes 1-2 and 3-4 of the Olsen cycle. The amplitude of the applied voltage corresponded to an electric field cycled between -3.0 and +3.0 MV/m.

6.1.3.2 Olsen cycle

The Olsen cycle was performed on all $x/65/35$ PLZT samples under various electric fields, temperatures, and frequencies to investigate their respective effects on the energy and power densities. The energy density N_D generated by the Olsen cycle and given by Equation (2.9) was numerically estimated using the trapezoidal rule. Similarly, the power density was computed according to Equation (2.10). The overall cycle frequency was defined as $f = (\tau_{12} + \tau_{23} + \tau_{34} + \tau_{41})^{-1}$ where τ_{ij} corresponds to the duration of process i-j in the Olsen cycle.
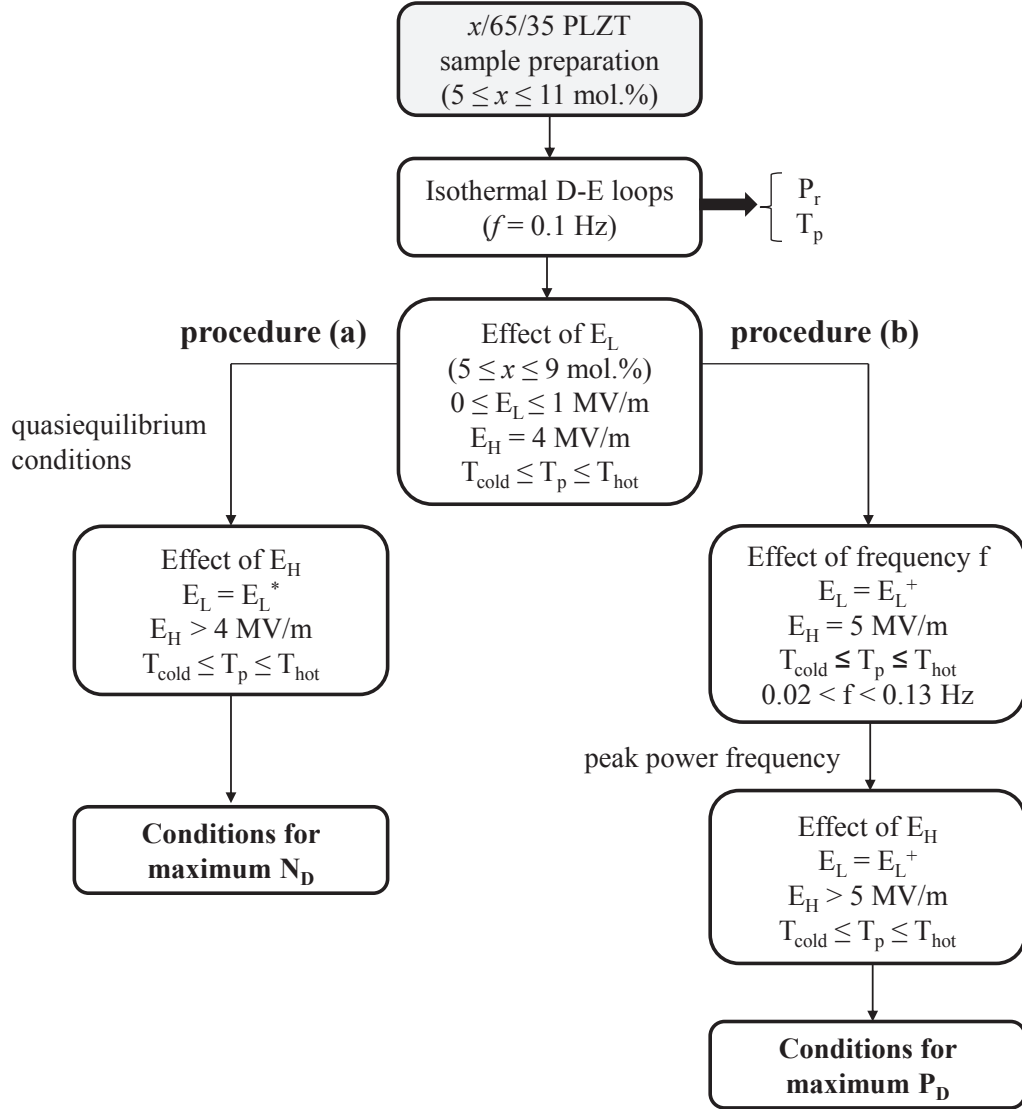
Figure 6.2: Systematic procedure used to identify the maximum (a) energy density N_D (Samples 14, 16, 18, 20, 22) and (b) power density P_D (Samples 15, 17, 19, 21, 23) of each PLZT composition investigated.

For most materials and applications, the maximum energy density and maximum power density are typically not achieved at the same operating frequency. The maximum energy density can be obtained by operating the Olsen cycle under quasiequilibrium conditions at relatively low frequencies [58]. In practice, quasiequilibrium conditions were achieved when the electric displacement reached steady state, i.e., $(\partial D/\partial T) = 0$, during processes 2-3 and 4-1 before the electric field was varied in processes 3-4 and 1-2, respectively. On the other hand, the maximum power density was typically reached at higher frequency. Therefore, the cycle frequency was varied to examine its effect on power density by changing the duration of the isoelectric field heating process 2-3 and of the cooling process 4-1 denoted by τ_{23} and τ_{41}, respectively. For example, the times τ_{23} and τ_{41} varied between approximately 2 and 15 s. However, the durations of the isothermal processes 1-2 (τ_{12}) and 3-4 (τ_{34}) were kept constant at around 1.5 s. Note that the time required to manually transfer the sample between cold and hot baths was about 0.5 s. Overall, the cycle frequency f varied between 0.024 and 0.13 Hz.

The effect of E_L on the energy and power densities produced in the Olsen cycle was assessed with the cold and hot source temperatures T_{cold} and T_{hot} determined from D-E loop measurements. The high electric field was maintained at $E_H = 4.0$ MV/m while the low electric field E_L was varied between 0 and 1.0 MV/m. The low electric field corresponding to a peak in energy density denoted by E_L^*, and to a maximum power density, denoted by E_L^+, were used thereafter in each respective set of measurements.

Procedure (a) in Figure 4.1 was followed in order to obtain the maximum energy density. The Olsen cycle was performed under quasiequilibrium conditions with low electric field E_L^* fixed and temperatures maintained at T_{cold} and T_{hot}. The high electric field E_H was increased from 4.0 MV/m by 0.5 MV/m increments until the sample suffered electromechanical breakdown. On the other hand, procedure (b) in Figure 4.1 was followed to find the conditions for maximum power density. The power density typically reaches a maximum at the peak power frequency larger than the frequency corresponding to quasiequilibrium conditions. Chin *et al.* [87] suggested that the peak power frequency for 9.5/65/35 PLZT was dependent on the applied high electric field. Therefore, the Olsen cycle was performed at cycle frequency vary-

ing between 0.024 and 0.13 Hz with high electric field E_H set as either 5.0, 6.0, or 7.0 MV/m. The low electric field was fixed at the previously determined value of $E_L{}^+$ and temperatures T_{cold} and T_{hot} were held constant. Then, the peak power frequency was identified. Finally, the Olsen cycle was carried out at the peak power frequency for high electric field E_H raised from 5.0 MV/m in 0.5 MV/m increments until the sample experienced dielectric breakdown.

6.2 Results and discussion

6.2.1 Isothermal D-E loops

Figure 6.3 plots the isothermal bipolar D-E loops measured at temperatures between (a) 40 and 250°C for 5/65/35 PLZT Sample 14, (b) 23 and 210°C for 6/65/35 PLZT Sample 16, (c) 25 and 200°C for 7/65/35 PLZT Sample 18, (d) 45 and 190°C for 8/65/35 PLZT Sample 20 (e) 3 and 150°C for 9/65/35 PLZT Sample 22, and (f) -110 and 40°C for 10/65/35 PLZT Sample 24. The bipolar D-E loops were similar among samples of the same composition for any given temperature.

These measurements showed that the isothermal D-E loops overlapped and exhibited square ferroelectric behavior at relatively low temperatures when the remnant polarization was maximum. However, as the temperature increased, the isothermal D-E loops degenerated into narrow and linear loops [77]. Then, the remnant polarization gradually decreased and dropped sharply to ∼0.02 C/m^2 beyond a critical temperature we will call the polarization transition temperature and denote by T_p. Similarly, Figure 6.3 indicates that the coercive field E_C decreased with increasing temperature for all compositions. This behavior was attributed to rapid dipole fluctuations at high temperatures contributing to the energy required for polarization switching. Moreover, the coercive fields were smaller for 9/65/35 PLZT than for 5/65/35 PLZT. This can be explained by a structural transformation from rhombohedral ferroelectric to slim loop cubic as the lanthanum doping level x increased from 5 to 9 mol.%.

Note that the isothermal D-E loops of 10/65/35 PLZT at 25, 30, and 40°C (Figure

6.3f) were slim and featured small remnant polarization, characteristic of the relaxor phase. Moreover, the isothermal D-E loops of 10/65/35 PLZT did not exhibit open loop ferroelectric behavior until the temperature was lowered to -70°C. Similar behavior was observed with 11/65/35 PLZT samples. Unfortunately, temperatures below 0°C are unpractical for waste heat energy harvesting applications and therefore x/65/35 PLZT samples with $x \geq 10$ mol.% were not considered further.

6.2.2 Polarization transition temperature

Figure 6.4a shows the remnant polarization of x/65/35 PLZT as a function of temperature for lanthanum doping level x between 5 and 10 mol.%. The solid lines representing polynomial fits are also plotted to guide the eye. The remnant polarization was large in the ferroelectric state for each composition. This was the manifestation of the cooperative ordering of dipole orientation at low temperatures [69]. However, the remnant polarization decreased with increasing temperature until it reached negligibly small values ($P_r \leq 0.02$ C/m^2) beyond the polarization transition temperature T_p. The small remnant polarization at high temperatures was evidence of the dipole disorder induced by rapid thermal fluctuations. Note that the remnant polarization $P_r(T)$ of ferroelectric relaxors retained finite values above T_p due to the persistence of nanopolar domains interacting with each other at temperatures between T_p and T_B [131].

Figure 6.4b plots the x/65/35 PLZT polarization transition temperature T_p for lanthanum doping level x between 5 and 10 mol.%. The values of T_p are also summarized in Table 6.1. Figure 4.3b shows that the polarization transition temperature decreased from 240 to 10°C as the molar fraction of lanthanum dopant increased from 5 to 10 mol.%. In order to achieve a large change in electric displacement necessary to obtain a large energy density, the Olsen cycle should be performed on PLZT samples between T_{cold} and $T_{hot} \geq T_p$. This suggests that these different PLZT compositions should be operated over different temperature ranges to achieve maximum thermal to electrical energy conversion.
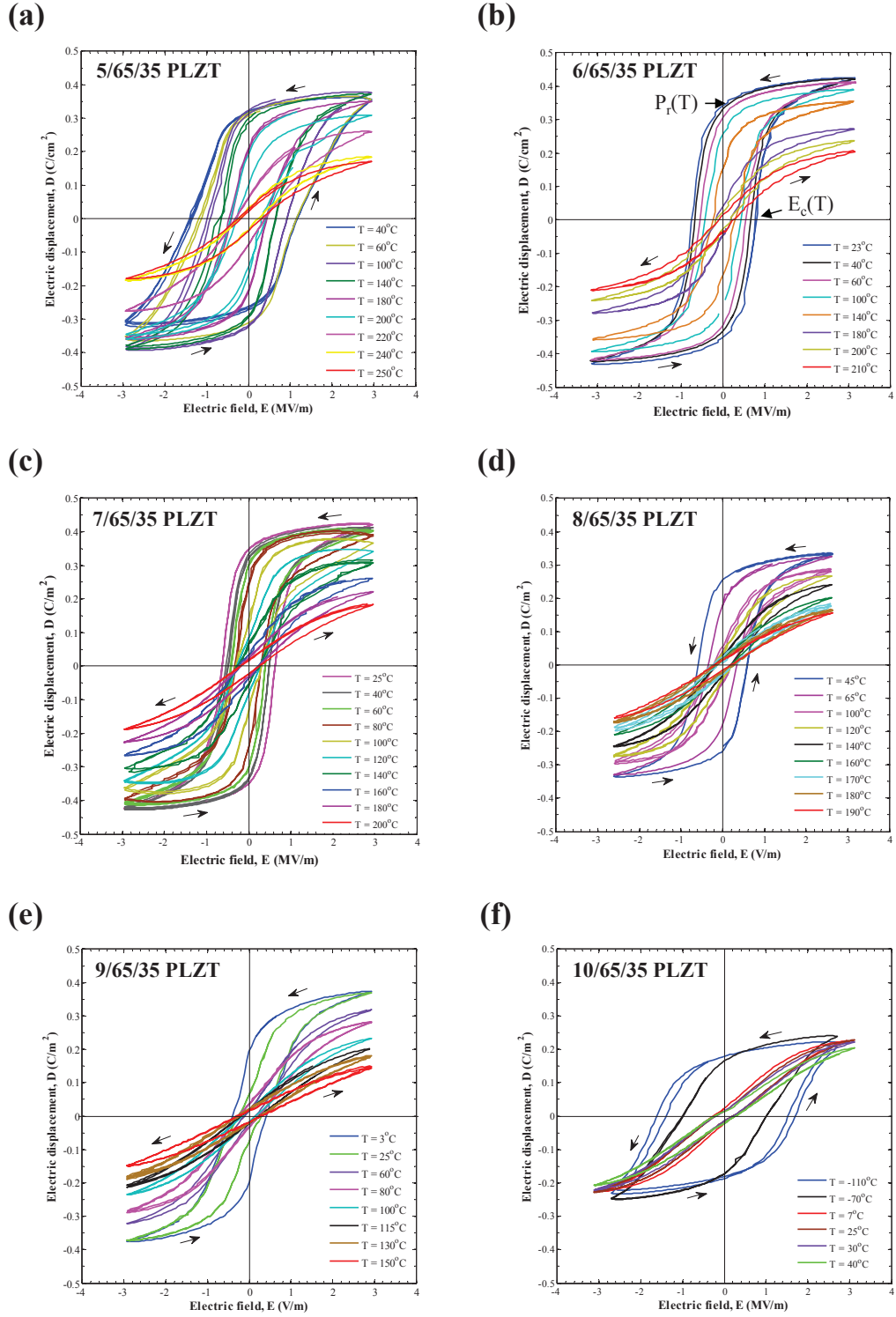
Figure 6.3: Bipolar isothermal electric displacement versus electric field (D-E) hysteresis curves measured at 0.1 Hz for (a) 5/65/35 PLZT, (b) 6/65/35 PLZT, (c) 7/65/35 PLZT, (d) 8/65/35 PLZT, (e) 9/65/35 PLZT, and (f) 10/65/35 PLZT at various temperatures. The temperatures corresponding to open loop ferroelectric behavior decreased as the lanthanum doping level x increased.
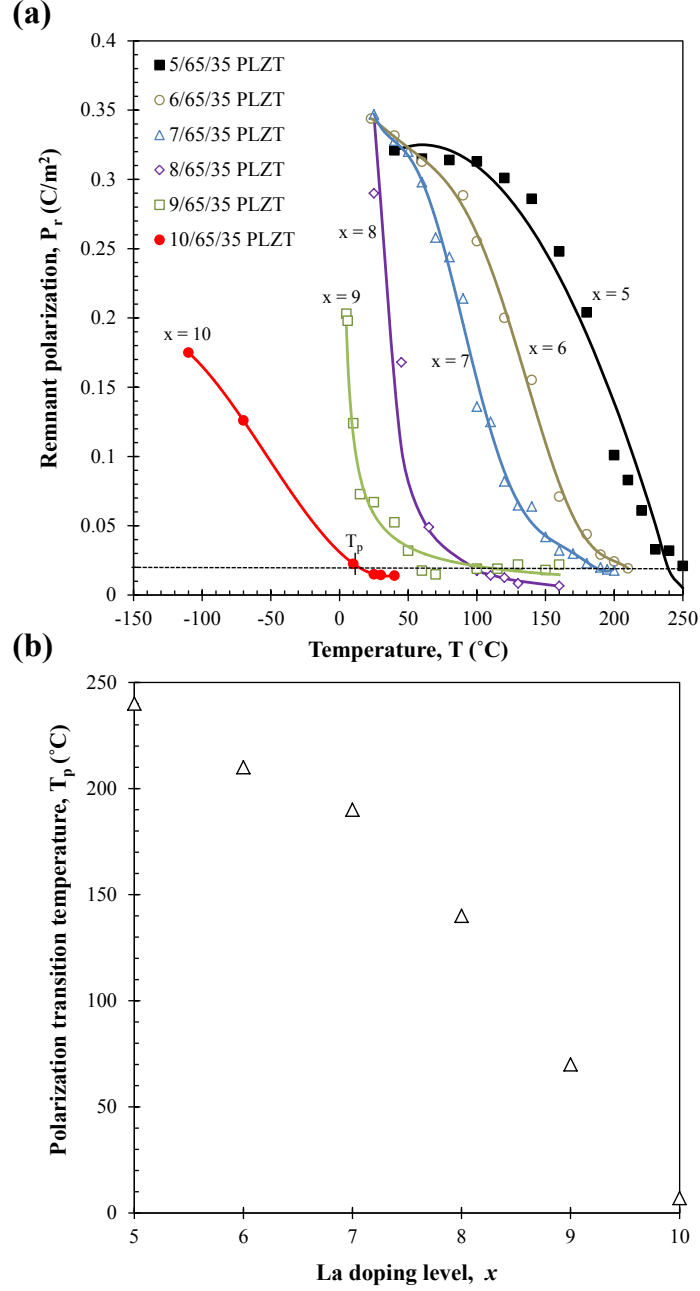
Figure 6.4: (a) Remnant polarization extracted from isothermal D-E loops measured at 0.1 Hz as a function of temperature for various x/65/35 PLZT compositions with x between 5 and 10 mol.%. The solid lines representing polynomial fits of measured data are also plotted to guide the eye. The remnant polarization $P_r(T)$ corresponds to the polarization under zero applied electric field. (b) Polarization transition temperature T_p of x/65/35 PLZT as a function of lanthanum doping level x varying from 5 to 10 mol.%. We define the polarization transition temperature T_p as the temperature corresponding to a transition from large to negligibly small remnant polarization ($P_r \leq 0.02$ C/m^2).

6.2.3 Curie temperature

The Curie temperature is typically defined as the temperature corresponding to the maximum dielectric constant. Figure 6.5 plots the large field dielectric constant of (a) 5/65/35 PLZT and (b) 9/65/35 PLZT at 0.1 Hz as a function of temperature. The large field dielectric constants were retrieved from the isothermal bipolar D-E loops as the slope of the linear fit corresponding to an isothermal field reduction from $E_{cr}(T)$ extrapolated to 0 MV/m. Table 6.1 presents the Curie temperature of $x/65/35$ PLZT for x between 5 and 9 mol.%. Dielectric constant measurements for 5/65/35 PLZT at 0.1 Hz show that the Curie temperature T_{Curie} was similar to the polarization transition temperature T_p and equal to 240°C. TThis is consistent with the fact that classical ferroelectric materials including 5/65/35 PLZT do not exhibit frequency dispersion [70, 132]. However, for 9/65/35 PLZT, the Curie temperature $T_{Curie} = 15^o$C fell below the polarization transition temperature estimated as $T_p = 70^o$C at 0.1 Hz. This can be attributed to the pronounced frequency dispersion featured in relaxor ferroelectric $x/65/35$ PLZT compositions for $x \geq 6$-7 mol.% as discussed in Ref. [133]. In fact, the Curie temperature of relaxor ferroelectric materials is frequency-dependent and shifts to higher values with increasing frequency [70].

6.2.4 Effect of low electric field E_L

Table 6.2 summarizes the operating temperature ranges, applied electric fields, and maximum energy and power densities generated in the present study by subjecting PLZT ceramics with various lanthanum doping concentrations to the Olsen cycle. Figure 6.6a plots six different Olsen cycles on the D-E diagram executed on 9/65/35 PLZT Sample 10 with low electric field E_L equal to 0, 0.1, 0.2, 0.3, 0.4, and 0.5 MV/m. This composition was selected for illustration purposes. The high electric field E_H was set as 4.0 MV/m while the cold and hot source temperatures were maintained at 3 and 150°C, respectively. Due to the measurement method of electric displacement D in the Olsen cycle, it was only possible to measure changes in electric displacement rather than absolute displacement. Therefore, the Olsen cycles shown were vertically translated to coincide at T_{hot} and E_H (state 3).

(a)

(b)
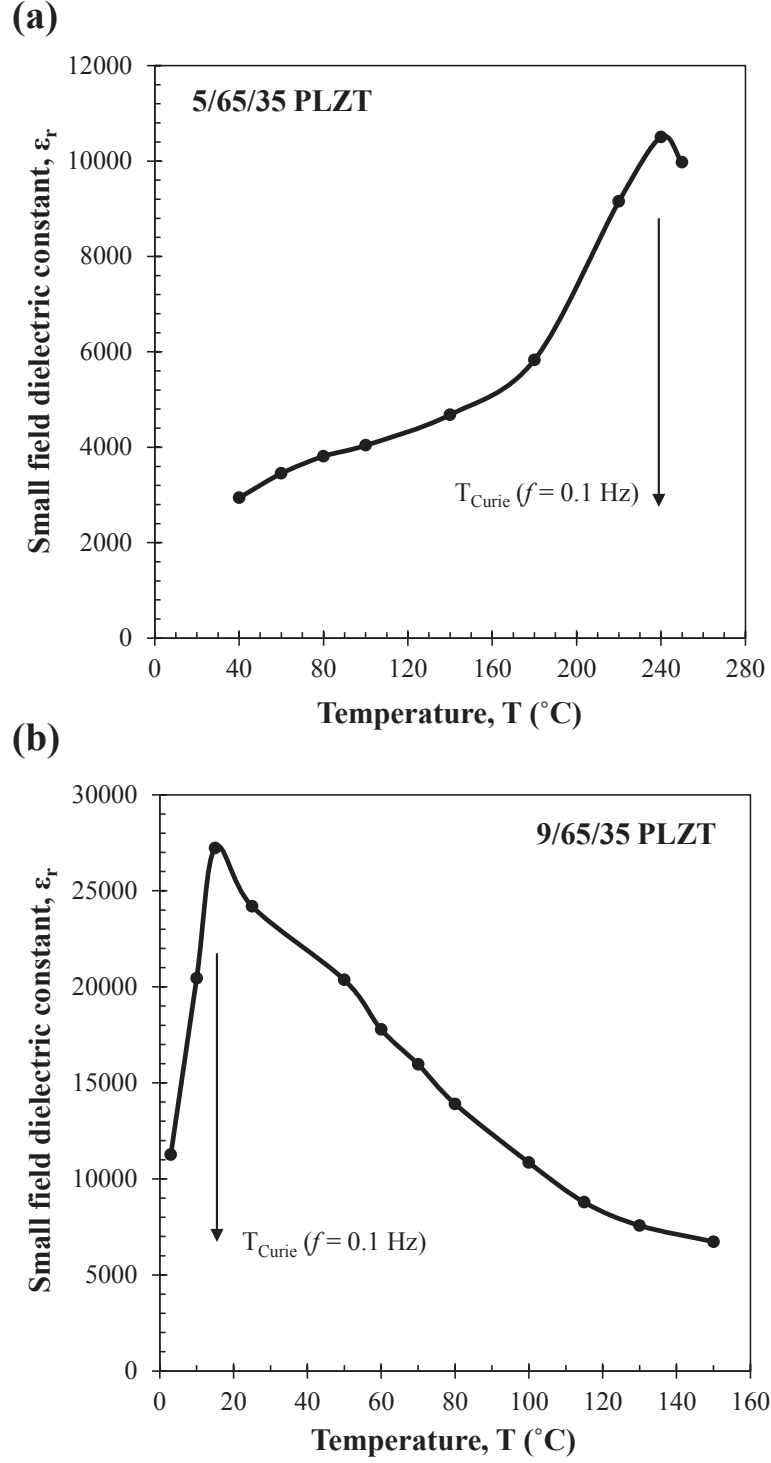
Figure 6.5: Small field dielectric constant $\varepsilon_r(E,T)$ for (a) 5/65/35 PLZT and (b) 9/65/35 PLZT as a function of temperature retrieved from isothermal bipolar D-E loops measured at 0.1 Hz as the slope of the linear fit corresponding to isothermal field reduction from $E_{cr}(T)$ to 0 MV/m. The Curie temperature at 0.1 Hz was identified as the temperature corresponding to the maximum value of ε_r.

(a)

(b)
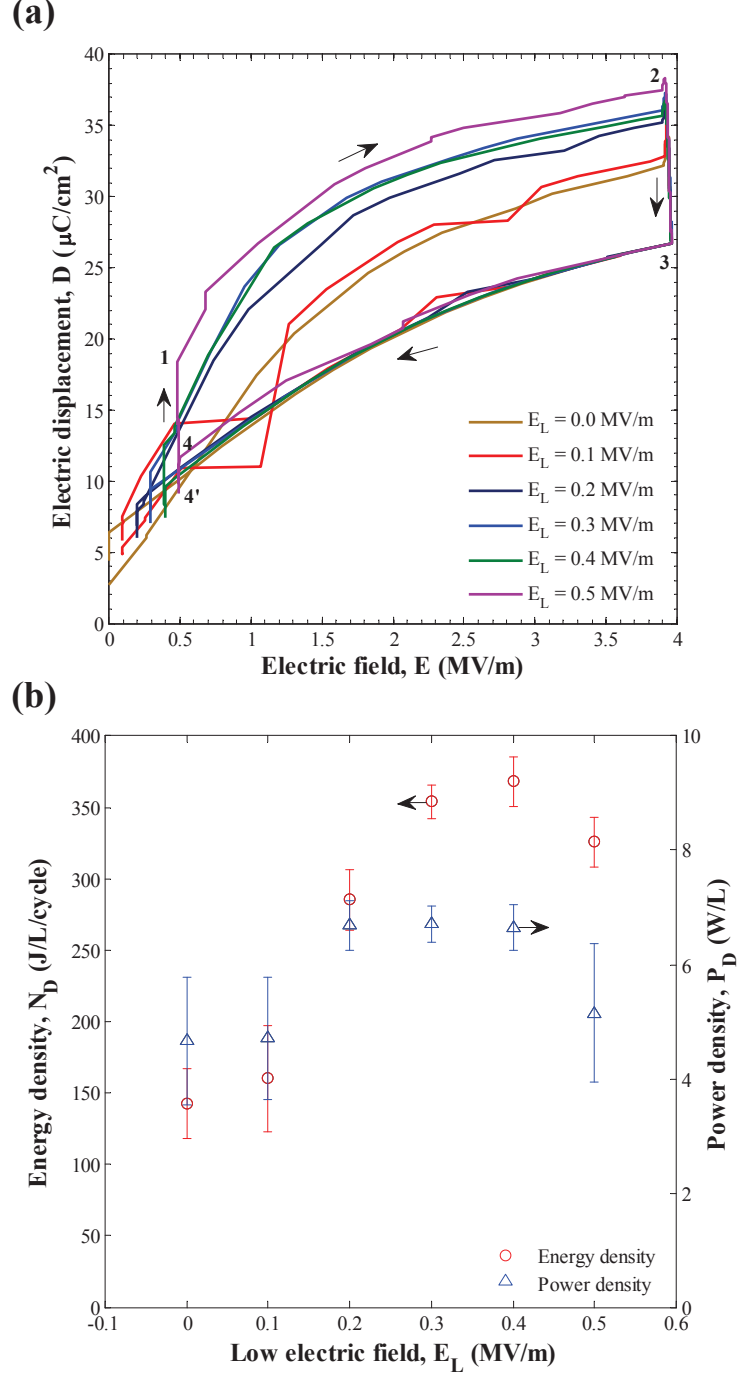
Figure 6.6: (a) Experimental Olsen cycle in the D-E diagram performed on 9/65/35 PLZT Sample 23 between $T_{cold} = 3^oC$ and $T_{hot} = 150^oC$ for $E_H = 4.0$ MV/m and E_L varying from 0 to 0.5 MV/m. The Olsen cycles were vertically displaced to coincide at T_{hot} and E_H (state 3). (b) The corresponding energy and power densities generated with Sample 23 for five different Olsen cycles performed under the above conditions. A peak in energy density was reached at $E_L^* = 0.4$ MV/m while a peak in power density was obtained for $E_L^+ = 0.2$ MV/m.

Table 6.2: Maximum energy and power densities achieved using the Olsen cycle for different materials, temperature ranges, operating electric fields, and cycle frequencies.

Sample	Material	T_{cold} °C	T_{hot} °C	$E_L{}^*$ MV/m	E_H MV/m	f Hz	$N_{D,max}$ J/L/cycle
1	5/65/35 PLZT	40	250	0.4	7.5	0.0296	799.5 ± 11.3
3	6/65/35 PLZT	40	210	0.4	8.5	0.0353	949.3 ± 11.2
5	7/65/35 PLZT	30	200	0.2	7.0	0.0256	1013.5 ± 16.2
7	8/65/35 PLZT	25	160	0.2	7.5	0.0178	887.5 ± 8.5
9	9/65/35 PLZT	3	150	0.4	7.5	0.0191	653.5 ± 34.3

Sample	Material	T_{cold} °C	T_{hot} °C	$E_L{}^+$ MV/m	E_H MV/m	f Hz	$P_{D,max}$ W/L
2	5/65/35 PLZT	40	250	0.4	9.0	0.0656	41.8 ± 2.2
4	6/65/35 PLZT	40	210	0.0	8.5	0.0604	47.9 ± 1.0
6	7/65/35 PLZT	30	200	0.0	9.5	0.0839	47.5 ± 0.3
8	8/65/35 PLZT	25	160	0.2	9.0	0.0627	39.5 ± 2.0
10	9/65/35 PLZT	3	150	0.2	7.0	0.0710	35.9 ± 0.6

Figure 6.6b shows the energy density and power density generated by Sample 10 as a function of E_L ranging between 0.0 and 0.5 MV/m corresponding to data shown in Figure 6.6a. The error bars correspond to two standard deviations or a 95% confidence interval. The error bars associated with P_D account for uncertainties for both energy density N_D and frequency f and were estimated from error propagation analysis. This explains why the errors bars for P_D are larger than those for N_D. It is evident that the energy density reached a maximum at $E_L^* = 0.4$ MV/m. As E_L decreased from 0.4 to 0.0 MV/m, a sharp decrease in the average energy density from 368.2 to 143.0 J/L/cycle was observed. This reduction can be explained by the fact that the sample was unable to re-polarize at zero electric field when the temperature decreased from T_{hot} to T_{cold} (Process 4-1). Unfortunately, de-poling the sample below or near the coercive field $E_C = 0.09$ MV/m at $T_{hot} = 150^oC$ resulted in crossovers in the Olsen cycle D-E curve between processes 1-2 and 3-4 as shown in Figure 6.6a ($E_L = 0$ MV/m) and a smaller energy density. Meanwhile, raising the low electric field E_L from 0.4 to 0.5 MV/m reduced the average energy density from 368.2 to 325.7 J/L/cycle. This was due to the smaller electric field span (E_H - E_L) imposed in the Olsen cycle. Similarly, Figure 6.6b shows that the largest power density was obtained for the low electric field set as $E_L^+ = 0.2$ MV/m. However, the power densities achieved with low electric fields $E_L = 0.2$, 0.3, and 0.4 MV/m were found to be relatively similar and within the experimental uncertainty of 0.036 W/L corresponding to a maximum difference of 1%. Similar results were obtained for other PLZT compositions. The values of E_L^* and E_L^+ for each composition are summarized in Table 6.2.

6.2.5   Effect of high electric field E_H

Figure 6.7 plots the energy densities generated by x/65/35 PLZT as a function of high electric field E_H ranging from 3.0 to 9.5 MV/m for $5 \leq x \leq 9$ mol.%. In all cases, E_L was set to E_L^*, previously estimated. Similarly, the optimum temperatures T_{cold} and $T_{hot} \geq T_{Curie}$ for each composition were imposed, as summarized in Table 6.2. Figure 6.7 indicates that raising the electric field span (E_H - E_L^*) resulted in larger energy densities. For example, the average energy density generated by a 190 μm thick 7/65/35 PLZT sample increased by 51%

from 553.0 to 832.8 J/L/cycle as the high electric field E_H increased from 4.0 to 6.0 MV/m (Figure 6.7c). However, the maximum value of E_H was limited by the samples' dielectric breakdown. Cracks formed within the samples beyond an applied electric field threshold. The formation of cracks may be attributed to mechanical stresses in the material along the grain boundaries due to spatially varying electric fields causing preferential domain wall motion [123]. Microcracks may then propagate along the grain boundaries of the samples under the cyclic electric field loading/unloading. Ultimately, the field-induced crack propagation led to sample failure.

Figure 6.7c also shows that the energy density of 7/65/35 PLZT increased with increasing high electric field E_H up to 7.0 MV/m and then decreased for $E_H = 8.0$ MV/m. This can be attributed to a significant increase in leakage current at large electric fields. Samples of other compositions investigated in this study were unable to withstand electric field large enough to observe this behavior.

6.2.6   Maximum energy density

Figure 6.7c also shows that a maximum energy density of 1013.5 ± 16.2 J/L/cycle, corresponding to a power density of 25.9 ± 0.8 W/L, was obtained with 7/65/35 PLZT. The Olsen cycles were performed under quasiequilibrium conditions at 0.0256 Hz with electric field cycled between $E_L = E_L{}^* = 0.2$ MV/m and $E_H = 7.0$ MV/m. The cold and hot source temperatures were equal to $T_{cold} = 30^oC$ and $T_{hot} = 200^oC$, respectively. To the best of our knowledge, this energy density is the largest achieved using the Olsen cycle among pyroelectric single crystals, ceramics, and polymeric materials reported to date.

Figure 6.8 presents six consecutive Olsen cycles on the D-E diagram corresponding to this maximum energy density. The D-E paths of the Olsen cycles were not closed since Points 4 and 4' did not coincide. The offset between points 4' and 4 can be explained by the leakage current observed across the PLZT ceramic at high temperatures and/or large electric fields [6, 25, 36, 99] as previously discussed. Note that the Olsen cycles plotted in Figure 6.8 did not follow a smooth path between E_L and E_H during isothermal processes
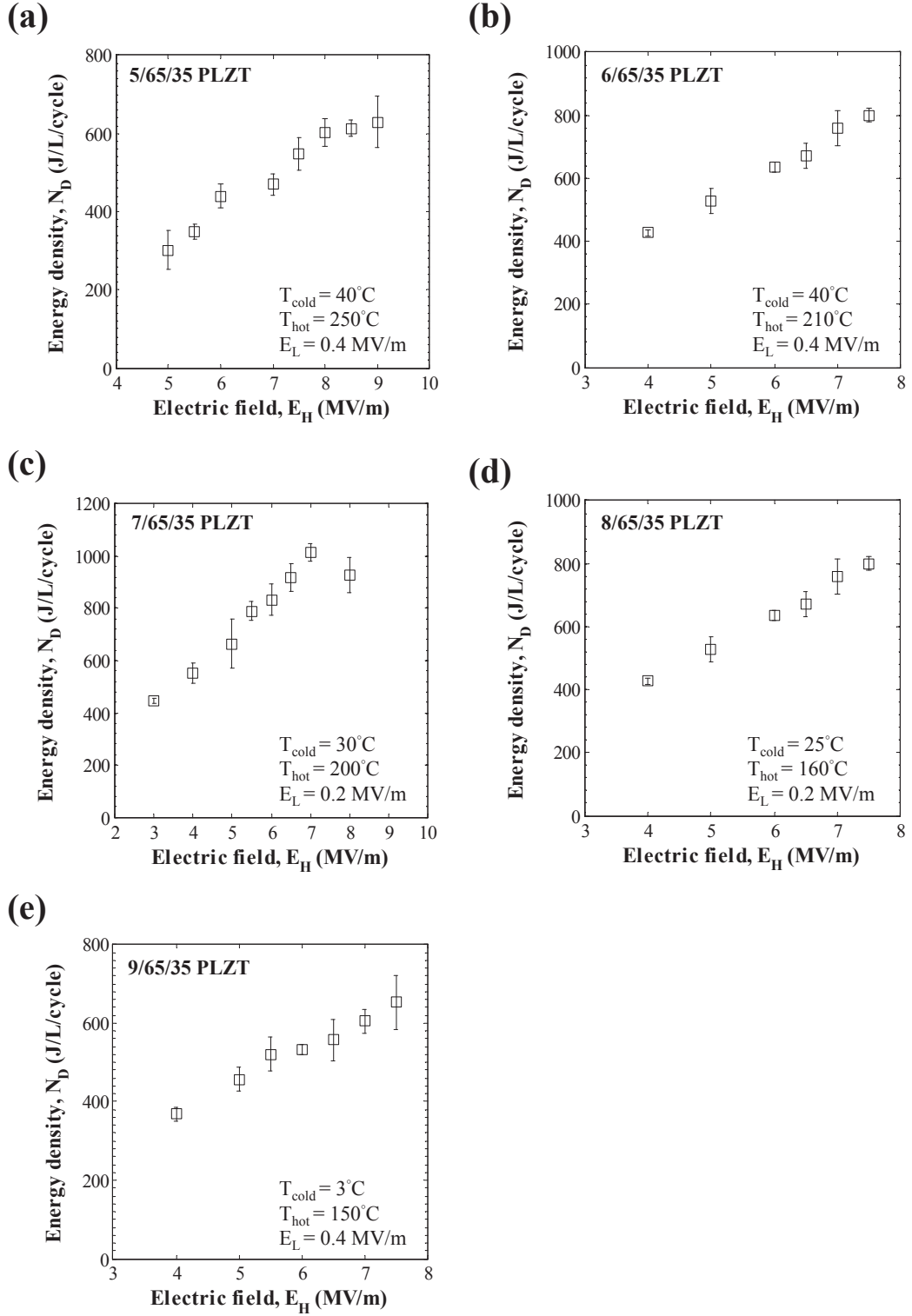
Figure 6.7: Experimentally measured energy density produced by (a) 5/65/35 PLZT, (b) 6/65/35 PLZT, (c) 7/65/35 PLZT, (d) 8/65/35 PLZT, and (e) 9/65/35 PLZT as a function of high electric field for Olsen cycles performed under quasiequilibrium conditions with E_L = $E_L{}^*$ and the optimum temperatures T_{cold} and T_{hot} for each composition.

1-2 and 3-4 in the D-E diagram. This was likely due to microcracks propagating along the grain boundaries of the sample while the Olsen cycle was performed under high electric fields and/or high temperatures [115]. These fractures introduced spatial variations in the local electric field near the crack front resulting in sample inhomogeneity [116].

6.2.7   Effect of cycle frequency f

For illustration purposes, Figure 6.9 plots both the energy and the power densities obtained with 9/65/35 PLZT as a function of cycle frequency, as previously described, for $E_L{}^+ = 0.2$ MV/m and $E_H = 6.0$ MV/m. The cold and hot temperatures were $T_{cold} = 3^oC$ and $T_{hot} = 150^oC$, respectively. The four different processes in the Olsen cycle performed at frequencies below 0.036 Hz corresponded to quasiequilibrium conditions. Figure 6.9 indicates that, under the above conditions, the energy density reached a maximum of 509.4 $\pm$ 29.6 J/L/cycle at 0.036 Hz and then decreased with increasing cycle frequency. The rise in N_D can be explained by the excessive leakage current observed in the material with frequency below 0.036 Hz. Smaller frequencies provided an opportunity for charges at the surface of the PE to conduct through its body (leakage current) particularly under large applied electric field and/or high operating temperature. As the cycle frequency decreases, the sample is subject to these unfavorable conditions for a longer duration. The leakage current can be estimated from the surface between states 4, 3, and 4'. For 9/65/35 PLZT, the loss in energy density associated with the leakage current was estimated to be 10% when the Olsen cycle was performed under quasiequilibrium conditions at 0.036 Hz. The loss increased to 20% when the cycle frequency was reduced to around 0.02 Hz. On the other hand, as the cycle frequency increased beyond 0.036 Hz, the energy density decreased due to a reduction in electric displacement span as the processes were not performed under quasiequilibrium conditions (i.e. the Olsen cycle did not span the isothermal D-E loops).

Figure 6.9 also indicates that under the above described operating conditions, the power density P_D from 9/65/35 PLZT reached a maximum of 32.4 $\pm$ 0.8 W/L at the peak power frequency of 0.096 Hz. Performing the Olsen cycle at frequencies greater than 0.096 Hz led to
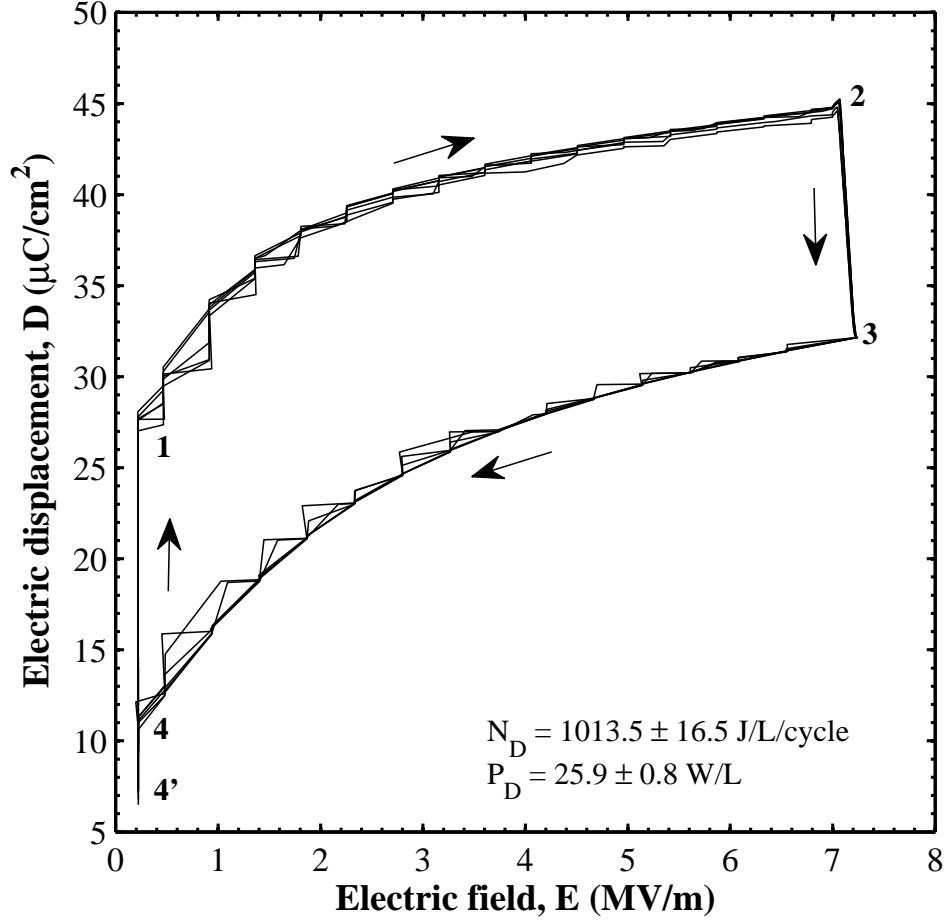
Figure 6.8: Electric displacement versus electric field diagram for six experimental Olsen cycles using 7/65/35 PLZT Sample 5. The electric field was cycled between $E_L = E_L^* = 0.2$ MV/m and $E_H = 7.0$ MV/m while the temperature varied between $T_{cold} = 30^oC$ and T_{hot} = 200^oC. The average energy density over six cycles was 1013.5 ± 16.2 J/L/cycle at 0.0256 Hz, corresponding to the largest energy density achieved in this study.

a smaller power output. This behavior may be explained by considering the relaxation and heat transfer mechanisms. First, the dipole realignment occurring during the isoelectric field heating and cooling processes 2-3 and 4-1 did not have time to complete at frequencies larger than 0.096 Hz due to the slow dipole relaxation inherent to ferroelectric relaxor materials, particularly at temperatures below T_{Curie} [134]. This is caused by the high energy barrier required to reorient the frozen nanodomains at low temperatures [113]. Second, the samples were unable to reach thermal equilibrium when the Olsen cycle was performed at large cycle frequencies. In other words, the temperature swings of the pyroelectric material did not reach the temperature of the oil baths during processes 2-3 and 4-1. Therefore, phase transitions may be incomplete resulting in a smaller electric displacement span. Thus, the electrical energy and power output were small. Although the energy density generated by Sample 10 decreased from 509 to 336 J/L/cycle as the frequency increased from 0.036 to 0.096 Hz, the corresponding power density increased from 18.8 to 32.4 W/L. This confirms that $P_D = N_D(f)f$ reaches a maximum through a compromise between large frequency f and energy density N_D.

Figure 6.10 plots the power density generated by 9/65/35 PLZT Sample 10 as a function of cycle frequency between 0.02 and 0.13 Hz. The low electric field was set as $E_L = E_L{}^+$ = 0.2 MV/m while the high electric field E_H was set at 5.0, 6.0, or 7.0 MV/m. The cold and hot source temperatures were $T_{cold} = 3^oC$ and $T_{hot} = 150^oC$, respectively. Figure 6.10 indicates that the peak power density increased with increasing high electric field E_H. This is attributed to (i) the increase in energy density N_D due to larger electric field span (E_H - $E_L{}^+$) and (ii) the increase in the time rate of change of the electric field for a given cycle frequency f. Figure 6.10 also indicates that the peak power density was reached at 0.0859, 0.0961, and 0.0709 Hz for high electric field E_H equal to 5.0, 6.0, and 7.0 MV/m, respectively. However, the variations in power density near these frequencies were small. This suggests that the differences in peak power frequency were attributed to measurement error. In order to ensure that the material did not break prematurely due to large thermoelectromechanical stress, the high electric field was imposed to $E_H = 5.0$ MV/m to determine the peak power frequency for testing the other PLZT compositions as summarized in Table 6.2.
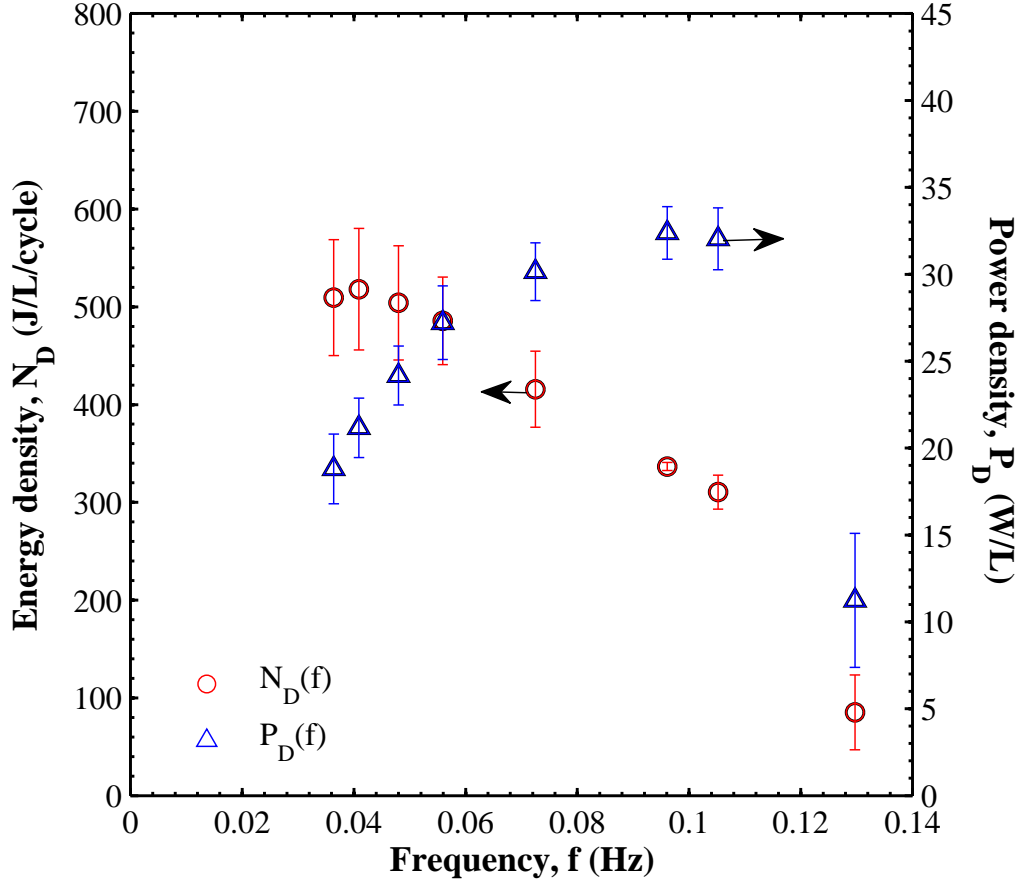
Figure 6.9: Energy and the power densities obtained with 9/65/35 PLZT Sample 23 as a function of cycle frequency for $E_L = 0.2$ MV/m and $E_H = 6.0$ MV/m with $T_{cold} = 3^oC$, and $T_{hot} = 150^oC$. The durations τ_{12} and τ_{34} were equal and fixed at around 1.5 s. The durations τ_{23} and τ_{41} of isoelectric field processes 2-3 and 4-1 were the same and ranged from about 2 to 15 s. The energy density and the power density reached a maximum at 0.0364 and 0.0961 Hz, respectively.
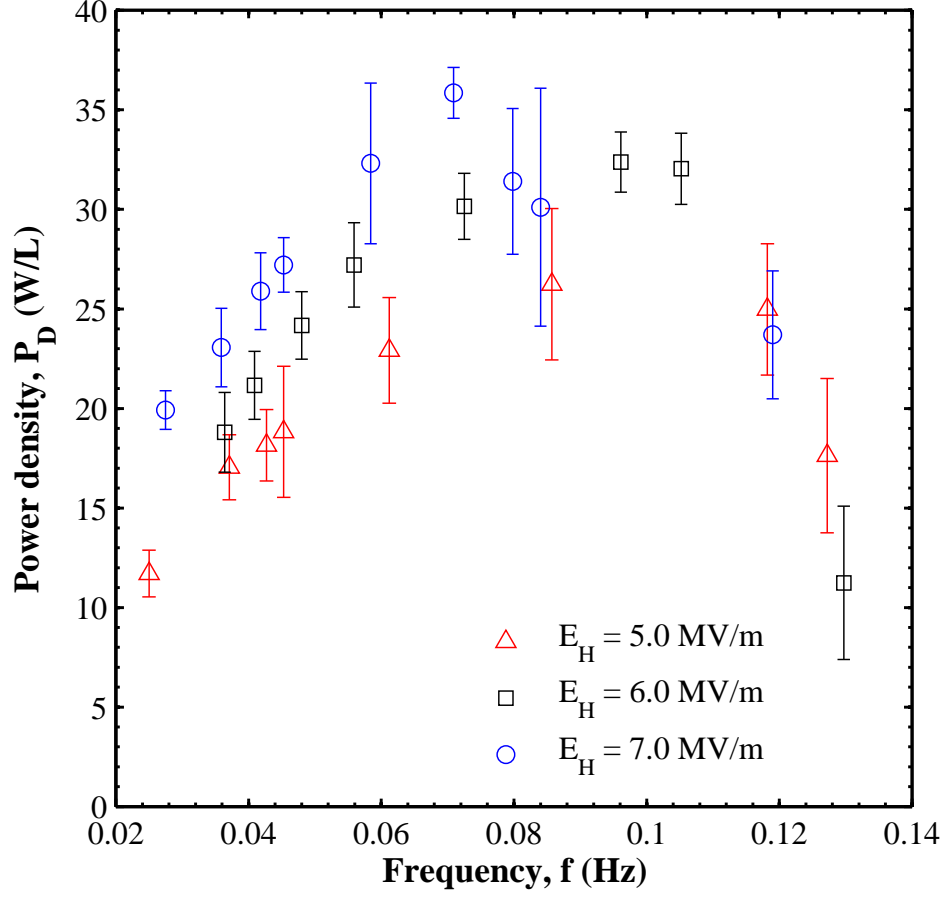
Figure 6.10: Power density generated by 9/65/35 PLZT Sample 23 as a function of cycle frequency between 0.02 and 0.13 Hz. The low electric field E_L was set as 0.2 MV/m while the high electric field E_H was set as either 5.0, 6.0, or 7.0 MV/m. The cold and hot source temperatures were equal to $T_{cold} = 3^oC$ and $T_{hot} = 150^oC$, respectively. The peak power frequency was equal to 0.0859, 0.0961, and 0.0709 Hz for high electric field E_H equal to 5.0, 6.0, and 7.0 MV/m, respectively.

6.2.8 Maximum power density

Figure 6.11 presents isothermal bipolar D-E loops collected on 6/65/35 PLZT Sample 4 at $T_{cold} = 40^oC$ and $T_{hot} = 210^oC$ overlaid with three consecutive Olsen cycles performed at 0.0604 Hz with the electric field cycled between $E_L = E_L{}^+ = 0$ MV/m and $E_H = 8.5$ MV/m. These Olsen cycles represent the largest power density obtained in this study with any PLZT composition investigated. This was due to smaller leakage current (larger N_D) observed in 6/65/35 PLZT and its ability to re-polarize under zero bias electric field unlike the other compositions. This enabled the isoelectric field cooling process to be performed rapidly (larger f). The 6/65/35 PLZT sample was able to re-polarize at $T_{cold} = 40^oC$ and $E_L = 0$ MV/m since these conditions were not near a ferroelectric-relaxor phase boundary.

Figure 6.11 also shows that process 3-4 of the Olsen cycle follows the decreasing electric field path of the isothermal D-E loop at T_{hot}. However, process 1-2 did not follow the increasing electric field path of the isothermal D-E loop at T_{cold}. The fact that the Olsen cycle did not span the electric displacement between the isothermal bipolar D-E loop corresponding to T_{cold} may be attributed to the existence of mixed ferroelectric and ergodic relaxor phases [118,122] when the applied electric field increased from E_L to $E_{cr}(T)$ during the Olsen cycle. These phases co-existed likely due to slow stabilization of the ferroelectric phase from the relaxor phase caused by parasitic interactions between defects and polar nanoregions [122].

6.2.9 Discussion

Table 6.2 indicates that the maximum energy density was reached for all compositions at frequencies between 0.019 and 0.035 Hz. On the other hand, the maximum power output was obtained at higher frequencies between 0.060 and 0.084 Hz. Additionally, the optimum value of E_H imposed for different samples was not the same. This is likely due to the different electric field breakdown inherent to the different compositions and to sample variation caused by parasitic defects introduced during the material synthesis process.

The maximum energy densities of $x/65/35$ PLZT with x ranging from 5 to 9 mol.% outperformed those reported for single crystal PMN-32PT [53] and PZN-4.5PT [58] by a
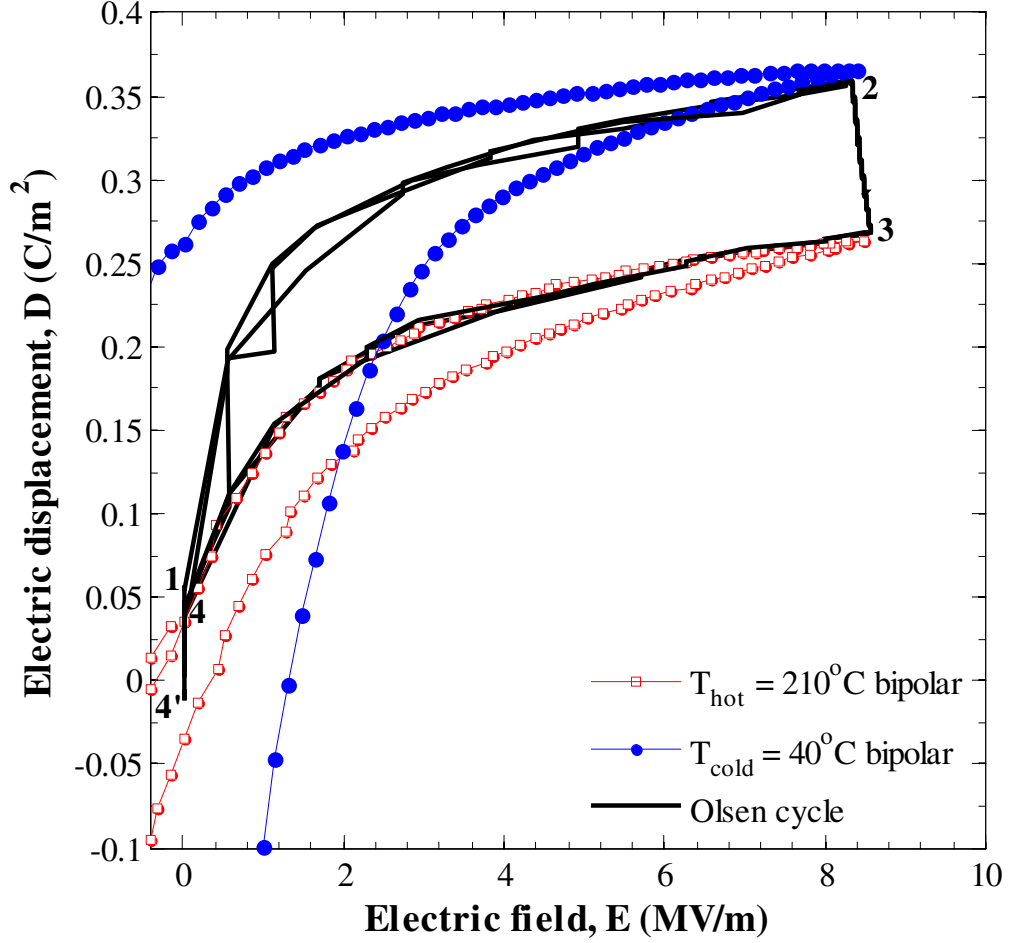
Figure 6.11: D-E diagram of isothermal bipolar D-E loops collected at $T_{cold} = 40^oC$ and $T_{hot} = 210^oC$ overlaid with three consecutive Olsen cycles performed at 0.0604 Hz with the electric field cycled between $E_L = 0.4$ MV/m and $E_H = 8.5$ MV/m. The average power density generated over three cycles was 47.8 $\pm$ 1.0 W/L, representing the largest power output in the present study. The Olsen cycles were vertically displaced to coincide with the isothermal D-E curve at T_{hot}.

factor of four to seven and were nearly twice as large as those obtained with copolymer 60/40 P(VDF-TrFE) [6]. The larger remnant and saturation polarization of PLZT enabled larger electric displacement span in the Olsen cycle thus increasing energy density N_D as suggested by Equation (2.9). Furthermore, using PLZT ceramics offers advantages over 60/40 P(VDF-TrFE) in that PLZT (i) possesses significantly lower leakage current thanks to their higher electrical resistivity, (ii) does not require electrical poling prior to performing the Olsen cycle [6, 36, 52], (iii) requires smaller electric field E_H in the Olsen cycle ($\sim$10 MV/m for PLZT vs. $\sim$50 MV/m for P(VDF-TrFE)) [6], and (iv) is capable of withstanding higher temperatures without melting thus rendering it suitable for temperature up to 250^oC.

6.3   Chapter summary

This chapter reported experimental measurements of the energy and power densities generated by subjecting relaxor ferroelectric x/65/35 PLZT to the Olsen cycle. PLZT thin films with various compositions were synthesized by the mixed oxide method and their thermal-electrical behavior was characterized. The polarization temperature and Curie temperature of the different x/65/35 PLZT compositions were found to increase with lanthanum doping level x. Large energy and power densities were obtained by performing the Olsen cycle on PLZT samples undergoing an ergodic relaxor-ferroelectric phase transition. A maximum energy density of 1014 $\pm$ 16 J/L/cycle was produced by 7/65/35 PLZT under quasiequilibrium conditions at 0.026 Hz for temperatures between $T_{cold} = 30^oC$ and $T_{hot} = 200^oC$ for electric field cycled from $E_L = 0.2$ MV/m to $E_H = 7.0$ MV/m. To the best of our knowledge, this is the largest energy density measured repeatedly among pyroelectric single crystals, ceramics, and polymers using the Olsen cycle. A maximum power density of 48 $\pm$ 1 W/L was obtained by 6/65/35 PLZT at 0.060 Hz for operating temperatures between 40 and 210^oC and electric field cycled from 0 to 8.5 MV/m. The x/65/35 PLZT compositions with x ranging from 5 to 9 mol.% can be used in multistage devices operating between 70 and 240^oC. Future work should focus on (a) fabricating thinner and dense PLZT films to increase electric field breakdown and reduce thermal time constant and (b) constructing and

operating pyroelectric energy harvesting devices.

CHAPTER 7

Conclusion and Future Work

7.1 Conclusion

This study was concerned with waste heat energy conversion using pyroelectric materials and the Olsen cycle. Thermal to electrical energy conversion was demonstrated experimentally using different heat transfer modes and different pyroelectric materials. The Olsen cycle was executed (1) by pressing copolymer P(VDF-TrFE) films against cold and hot aluminum blocks (stamping experiments) or (2) by successively dipping relaxor ferroelectric PLZT samples into cold and hot silicone oil baths (dipping experiments). The energy and power densities generated were compared with those reported in the literature to identify promising pyroelectric materials to use in devices. The effects of operating temperature, electric field, cycle frequency, sample thickness, and electrode material on the energy and power generation performance were systematically investigated. The following subsections summarize the conclusions which can be drawn from this study.

7.1.1 Stamping experiments

The "stamping experiments" were performed to assess the pyroelectric energy and power generation performance of copolymer P(VDF-TrFE) thin film using heat conduction to cool and heat a pyroelectric material. It was established that:

1. The largest energy density produced by 60/40 P(VDF-TrFE) was 155 J/L/cycle at 0.066 Hz for temperatures between $T_{cold} = 46.8^oC$ and $T_{hot} = 99.7^oC$ and electric field cycled between $E_L = 20$ MV/m and $E_H = 35$ MV/m. The corresponding power density

was 10.3 W/L.

2. The largest energy density generated 155 J/L/cycle exceeded the 130 J/L/cycle obtained with our previously operated pyroelectric converter reported in Ref. [7] for similar operating conditions. However, the stamping experiment was significantly simpler to implement.

3. The energy densities generated in the "stamping experiments" were significantly smaller than those obtained in "dipping experiments" [6]. This can be explained by the lower electric field E_H applied in the stamping experiments ($E_H = 290$ to 475 kV/cm) as compared to the dipping experiments ($E_H = 600$ kV/cm). The latter was made possible by the use of silicone oil which has a larger electric breakdown field strength than air [100].

4. The energy generation performance suffered from (1) large thermal contact resistance between the PE and aluminum blocks resulting in poor thermal contact and (2) excessive leakage current for large E_H beyond 35 MV/m and temperature T_{hot} in excess of 110^oC.

5. Power densities of up to four orders of magnitude higher can be generated by using the Olsen cycle rather than simply by using the pyroelectric effect, regardless of the heating and cooling methods used.

7.1.2   Dipping experiments

Successive dipping of a PE into hot and cold dielectric fluid baths under specified electric fields provides a simple and somewhat idealized way to perform the Olsen cycle. The dipping experiments can be used to rapidly assess the energy and power generation performance of pyroelectric materials before using them in actual devices. This was performed on a PLZT ceramic family with a Zr/Ti molar ratio of 65 mol.%/35 mol.% and lanthanum doping level x ranging from 5 to 9.5 mol.%. It was established that:

1. The largest energy density N_D of 1014 J/L/cycle was experimentally measured with

a 190 μm thick 7/65/35 PLZT sample at 0.0256 Hz. This corresponded to a power density of 26 W/L. The cold and hot source temperature were $T_{cold} = 30^oC$ and $T_{hot} = 200^oC$, respectively, while the electric field was cycled between $E_L = E_L{}^* = 0.2$ MV/m and $E_H = 7.0$ MV/m. To the best of our knowledge, this energy density is the largest achieved among pyroelectric single crystals, ceramics, and polymers using the Olsen cycle.

2. The maximum energy densities obtained with PLZT were more than four to seven times greater than those reported for single crystal PMN-32PT [53] and PZN-4.5PT [58] and nearly twice of those obtained with polymer 60/40 P(VDF-TrFE) [6]. This can be explained by the significantly larger product of polarization achieved and electric field applied to PLZT ceramics in comparison to single crystals or polymers.

3. The maximum power density of 55 W/L was obtained with a 190 μm thick 9.5/65/35 PLZT sample at 0.125 Hz. It corresponded to an energy density of 441 J/L per cycle. The cold and hot source temperatures were $T_{cold} = 3^oC$ and $T_{hot} = 140^oC$, respectively, while the electric field was cycled between $E_L = E_L{}^+ = 0.2$ MV/m and $E_H = 6.0$ MV/m. This is comparable to the 58 W/L generated by 60/40 P(VDF-TrFE) polymer for a similar temperature range [6]. However, PLZT is superior to P(VDF-TrFE) since it possesses lower leakage current, does not require electrical poling prior to executing the Olsen cycle, and requires smaller applied voltages in the Olsen cycle.

4. The energy and power densities did not reach a maximum at the same cycle frequency. On the one hand, the maximum energy density was achieved at low cycle frequencies in the Olsen cycle performed under quasiequilibrium conditions. On the other hand, the maximum power density was obtained at larger frequency.

5. An increase in the operating temperature range (T_{hot} - T_{cold}) and/or an increase in the electric field span (E_H - E_L) resulted in larger energy generated. However, these ranges were limited by the thermoelectromechanical stress that the sample can withstand.

6. The dielectric breakdown strength was enhanced by (a) applying a thin layer of sili-

120

cone conformal coating on both faces on each sample and (b) decreasing the sample thickness.

7. Samples containing electrode materials with thermal expansion coefficient close to that of the pyroelectric material were able to sustain larger temperature swings without breakdown.

8. The polarization transition temperatures T_p of $x/65/35$ PLZT were observed to be 240, 210, 190, 140, 70, 65 and 10^oC for lanthanum doping level x equal to 5, 6, 7, 8, 9, 9.5, and 10 mol.% respectively. The Curie temperature T_{Curie} of relaxor ferroelectric $x/65/35$ PLZT fell below the polarization transition temperature T_p for compositions with $x \geq 6$ mol.% [133].

9. Relaxor ferroelectric $x/65/35$ PLZT with x between 5 and 9.5 mol.% is a very promising family of materials to use in pyroelectric waste heat energy harvesting applications between 3 and 250^oC.

10. A physical model for estimating the energy harvested by ferroelectric relaxors was further validated against experimental data (within 40%) for a wide range of electric fields and temperatures.

7.1.3 Optimum temperature windows

In practice, pyroelectric devices are designed to operate within specific temperature ranges. For example, CPUs in laptops and desktops typically work at around 85-100^oC [135] and could serve as a hot source for the Olsen cycle. As previously mentioned, the performance of pyroelectric materials is highly dependent on their operating temperatures. Therefore, it is necessary to characterize each pyroelectric material into its optimal temperature range. This facilitates the selection of promising materials to use in devices.

Table 7.1 compares the maximum energy and power densities generated from the Olsen cycle for different materials, temperature ranges, and operating electric fields as reported in the literature or measured in the present study. The largest energy density was achieved with

7/65/35 PLZT for temperatures between $T_{cold} = 30^{o}$C and $T_{hot} = 200^{o}$C while the electric field was cycled between 0.2 and 7.0 MV/m. Similarly, Table 7.2 compares the maximum power densities generated for the same materials considered in Table 7.1. Figure 7.1 plots the temperature windows associated with different pyroelectric materials in ascending order of maximum power density. The temperature windows are bounded by the cold and hot source temperatures imposed in the Olsen cycle to generate the maximum amount of electrical power. Figure 7.1 indicates that the different $x/65/35$ PLZT compositions with x between 5 and 9 mol.% can be used for applications between 3 and 250°C.
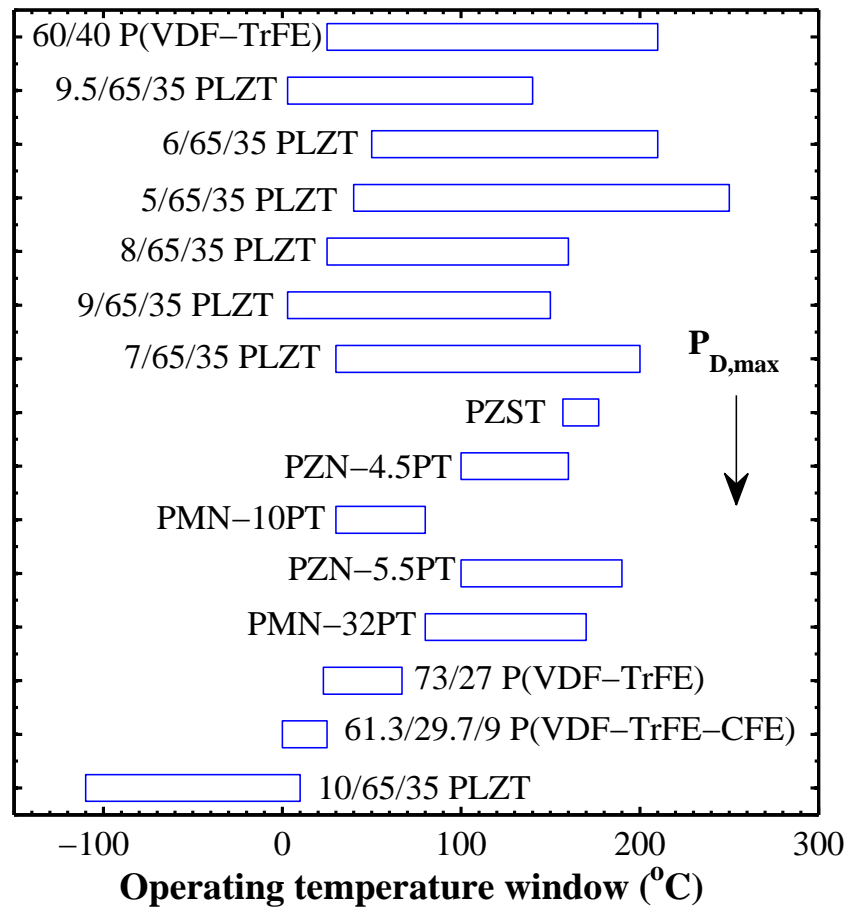
Figure 7.1: Operating temperature windows for various pyroelectric materials subject to the Olsen cycle, in ascending order of maximum power density. The temperature windows were bounded by the cold and hot source temperatures imposed in the Olsen cycle.

Table 7.1: Comparison of maximum energy density achieved using the Olsen cycle (or Ericsson cycle) for different materials, temperature ranges, and operating electric fields.

Material	T_{cold} ^{o}C	T_{hot} ^{o}C	E_L MV/m	E_H MV/m	$N_{D,max}$ J/L/cycle	Ref.
PZST	157	177	0.4	3.2	131	[22]
PZST	145	178	1.2	3.2	130	[19]
PZST	146	159	0.0	2.9	100	[23]
PZST	110	170	0.0	2.8	0.4	[21]
73/27 P(VDF-TrFE)	23	67	23.0	53.0	30	[36]
60/40 P(VDF-TrFE)	58	77	4.1	47.2	52	[4]
60/40 P(VDF-TrFE)	67	81	20.3	37.9	130	[7]
60/40 P(VDF-TrFE)	25	110	20.0	50.0	521	[6]
60/40 P(VDF-TrFE)	25	120	20.0	60.0	900	[5]
61.3/29.7/9 P(VDF-TrFE-CFE)	0	25	0.0	25.0	50	[117]
PZN-4.5PT	100	160	0.0	2.0	217	[29]
PZN-5.5PT	100	190	0.0	1.2	150	[58]
PMN-10PT	30	80	0.0	3.5	186	[44]
PMN-32PT	180	170	0.0	0.9	100	[53]
5/65/35 PLZT	40	250	0.4	7.5	799.5	
6/65/35 PLZT	40	210	0.4	8.5	949.3	
7/65/35 PLZT	30	200	0.2	7.0	1013.5	
8/65/35 PLZT	25	160	0.2	7.5	888.0	[86]
9/65/35 PLZT	3	150	0.4	7.5	653.5	
9.5/65/35 PLZT	3	140	0.2	6.0	637.0	[87]

Table 7.2: Summary of maximum power density obtained using the Olsen cycle (or Ericsson cycle) for different materials, temperature ranges, operating electric fields, and frequencies.

Material	T_{cold} °C	T_{hot} °C	E_L MV/m	E_H MV/m	f Hz	$P_{D,max}$ W/L	Ref.
PZST	156.8	177.4	0.4	2.8	0.26	33.9	[22]
73/27 P(VDF-TrFE)	23.0	67.0	23.0	53.0	0.079	2.38	[36]
60/40 P(VDF-TrFE)	25.0	120.0	20.0	50.0	0.125	112.5	[5]
60/40 P(VDF-TrFE)	58.3	76.5	4.0	48.0	0.256	13.3	[4]
60/40 P(VDF-TrFE)	67.3	81.4	20.2	37.9	0.12	10.7	[7]
60/40 P(VDF-TrFE)	25.0	120.0	20.0	50.0	0.13	58.0	[6]
PZN-4.5PT	100.0	160.0	0.0	1.0	0.10	24.3	[29]
PZN-5.5PT	100.0	190.0	0.0	1.5	0.10	11.7	[58]
PMN-32PT	80.0	170.0	0.2	0.9	0.049	4.92	[53]
5/65/35 PLZT	40.0	250.0	0.4	9.0	0.0656	41.8	
6/65/35 PLZT	40.0	210.0	0.0	8.5	0.0604	47.9	
7/65/35 PLZT	30.0	200.0	0.0	8.5	0.0839	47.5	
8/65/35 PLZT	25.0	160.0	0.2	9.0	0.0627	39.5	
9/65/35 PLZT	3.0	150.0	0.2	7.0	0.0710	35.9	
9.5/65/35 PLZT	3.0	140.0	0.2	6.0	0.125	55.3	[87]

7.2 Recommendations and future work

In order to make pyroelectric energy conversion a more competitive and practical technology, further research should focus on improving the material performance and constructing and operating prototypical pyroelectric converters. Recommendations for future work are as follows:

1. **Increase electric displacement span**

    The energy and power densities of a pyroelectric material can be improved by increasing the electric displacement span as it undergoes the energy conversion cycle (see D-E diagram).

    The change in electric displacement is directly related to the magnitude of the material's spontaneous or remnant polarization. Therefore, materials with large spontaneous or remnant polarization need to be identified. For example, PLZT compositions along the morphotropic phase boundary ($x/52/48$) possess a large dielectric constant, remnant polarization, and piezoelectric coefficient due to strong electromechanical coupling [68]. In fact, the remnant polarizations of 2/65/35 PLZT and 8/65/35 PLZT at room temperature were reported to be 39 and 35 C/m^2, respectively [68]. This suggests that energy density generated by 2/65/35 PLZT could be larger than the 888 J/L/cycle achieved with 8/65/35 PLZT [86]. Therefore, PLZT systems near the morphotropic phase boundary may be attractive for pyroelectric energy conversion and their energy generation capabilities should be assessed.

    Recently studies demonstrated that application of compressive uniaxial stress on a piezoelectric material results in a reduction in polarization [136, 137]. In addition, the Curie temperature of bulk perovskite ferroelastic BaTiO$_3$ was observed to shift to lower temperatures with applied hydrostatic pressure [54]. Refs. [138, 139] reports the Curie temperature of BaTiO$_3$ and SrTiO$_3$ to shift by more than 300°C through controlling the applied biaxial stress. These studies suggest that bias stress could be applied to a pyroelectric sample during processes 2-3 and 3-4 of a modified Olsen cycle to increase the electric displacement span achieved. This technique should be demonstrated on

different piezoelectric and ferroelastic materials to explore the effect of applied stress on the energy density N_D.

2. **Increase dielectric breakdown field**

The energy and power densities of PLZT could also be further increased by increasing the electrical breakdown strength of the material. Additionally, the power density can be increased by increasing the thermal cycling frequency. Both can be achieved by fabricating thin film samples to increase the applied electric field without sample failure [75] and to reduce the thermal time constant τ_t, thus shortening the duration required for samples to reach thermal equilibrium during isoelectric field processes 2-3 and 4-1. For example, reducing the specimen film thickness from 200 to 10 μm decreases the thermal time constant in the dipping experiments from 1.7 to less than 0.1 s. The use of thin film PLZT on substrates would also substantially reduce the applied voltage delivered to the electrical circuit during the Olsen cycle. For example, only 8 V applied across a 10 μm thin PLZT film would be required to achieve an electric field of 8.0 MV/m instead of 1600 V required across a 200 μm thick sample. Then, the Olsen cycle could be easily implemented in devices.

The dielectric breakdown field can be increased by reducing its porosity. Yin *et al.* [140] reported the porosity of PLZT ceramics synthesized by the mixed oxide method to be around 5%. Indeed, pores act as pins against domain formation and movement [140]. They tend to concentrate high mechanical stress and therefore reduce the materials' dielectric strength [51]. The porosity of PLZT ceramics can be reduced to less than around 1% by synthesizing samples using the isostatic hot-press method [140]. This method consists of simultaneously imposing a high temperature and external pressure during the sintering process. This procedure enhances particle packing and reduces the number and size of pores, thus increasing the samples' dielectric breakdown strength [140].

3. **Improve heat transfer**

The power output of devices using conduction [52], convection [5, 7, 19–22], or radi-

ation [31] could be advantageously enhanced by employing a multistaging technique envisioned by Olsen *et al.* [22]. This technique consists of placing pyroelectric materials in the order of increasing T_{Curie} between the cold and the hot sources. For example, the 9.5/65/35 PLZT material with Curie temperature around 65°C [141] at zero electric field can be included in the same multistage device as 8/65/35 PLZT and 6/65/35 PLZT with Curie temperatures of 113°C [70] and 240°C [68], respectively.

Novel pyroelectric converters which make use of different heat transfer mechanisms should be assembled and tested. For example, nanoscale radiation can be used to heat and cool a pyroelectric material rapidly, since radiation heat transfer occurs nearly instantaneously. In fact, Fang *et al.* [31] numerically showed that a pyroelectric material can reach its phase transition temperature rapidly during the Olsen cycle when heated by nanoscale radiation, and theoretically, large device efficiencies and power densities can be achieved using nanoscale radiation and the Olsen cycle. These numerical results should be validated against experimental data over a wide range of operating conditions in a pyroelectric converter.

References

[1] Lawrence Livermore National Laboratory, "U.S. Energy Flow Trends - 2009", https://publicaffairs.llnl.gov/news/energy/energy.html#2009, September 16, 2011.

[2] S.B. Lang and D.K. Das-Gupta, *Handbook of Advanced Electronic and Photonic Materials and Devices*, vol. 4, Academic Press, San Diego, CA, 2001.

[3] S.B. Lang, "Pyroelectricity: from ancient curiosity to modern imaging tool", *Physics Today*, vol. 58, pp. 31–36, 2005.

[4] M. Ikura, "Conversion of low-grade heat to electricity using pyroelectric copolymer", *Ferroelectrics*, vol. 267, pp. 403–408, 2002.

[5] R.B. Olsen and D.A. Bruno, "Pyroelectric conversion materials", in *Proceedings of the 21st Intersociety Energy Conversion Engineering Conference, American Chemical Society*, San Diego, CA, August 25-29 1986, pp. 89–93.

[6] A. Navid and L. Pilon, "Pyroelectric energy harvesting using Olsen cycles in purified and porous poly(vinylidene fluoride-trifuoroethylene) thin films", *Smart Materials and Structures*, vol. 20, no. 2, pp. 025012, 2011.

[7] H. Nguyen, A. Navid, and L. Pilon, "Pyroelectric energy converter using co-polymer P(VDF-TrFE) and the Olsen cycle for waste heat energy harvesting", *Applied Thermal Engineering*, vol. 30, no. 14-15, pp. 2127–2137, 2010.

[8] U.S. Census Bureau, "U.S. and world population clocks", http://www.census.gov/main/www/popclock.html, July 11, 2012.

[9] The United Nations Department of Economics and Social Affairs, "United nations press release", http://esa.un.org/unpd/wpp/other-information/Press_Release_WPP2010.pdf, May 3, 2011.

[10] The United Nations Department of Economics and Social Affairs, "World urbanization prospects, the 2009 revision, highlights", http://esa.un.org/unpd/wup/Documents/WUP2009_Highlights_Final.pdf, March 2010.

[11] C.F. Taylor, *The Internal Combustion Engine in Theory and Practice - Chapter 8: Heat Losses*, The MIT Press, Cambridge, MA, 1985.

[12] W.C. Turner and S. Doty, *Energy Management Handbook*, Fairmont Press, 6th edition, 2007.

[13] Wikipedia, "Cogeneration", http://en.wikipedia.org/wiki/Cogeneration, April 22, 2008.

[14] B.T. Liu, K.H. Chien, and C.C. Wang, "Effect of working fluids on organic Rankine cycle for waste heat recovery", *Energy*, vol. 29, no. 8, pp. 1207 – 1217, 2004.

[15] D.G. Thombare and S.K. Verma, "Technological development in the Stirling cycle engines", *Renewable and Sustainable Energy Reviews*, vol. 12, pp. 1–38, 2008.

[16] S.B. Riffat and X. Ma, "Thermoelectrics: a review of present and potential applications", *Applied Thermal Engineering*, vol. 23, no. 8, pp. 913–935, 2003.

[17] Renewable Energy Today, "World's largest solar power project unveiled", http://renewableenergytoday.net/rea/news/story?id=35263, May 7, 2008.

[18] Todd Woody, "Have you driven a Fjord lately?", http://money.cnn.com/magazines/business2/business2_archive/2007/08/01/100138830/index.htm?postversion=2007073110, April 20, 2008.

[19] R.B. Olsen, D.A. Bruno, J.M. Briscoe, and W.F. Butler, "A pyroelectric energy converter which employs regeneration", *Ferroelectrics*, vol. 38, no. 1-4, pp. 975–978, 1981.

[20] R.B. Olsen, "Ferroelectric conversion of heat to electrical energy - a demonstration", *Journal of Energy*, vol. 6, pp. 91–95, 1982.

[21] R.B. Olsen and D.D. Brown, "High-efficiency direct conversion of heat to electrical energy related pyroelectric measurements", *Ferroelectrics*, vol. 40, no. 1-2, pp. 17–27, 1982.

[22] R.B. Olsen, D.A. Bruno, and J.M. Briscoe, "Cascaded pyroelectric energy converter", *Ferroelectrics*, vol. 59, no. 3-4, pp. 205–219, 1984.

[23] R.B. Olsen, D.A. Bruno, and J.M. Briscoe, "Pyroelectric conversion cycles", *Journal of Applied Physics*, vol. 58, no. 12, pp. 4709–4716, 1985.

[24] L. Kouchachvili and M. Ikura, "High performance P(VDF-TrFE) copolymer for pyroelectric conversion", U.S. Patent #7,323,506 issued 1/29/2008, filed 2004.

[25] L. Kouchachvili and M. Ikura, "Improving the efficiency of pyroelectric conversion", *International Journal of Energy Research*, vol. 32, pp. 328–335, 2008.

[26] A. Navid, D. Vanderpool, A. Bah, and L. Pilon, "Towards optimization of a pyroelectric energy converter for harvesting waste heat", *International Journal of Heat and Mass Transfer*, vol. 53, no. 19-20, pp. 4060 – 4070, 2010.

[27] G. Sebald, L. Seveyrat, D. Guyomar, L. Lebrun, B. Guiffard, and S. Pruvost, "Electrocaloric and pyroelectric properties of $0.75Pb(Mg_{1/3}Nb_{2/3})O_3$-$0.25PbTiO_3$ single crystals", *Journal of Applied Physics*, vol. 100, pp. 124112 1–6, 2006.

[28] D. Guyomar, S. Pruvost, and G. Sebald, "Energy harvesting based on FE-FE transition in ferroelectric single crystals", *IEEE Transactions on Ultrasonics, Ferroelectrics, and Frequency Control*, vol. 55, pp. 279–285, 2008.

[29] A. Khodayari, S. Pruvost, G. Sebald, D. Guyomar, and S. Mohammadi, "Nonlinear pyroelectric energy harvesting from relaxor single crystals", *IEEE Transactions on Ultrasonics, Ferroelectrics, and Frequency Control*, vol. 56, pp. 693–699, 2009.

[30] H. Zhu, S. Pruvost, D. Guyomar, and A. Khodayari, "Thermal energy harvesting from $Pb(Zn_{1/3}Nb_{2/3})_{0.955}Ti_{0.045}O_3$ single crystals phase transitions", *Journal of Applied Physics*, vol. 106, no. 12, pp. 124102, 2009.

[31] J. Fang, H. Frederich, and L. Pilon, "Harvesting nanoscale thermal radiation using pyroelectric materials", *ASME Journal of Heat Transfer*, vol. 132, no. 9, pp. 092701, 2010.

[32] A. Cuadras, M. Gasulla, and V. Ferrari, "Thermal energy harvesting through pyro-electricity", *Sensors and Actuators A: Physical*, vol. 158, no. 1, pp. 132–139, 2010.

[33] P. Mane, J. Xie, K. Leang, and K. Mossi, "Cyclic energy harvesting from pyroelectric materials", *IEEE Transactions on Ultrasonics, Ferroelectrics, and Frequency Control*, vol. 58, no. 1, pp. 10–17, 2011.

[34] S. Hunter, N. Lavrik, T. Bannuru, S. Mostafa, S. Rajic, P. Datskos, edited by N. Dhar, P. Wijewarnasuriya, and A. Dutta, "Development of MEMS based pyroelectric thermal energy harvesters", in *Energy Harvesting and Storage: Materials, Devices, and Applications II*, Orlando, FL, April 25 2011, p. 80350V.

[35] S.K.T. Ravindran, T. Huesgen, M. Kroener, and P. Woias, "A self-sustaining micro thermomechanic pyroelectric generator", *Applied Physics Letters*, vol. 99, pp. 104102, 2011.

[36] R.B. Olsen, D.A. Bruno, and J.M. Briscoe, "Pyroelectric conversion cycle of vinylidene fluoride-trifluoroethylene copolymer", *Journal of Applied Physics*, vol. 57, no. 11, pp. 5036–5042, 1985.

[37] J.N. Zemel, "Future directions for thermal information sensors", *Sensors and Actuators A*, vol. 56, pp. 57–62, 1996.

[38] A. van der Ziel, "Solar power generation with the pyroelectric effect", *Journal of Applied Physics*, vol. 45, no. 9, pp. 4128, 1974.

[39] W.H. Clingman and R.G. Moore, "Application of ferroelectricity to energy conversion processes", *Journal of Applied Physics*, vol. 32, pp. 675–681, 1961.

[40] L. Kouchachvili and M. Ikura, "Pyroelectric conversion - effects of P(VDF-TrFE) preconditioning on power conversion", *Journal of Electrostatics*, vol. 65, no. 1, pp. 182–188, 2006.

[41] M.A. Itskovsky, "Pyroelectric hysteresis loop at ferroelectric phase transition", *Journal of Applied Physics*, vol. 85, pp. 4256–4258, 1999.

[42] B. Rozic, B. Malic, H. Ursic, J. Holc, M. Kosec, B. Neese, Q.M. Zhang, and Z. Kutnjak, "Direct measurements of the giant electrocaloric effect in soft and solid ferroelectric materials", *Ferroelectrics*, vol. 405, pp. 26–31, 2010.

[43] S.G. Lu, B. Rozie, Q.M. Zhang, Z. Kutnjak, B. Li, E. Furman, L.J. Gorny, M. Lin, B. Malie, M. Kosec, R. Blinc, and R. Pirc, "Organic and inorganic relaxor ferroelectrics with giant electrocaloric effect", *Applied Physics Letter*, vol. 97, pp. 162904, 2010.

[44] G. Sebald, S. Pruvost, and D. Guyomar, "Energy harvesting based on Ericsson pyroelectric cycles in a relaxor ferroelectric ceramic", *Smart Materials and Structures*, vol. 17, pp. 1–6, 2008.

[45] A.S. Mischenko, Q. Zhang, J.F. Scott, R.W. Whatmore, and N.D. Mathur, "Giant electrocaloric effect in thin-film $PbZr_{0.95}Ti_{0.05}O_3$", *Science*, vol. 311, no. 5765, pp. 1270–1271, 2006.

[46] A.S. Mischenko, Q.Zhang, R.W. Whatmore, J.F. Scott, and N.D. Mathur, "Giant electrocaloric effect in the thin film relaxor ferroelectric 0.9 $PbMg_{1/3}Nb_{2/3}O_3$–0.1 $PbTiO_3$ near room temperature", *Applied Physics Letters*, vol. 89, pp. 242912, 2006.

[47] T.M. Correia, J.S. Young, R.W. Whatmore, J.F. Scott, N.D. Mathur, and Q. Zhang, "Investigation of the electrocaloric effect in a $PbMg_{2/3}Nb_{1/3}O_3$–$PbTiO_3$ relaxor thin film", *Applied Physics Letters*, vol. 95, pp. 182904, 2009.

[48] B. Neese, S.G. Lu, B. Chu, and Q.M. Zhang, "Electrocaloric effect of the relaxor ferroelectric poly(vinylidene fluoride-trifluoroethylene-chlorofluoroethylene) terpolymer", *Applied Physics Letters*, vol. 94, pp. 042910, 2009.

[49] S.B. Lang, *Sourcebook of Pyroelectricity*, Gordon and Breach, Science Publishers, Inc., New York, NY, 1974.

[50] R.C. Moreno, B.A. James, A. Navid, and L. Pilon, "Pyroelectric energy converter for harvesting waste heat: Simulations versus experiments", *International Journal of Heat and Mass Transfer*, vol. 55, pp. 4301–4311, 2012.

[51] A. Navid, C.S. Lynch, and L. Pilon, "Purified and porous poly(vinylidene fluoride-trifluoroethylene) [P(VDF-TrFE)] thin films for pyroelectric infrared sensing and energy harvesting", *Smart Materials and Structures*, vol. 19, pp. 055006, 2010.

[52] F.Y. Lee, A. Navid, and L. Pilon, "Pyroelectric waste heat energy harvesting using heat conduction", *Applied Thermal Engineering*, vol. 37, no. 1, pp. 30–37, 2012.

[53] R. Kandilian, A. Navid, and L. Pilon, "The pyroelectric energy harvesting capabilities of PMN-PT near the morphotropic phase boundary", *Smart Materials and Structures*, vol. 20, no. 1, pp. 055020, 2011.

[54] M.E. Lines and A.M. Glass, *Principles and Applications of Ferroelectrics and Related Materials*, Clarendon Press, Oxford, UK, 1977.

[55] L. Kouchachvili and M. Ikura, "Pyroelectric conversion-effects of P(VDF-TrFE) pre-conditioning on power conversion", *Journal of Electrostatics*, vol. 65, pp. 182–188, 2006.

[56] V. Sencadas, S. Lanceros-Mendez, and J.F. Mano, "Characterization of poled and non-poled β-PVDF films using thermal analysis techniques", *Thermochimica Acta*, vol. 424, pp. 201–207, 2004.

[57] B. Chu, X. Zhou, K. Ren, B. Neese, M. Lin, Q. Wang, F. Bauer, and Q.M. Zhang, "A dielectric polymer with high electric energy density and fast discharge speed", *Science*, vol. 313, no. 5785, pp. 334–336, 2006.

[58] I. McKinley, R. Kandilian, and L. Pilon, "Waste heat energy harvesting using Olsen cycle on $0.945Pb(Zn_{1/3}Nb_{2/3})O_3$-$0.055PbTiO_3$ single crystals", *Smart Materials and Structures*, vol. 11, no. 3, pp. 035015, 2012.

[59] Z. Li, Z. Xi, Z. Xu, and X. Yao, "Dielectric/ferroelectric response and phase transition of PMN-0.32PT single crystal", *Journal of Materials Science Letters*, vol. 21, pp. 1325–1327, 2002.

[60] F.J. Balta Calleja, A. Gonzalez Arche, T.A. Ezquerra, C. Santa Cruz, F. Batallan, B. Frick, and E. Lopez Cabarcos, "Structure and properties of ferroelectric copolymers of poly(vinylidene fluoride)", *Advances in Polymer Science*, vol. 108, pp. 1–48, 1993.

[61] T. Yamada, T. Ueda, and T. Kitayama, "Ferroelectric-to-paraelectric phase transition of vinylidene fluoride-trifluoroethylene copolymer", *Journal of Applied Physics*, vol. 52, no. 2, pp. 948–952, 1981.

[62] R. Zhang, B. Jiang, and W. Cao, "Orientation dependence of piezoelectric properties of single domain $0.67PbMg_{1/3}Nb_{2/3}O_3$–$0.33$ $PbTiO_3$ single crystals", *Applied Physics Letters*, vol. 82, no. 21, pp. 3737–3739, 2003.

[63] Z. Li, Z. Xu, Z. Xi, F. Xiang, and X. Yao, "Thermal expansion characteristics in [001]-oriented PMN-0.32PT single crystals", *Ferroelectrics*, vol. 355, no. 1, pp. 245–251, 2007.

[64] P. Kumar, S. Sharma, O.P. Thakur, C. Prakash, and T.C. Goel, "Dielectric, piezoelectric and pyroelectric properties of PMN-PT (68:32) system", *Ceramics International*, vol. 30, no. 4, pp. 585 – 589, 2004.

[65] N. Yasuda, T. Banno, K. Fujita, H. Ohwa, M. Matushita, Y. Yamashita, M. Iwata, and Y. Ishibashi, "Piezoelectric properties of relaxor ferroelectric solid solution single crystals PMN-PT and PZN-PT near MPB under pressures", *Ferroelectrics*, vol. 347, no. 1, pp. 44–49, 2007.

[66] K.B.R. Varma, "Morphology and dielectric properties of fish scales", *Current science*, vol. 59, no. 8, pp. 420–423, 1990.

[67] S. Bauer and S.B. Lang, "Pyroelectric polymer electrets", *IEEE Transaction of Dielectrics and Electrical Insulation*, vol. 56, pp. 57–62, 1996.

[68] G.H. Haertling and R.C. Buchanan (ed.), *Ceramic Materials for Electronics: Processing, Properties, and Applications*, Marcel Dekker, New York, NY, 1991.

[69] G.A. Samara, "Ferroelectricity revisited–advances in materials and physics", vol. 56 of *Solid State Physics*, pp. 239 – 458. Academic Press, San Diego, CA, 2001.

[70] M. Akbas, I. Reaney, and W. Lee, "Domain structure-property relations in lead lanthanum zirconate titanate ceramics", *Journal of Materials Research*, vol. 11, no. 9, pp. 2293–2301, 1996.

[71] C.S. Lynch, "The effect of uniaxial stress on the electro-mechanical response of 8/65/35 PLZT", *Acta Materialia*, vol. 44, pp. 4137–4139, 1996.

[72] T. Liu and C.S. Lynch, "Domain engineered relaxor ferroelectric single crystals", *Continuum Mechanics and Thermodynamics*, vol. 18, pp. 119–135, 2006.

[73] C.S. Lynch, "Large field electromechanical measurement techniques for ferroelectric materials", *Integrated Ferroelectrics*, vol. 111, pp. 59–67, 2011.

[74] G.H. Haertling, "Ferroelectric ceramics: History and technology", *Journal of American Ceramic Society*, vol. 82, no. 4, pp. 797–818, 1999.

[75] D.E. Dausch and G.H. Haertling, "The domain switching and structural characteristics of PLZT bulk ceramics and thin films chemically prepared from the same acetate precursor solutions", *Journal of Materials Science*, vol. 31, pp. 3409–3417, 1996.

[76] G.H. Haertling and C.E. Land, "Hot-pressed (Pb,La)(Zr,Ti)O$_3$ ferroelectric ceramics for electro-optic applications", *Journal of American Ceramic Society*, vol. 54, no. 1, pp. 1–11, 1971.

[77] M.W. Hooker, "Properties of PZT-based piezoelectric ceramics between -150 and 250°C", *NASA/CR-1998-208708*, 1998.

[78] V. Bobnar, Z. Kutnjak, R. Pirc, and A. Levstik, "Electric-field-temperature phase diagram of the relaxor ferroelectric lanthanum-modified lead zirconate titanate", *Physical Review B*, vol. 60, pp. 6420–6427, 1999.

[79] B. Vodopivec, C. Filipic, A. Levstik, J. Holc, and Z. Kutnjak, "E-T phase diagram of the 6.5/65/35 PLZT incipient ferroelectric", *Journal of the European Ceramic Society*, vol. 24, pp. 15611564, 2004.

[80] D. Viehland, X.H. Dai, J.F. Li, , and Z. Xu, "Effects of quenched disorder on la-modified lead zirconate titanate: Long and short-range ordered structurally incommensurate phases, and glassy polar clusters", *Journal of Applied Physics*, vol. 84, no. 1, pp. 458–471, 1998.

[81] S. Kamba, V. Bovton, J. Petzelt, I. Rychetsky, R. Mizaras, A. Brilingas, J. Banys, J. Gringas, and M. Kosec, "Dielectric dispersion of the relaxor PLZT ceramics in the frequency range 20 Hz-100 THz", *Journal of Physics: Condensed Matter*, vol. 12, pp. 497519, 2000.

[82] J.L. Dellis, M. El Marssi, P. Tilloloy, R. Farhi, and D. Viehland, "A dielectric study of the x/65/35 lanthanum-modified lead zirconate titanate series", *Ferroelectrics*, vol. 201, pp. 167–174, 1997.

[83] Y. Xi, C. Zhili, and L.E. Cross, "Polarization and depolarization behavior of hot pressed lead lanthanum zirconate titanate ceramics", *Journal of Applied Physics*, vol. 54, no. 6, pp. 3399–3403, 1983.

[84] A.S. Divya nad V. Kumar, "A novel mechanism for relaxor-ferroelectric transition in PLZT (8/65/35)", *Journal of American Ceramic Society*, vol. 92, no. 9, pp. 2029–2032, 2009.

[85] Z. Kutnjak, C. Filipic, R. Pirc, and A. Levstik, "Slow dynamics and ergodicity breaking in a lanthanum-modified lead zirconate titanate relaxor system", *Physical Review B*, vol. 59, no. 1, pp. 294–301, 1999.

[86] F.Y. Lee, S. Goljahi, I. McKinley, C.S. Lynch, and L. Pilon, "Pyroelectric waste heat energy harvesting using relaxor ferroelectric 8/65/35/ PLZT and the Olsen cycle", *Smart Materials and Structures*, vol. 21, no. 2, pp. 025021, 2012.

[87] T. Chin, F.Y. Lee, I.M. McKinley, S. Goljani, C.S. Lynch, and L. Pilon, "Pyroelectric waste heat energy harvesting using 9.5/65/35 PLZT ceramics", *IEEE Transactions on Ultrasonics, Ferroelectrics, and Frequency Control*, vol. 59, no. 11, pp. 2373–2385, 2012.

[88] S.K.T. Ravindran, T. Huesgen, M. Kroener, and P. Woias, "A self-sustaining pyroelectric energy harvester utilizing spatial thermal gradients", in *Solid-State Sensors, Actuators and Microsystems Conference (TRANSDUCERS), 2011 16th International*, Beijing, China, June 5-9 2011, pp. 657–660.

[89] G. Cha and S.Y. Ju, "Electric field dependence of the curie temperature of ferroelectric poly(vinylidenefluoride-trifluoroethylene) co-polymers for pyroelectric energy harvesting", *Smart Materials and Structures*, vol. 21, no. 2, pp. 022001, 2012.

[90] H. Zhu, S. Pruvost, P.J. Cottinet, D. Guyomar, and Mickael Lallart (ed.), *Thermal Energy Harvesting Using Fluorinated Terpolymers, Small-Scale Energy Harvesting*, In-Tech, 2012.

[91] A. Narayanaswamy, S.Shen, and G. Chen, "Near-field radiative heat transfer between a sphere and a substrate", *Applied Physics B*, vol. 78, pp. 115303, 2000.

[92] S. Shen, A. Narayanaswamy, and G. Chen, "Surface phonon polaritons mediated energy transfer between nanoscale gaps", *Nano Letters*, vol. 9, no. 8, pp. 2909–2913, 2009.

[93] A. Narayanaswamy, S. Shen, L. Hu, X. Chen, and G. Chen, "Breakdown of the planck blackbody radiation law at nanoscale gaps", *Applied Physics A*, vol. 96, no. 2, pp. 357–362, 2009.

[94] L. Hu, A. Narayanaswamy, X. Chen, and G. Chen, "Near-field thermal radiation between two closely spaced glass plates exceeding planck's blackbody radiation law", *Applied Physics Letters*, vol. 92, no. 13, pp. 133106, 2009.

[95] Omega Engineering, "Thermally conductive epoxies and thermally conductive grease", http://www.omega.com/pptst/OB100_OB200_OT200.html, June 14, 2011.

[96] K.J. Kim and S.L. Hsu, "An infra-red spectroscopic study of structural reorganization of a uniaxially draw VDF/TrFE copolymer in an electric field", *Journal of Polymer Science*, vol. 35, pp. 3612–3618, 1993.

[97] K.J. Kim and G.B. Kim, "Curie transition, ferroelectric crystal structure and ferroelectricity of VDF/TrFE (75/25) copolymer: 2. The effect of poling on Curie transition and ferroelectric crystal structure", *Journal of Polymer Science*, vol. 38, pp. 4881–4889, 1997.

[98] H. Yamazaki, J. Ohwaki, T. Yamada, and T. Kitayama, "Temperature dependence of the pyroelectric response of vinylidene fluoride trifluoroethylene copolymer and the effect of its poling conditions", *Applied Physics Letters*, vol. 39, pp. 772–773, 1981.

[99] J. Yu and M. Ikura, "Direct conversion of low-grade heat to electricity using pyroelectric conversion", in *Proceedings of the Fourth IASTED International Conference European Power and Energy Systems*, Rhodes, Greece, 2004, pp. 442–446.

[100] E.O. Forster, H. Yamashita, C. Mazzetti, C. Pompili, L. Caroli, and S. Patrissi, "The effect of electrode gap on breakdown in liquid dielectrics", *IEEE Transactions on Dielectrics and electical insulation*, vol. 1, no. 3, pp. 440–446, 1994.

[101] F.P. Incropera, D.P. DeWitt, T. Bergman, and A. Lavine, *Fundamentals of Heat and Mass Transfer (6th ed.)*, John Wiley and Sons, Ltd., New York, NY, 2006.

[102] F.Y. Chen, Y.K. Fang, C.Y. Hsu, and J.R. Chen, "Time response analysis of a pyroelectric detector", *Ferroelectrics*, vol. 200, no. 1, pp. 257–268, 1997.

[103] M.C. Kao, C.M. Wang, H.Z. Chen, M.S. Lee, , and Y.C. Chen, "Thickness-dependent leakage current of (polyvinylidene fluoride/lead titanate) pyroelectric detectors", *IEEE Transactions on Ultrasonics, Ferroelectrics, and Frequency Control*, vol. 50, no. 8, pp. 958–964, 2003.

[104] R. Buchanan and J. Huang, "Pyroelectric and sensor properties of ferroelectric thin films for energy conversion", *Journal of the European Ceramic Society*, vol. 98, pp. 1467–1471, 1999.

[105] H.H.S. Chang and Z. Huang, "Laminate composites with enhanced pyroelectric effects for energy harvesting", *Smart Materials and Structures*, vol. 19, no. 1, pp. 065018, 2010.

[106] G. Sebald, E. Lefeuvre, and D. Guyomar, "Pyroelectric energy conversion: optimization principles", *IEEE Transactions on Ultrasonics, Ferroelectrics, and Frequency Control*, vol. 55, pp. 538–551, 2008.

[107] I.A. Santos, C. Endo, A.L. Zanin, M.H. Lente, J.A. Eiras, and D. Garcia, "Hot-pressed transparent PLZT ceramics from low cost chemical processing", *Materials Research*, vol. 4, no. 4, pp. 291–295, 2001.

[108] M. Simhony, M. Bass, E. Van Stryland, E. Tenescu, and B. Levy, "Fast response of PLZT pyroelectric detectors to megawatt CO_2 laser pulses", *IEEE Journal of Quantum Electronics*, vol. 15, no. 4, pp. 206–208, 1979.

[109] B. Liščić, "Heat transfer control during quenching", *Materials and Manufacturing Processes*, vol. 24, pp. 879–886, 2009.

[110] M. Rauls, W. Dong, J. Huber, and C.S. Lynch, "The effect of temperature on the large field electromechanical response of relaxor ferroelectric 8/65/35 PLZT", *Acta Materialia*, vol. 59, no. 7, pp. 2713–2722, 2011.

[111] L.X. Zhang, X. Ren, Y. Wang, X.Q. Ke, X.D. Ding, and J. Sun, "Novel electro-strain-effect in La-doped Pb(Zr,Ti)O$_3$ relaxor ferroelectrics", in *International Conference on Martensitic Transformations*, Santa Fe, NM, June 29-July 5, 2008.

[112] A.I. Burkhanov and A.V. Shil'Nikov, "Super slow polarization relaxation in PLZT relaxor ceramics", *Ferroelectrics*, vol. 299, no. 1, pp. 153–156, 2010.

[113] Z.G. Ye, "Relaxor ferroelectric Pb($Mg_{1/3}Nb_{2/3}$)O$_3$: Properties and present understanding", *Ferroelectrics*, vol. 184, no. 1, pp. 193–208, 1996.

[114] E. Furman and L.E. Cross, "Dielectric breakdown in PLZT 9.5/65/35 ceramics", in *Proceedings of the Ninth IEEE International Symposium on Ferroelectrics*, College Park, PA, August 7-10, 1994, pp. 577–580.

[115] C.S. Lynch, "Fracture of ferroelectric and relaxor electro-ceramics: influence of electric field", *Acta Materialia*, vol. 46, no. 2, pp. 599–608, 1998.

[116] H. Cao and A.G. Evans, "Electric-field-induced fatigue crack growth in piezoelectrics", *Journal of American Ceramic Society*, vol. 77, no. 7, pp. 1783–1786, 1994.

[117] H. Zhu, S. Pruvost, P.J. Cottinet, and D. Guyomar, "Energy harvesting by nonlinear capacitance variation for a relaxor ferroelectric poly(vinylidene fluoride-trifluoroethylene-chlorofluoroethylene) terpolymer", *Applied Physics Letters*, vol. 98, no. 22, pp. 222901–222901–3, 2011.

[118] A. Safari, R.K. Panda, and V.F. Janas, "Ferroelectric ceramics: Processing, properties and applications", http://www.rci.rutgers.edu/ ecerg/projects/ferroelectric.html, December 8, 2011.

[119] R. Selvamani, G. Singh, and V.S. Tiwari, "Electro-caloric effect in PLZT (8/65/35) ceramic", in *Proceedings of the 56th DAE Solid State Physics Synopsium 2011*, SRM University, Kattankulathur, Tamilnadu, India, 2012, pp. 1281–1282.

[120] MG Chemicals, "Technical specifications silicon conformal coating (liquid) 422-1L/4L/20L liquid", http://www.mgchemicals.com/downloads/pdf/specsheets/422l.pdf, January 3, 2012.

[121] G.H. Haertling, E. Furman, C.S. Hsi, and G. Li, "Superconductivity devices: Commercial use of space", Tech. Rep., September 1993.

[122] C. Filipic, B. Vodopivec, J. Holc, A. Levstik, Z. Kutnjak, and H. Beige, "Relaxor and incipient ferroelectric phases in 6.5/65/35 PLZT ceramics", *Journal of the European Ceramic Society*, vol. 24, pp. 15651568, 2004.

[123] D. Wang, Y. Fotinich, and G.P. Carman, "Influence of temperature on the electromechanical and fatigue behavior of piezoelectric ceramics", *Journal of Applied Physics*, vol. 83, no. 10, pp. 5342–5350, 1998.

[124] Y.S. Touloukian, *Thermophysical Properties of Matter*, IFI/Plenum, New York, NY, 1975.

[125] C.S. Lynch, W. Yang, L. Collier, Z. Suo, and R.M. McMeeking, "Electric field induced cracking in ferroelectric ceramics", *Ferroelectrics*, vol. 166, pp. 11–30, 1995.

[126] J. Nuffer, D.C. Lupascu, and J. Rodel, "Microcrack clouds in fatigued electrostrictive 9.5/65/35 PLZT", *Journal of the European Ceramic Society*, vol. 21, no. 1, pp. 1421–1423, 2001.

[127] B. Fang, Q. Du, L. Zhou, X. Zhao, H. Xu, and H. Luo, "Structural phase transition and physical properties of tetragonal $0.85Pb(Zn_{1/3}Nb_{2/3})O_3$-$0.15PbTiO_3$ single crystals", *Journal of Applied Physics*, vol. 106, no. 7, pp. 074110–1, 2009.

[128] K. wa Gachigi, "Electrical energy storage in antiferroelectric-ferroelectric switching, chemically modified lead zirconate ceramics", Tech. Rep., Pennsylvania State University, May 1997.

[129] S. Shah and M.S. Rao, "Preparation and dielectric study of high-quality PLZT x/65/35 (x=6,7,8) ferroelectric ceramics", *Applied Physics A*, vol. 71, pp. 65–69, 2000.

[130] Clearco Products, "Silicone transformer oil", www.clearcoproducts.com/siliconetransformeroil.ht: May 14, 2012.

[131] A. Kholkin, "Piezoresponse force microscopy of polarization dynamics in ferroelectrics", in *8th International Tutorial Workshop on Piezoresponse Force Microscopy and Nanoscale Electromechanics of Polar Materials*, Beijing, China, August 25-27, 2010.

[132] D.S. Tinburg, *Pulsed Laser Deposition of xBiScO₃-(1-x)BaTiO₃ Thin Films for Lead Free Dielectric Applications*, PhD thesis, The Pennsylvania State University, 2006.

[133] B. Vodopivec, C. Filipic, A. Levstik, J. Holc, and Z. Kutnjak, "Dielectric properties of partially disordered lanthanum-modified lead zirconate titanate relaxor ferroelectrics", *Physical Review B*, vol. 69, pp. 224208, 2004.

[134] M. Pavel, I. Rychetsky, and J. Petzelt, "Polar clusters in relaxor (Pb,La)(Zr,Ti)O₃ revealed by second harmonic generation", *Journal of Applied Physics*, vol. 89, no. 9, pp. 5036–5039, 2001.

[135] Intel Corporation, "Intel Atom Processor N450, D410 and D510 for Embedded Applications", http://download.intel.com/embedded/processors/thermalguide/323439.pdf, June 2, 2012.

[136] Z. Feng, D. Lin, and H. Luo, "Effect of uniaxial stress on the electromechanical response of ¡001¿-oriented pb(mg$_{1/3}$nb$_{2/3}$o₃pbtio₃ crystals", *Journal of Applied Physics*, vol. 97, pp. 024103, 2005.

[137] Q. Wan, C. Chen, and Y.P. Shen, "Effects of stress and electric field on the electromechanical properties of pb(mg$_{1/3}$nb$_{2/3}$o₃0.32pbtio₃ single crystals", *Journal of Applied Physics*, vol. 98, pp. 024103, 2005.

[138] M.D. Biegalski, Y. Jia, D.G. Schlom, S. Trolier-McKinstry, S.K. Streiffer, V. Sherman, R. Uecker, and P. Reiche, "Relaxor ferroelectricity in strained epitaxial srtio₃ thin films on dysco₃ substrates", *Applied Physics Letter*, vol. 88, no. 19, pp. 192907, 2006.

[139] K.J. Choi, M. Biegalski, Y.L. Li, A. Sharan, J. Schubert, R. Uecker, P. Reiche, Y.B. Chen, X.Q. Pan, V. Gopalan, L.Q. Chen, D.G. Schlom, and C.B. Eom, "Enhancement of ferroelectricity in strained batio₃ thin films", *Science*, vol. 306, no. 5698, pp. 1005–1009, 2004.

[140] Q. Yin, B. Zhu, and H. Zeng, *Microstructure, Property and Processing of Functional Ceramics*, Springer, New York, NY, 2009.

[141] D.E. Dausch and G.H. Haertling, "Bulk vs. thin film PLZT ferroelectrics", in *Proceedings of the 8th IEEE International Symposium on Applications of Ferroelectrics (ISAF'92)*, Greenville, SC, 1992, pp. 297–300.